Master of Science Thesis

Design of a combined optical and structural bone phantom

Concept validation and design tool

Tess Madelief van Pelt

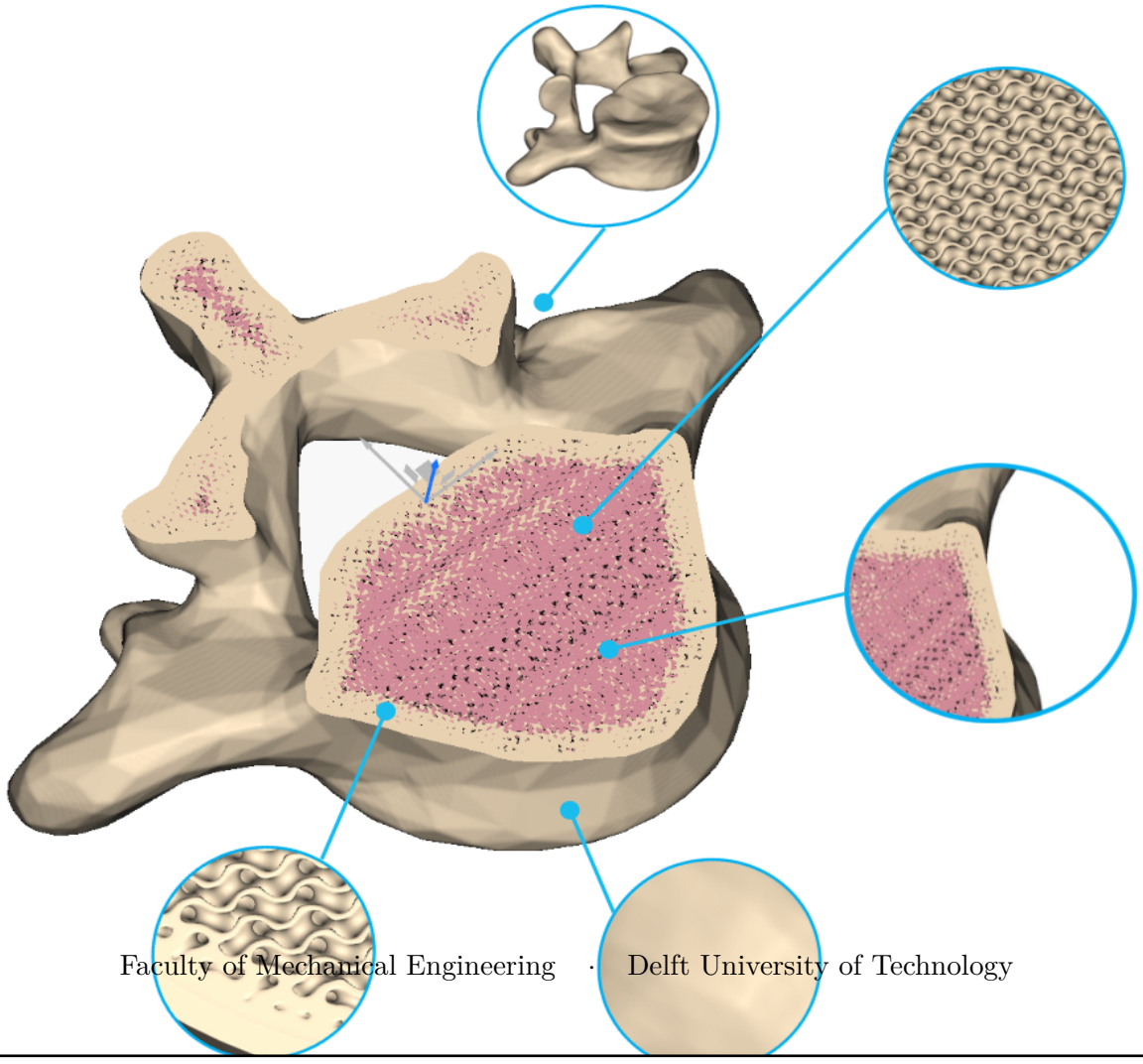

Faculty of Mechanical Engineering · Delft University of Technology

TU Delft Delft University of Technology

Design of a combined optical and structural bone phantom

Concept validation and design tool

Master of Science Thesis

For obtaining the degree of Master of Science in Mechanical Engineering at Delft University of Technology

Tess Madelief van Pelt

25-01-22

Faculty of Mechanical Engineering · Delft University of Technology

Delft University of Technology
Faculty of Mechanical Engineering
Department of Biomechanical Engineering

GRADUATION COMMITTEE

Dated: 25-01-22

Chair holder:

Prof.dr. J. Dankelman

Committee members:

Prof.dr. B.H.W. Hendriks

Dr.ir. A.J. Loeve

PhD candidate Msc. M. Losch

Abstract

Introduction: Although being the most advanced spinal stabilization method, pedicle screw fixation has an increased number of complications compared to other surgical procedures, due to the complex spinal anatomy, large inter-patient anatomical variability, and the highly vulnerable surrounding tissue of the spine. Screw fixation strength can be increased by anchoring a flexible screw in a hole following the curved trajectory of the more dense cortical shell of the vertebral body, instead of the porous core. The curved trajectory can be determined by local diffuse reflectance spectroscopy (DRS) guiding. Currently, there is no commercial phantom or phantom recipe known that provides the correct optical and structural material characteristics for testing DRS guiding and curved trajectory drilling on, comparing it to similar devices, and perform surgical training sessions on. The research goal is to design and validate an integrated phantom that closes this gap. **Preliminary test results:** Preliminary optical and structural tests were performed separately on hybrid optical filler samples and structural matrix samples, respectively. The hybrid optical filler samples made out of water, fat (30%, 40% and 50% fat fraction) and silicone (95%, 80%, and 50%) were inspected visually, and spectra were obtained by means of a DRS device in week 0 as well as in week 10. The most promising optical filler sample consisted of 50% of silicone and 50% of water+fat, with a fat fraction of 40%. The measured DRS signals showed a clear correlation between the fitted and actual water+fat content, which, can thus be used as a tissue differentiation parameter. The stability and preservability of phantoms that were enhanced with silicone and resulted in homogeneous mixtures, was increased compared to samples without any silicone. For the structural matrix, different 3D printers, materials, and infill densities were evaluated on drill characteristics and compression characteristics. The best bone mimicking structural phantom consisted of an FDM printed part made out of ABS with a gyroid infill structure with an infill density of 50%. **Integrated phantom validation:** The combination of the optical filler and the structural matrix was validated by infusing the optical filler in the structural matrix with a vacuum chamber and measuring the drill characteristics and DRS spectra at various depths inside the phantom. A gradual increase in axial drilling force and a gradual change in spectral shape was noticed as a function of depth from the cancellous zone, to the pre-cortical zone and cortical zone. **Discussion:** The ABS material and the actual optical filler constituents (such as peanut oil and specific silicone types) should be implemented in

the fitting algorithm. Nevertheless, the results of this research show not only great potential phantom design for a wide variety of bone types because of the structure and shape design flexibility of 3D printing, but also for soft tissues by using only the optical filler with a much better stability and preservability than traditional soft tissue phantoms.

Preface

On April 19th 2021 I started this project in good spirits, thinking that the horror stories I had heard about graduation projects would not apply to those who are truly interested in the subject and see the potential impact of a fundamentally well structured research. Gladly, it turned out that this research was a perfect match with my personal interests and ideas about technological creation. I obtained my bachelor degree in Aerospace Engineering, and the redirection of field of study to Biomechanical Engineering enabled much more opportunity for fast progression and tangible results, which suits me better and would not have been as easy to accomplish in Aerospace Engineering. This project in particular connects well with my previous experience in material science and product design as a structural engineer working full time for a year in the Delft Hyperloop Dreamteam of the TU Delft in 2018/2019.

There was never a dull moment during my MSc Thesis project because I was fascinated by the subject and the belief that I could make a contribution to this topic of phantom design. The project contained the full spectrum of research aspects, from conducting a literature study, to developing a preliminary prototype. Because of the fast pace in which the phases followed up on each other, I was constantly challenged to tackle new types of problems. After having analyzed the final results, I still believe that there is a need for a reliable integrated optical and structural phantom and I think that the design investigated in this research has endless possibilities. I sincerely hope that the research I conducted attributed to the development of such a novel phantom.

During my thesis, I could always rely on the help, support and insightful feedback of my daily supervisor and PhD candidate Merle Losch. I would like to thank you for giving me a great deal of freedom such that I was able to steer my research into the desired direction, but still providing me with enough feedback to not get entangled in a web of design options. At the moments when I was near despair, you were able to clarify facts such that the focus was on the main goal again. I would also like to thank my first supervisor Prof.dr. J. Dankelman and my second supervisor Prof.dr. B.H.W. Hndriks for the feedback I received on my methodology as well as my report content and structure.

Table of Contents

List of Figures

List of Tables

Acronyms

AP	Anterior-Posterior
ABS	Acrylonitrile Butadiene Styrene
BMD	Bone Mineral Density
BVF	Bone Volume Fraction
DRFF	Diffuse Reflectance Fat Fraction
DRS	Diffuse Reflectance Spectroscopy
FF	Fat Fraction
FDM	Fused Deposition Modeling
ML	Medial-Lateral
NIR	Near Infra-Red
PDFF	Proton Density Fat Fraction
PMMA	Polymethylmethacrylate
PSF	Pedicle Screw Fixation
PU	Polyurethane
PVC	Polyvinyl Chloride
SI	Superior-Inferior
SLA	Stereolithography
VIS	Visible

Part I

First part

Chapter 1

Introduction

The number of complications during spinal surgeries is relatively high compared to other surgeries and the number of spinal surgeries is increasing in a fast rate as well. Because of this, there is need for a novel enhanced pedicle screw fixation method. One concept is pedicle screw fixation following a curved pathway along the cortical shell of the vertebral body by guiding based on Diffuse Reflectance Spectroscopy (DRS). Currently, no phantom exists that is easy to use and produce, reliable, cost-efficient and stable over time, to test this novel surgical device on. This chapter will guide you through the prerequisite anatomical knowledge, pedicle screw fixation procedure and enhanced pedicle screw fixation concept to come to the design objective of designing and validating a phantom that facilitates testing of the DRS system and the curved drill and flexible screw anchor systems simultaneously.

1.1 Prerequisite anatomical knowledge

First, the anatomy of the spine as well as bone characteristics will be discussed. The anatomical information mentioned in this section originates from Klenerman [3]. The anatomical reference system that is used throughout this report is shown in Figure 1.1.

1.1.1 Spinal anatomy

The spine or spinal column is a structure consisting of multiple vertebral bones vertically stacked and separated by intervertebral discs. The main functions of the spine are providing support to the head and trunk, protecting the spinal cord, and providing attachment points for the ribs, back muscles, and neck muscles. The spine is subdivided into three regions, from the head towards the pelvis: the cervical spine, the thoracic spine, and the lumbar spine. The vertebrae become progressively larger towards the pelvis because the weight on the lower parts of the spine increases as well. A healthy spine viewed from the sagittal plane is naturally positioned in an S-shape. A representation of a healthy spine is shown in Figure 1.2a.

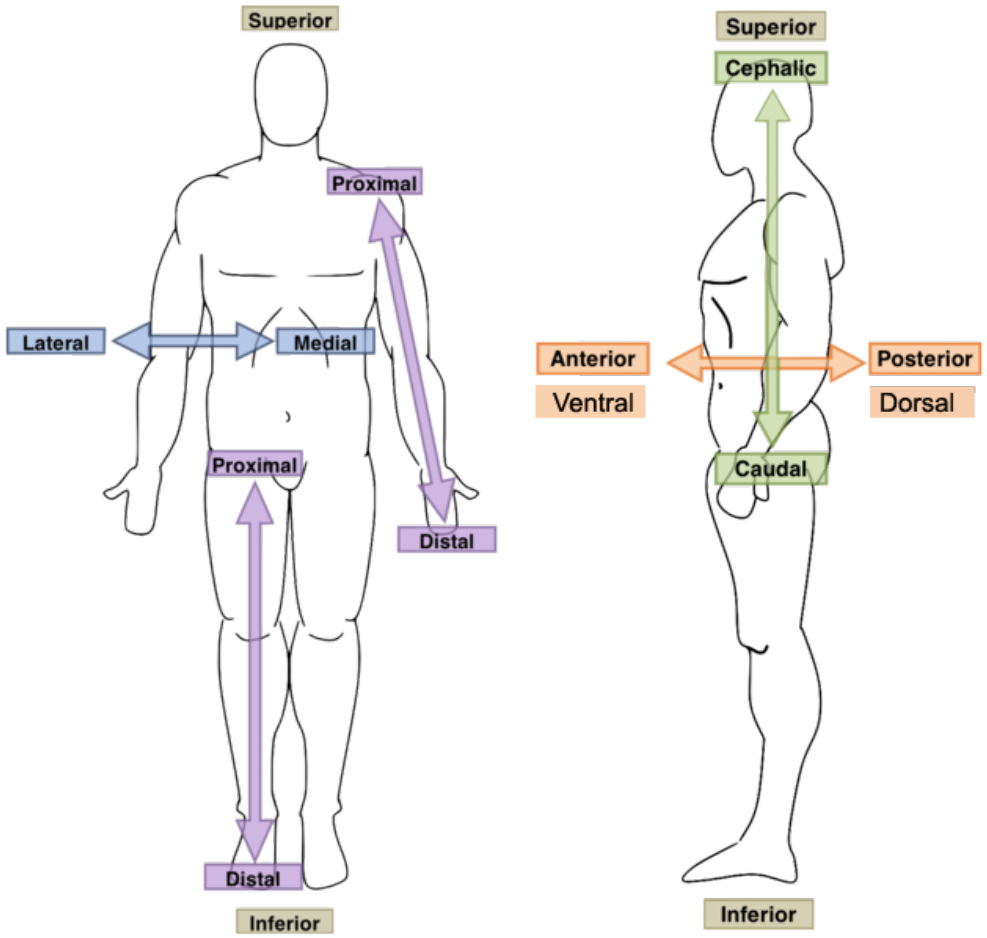

Figure 1.1: The anatomical reference system [1]

For some patients, the spine has an abnormal curvature. One frequent example is *scoliosis*, which is an abnormal lateral curvature of the spine, as shown in Figure 1.2b. Another example is *kyphosis*, which is a dorsally abnormal curvature of the upper part of the spine shown in Figure 1.2c. Kyphosis is a common disease for elderly people because it can result from osteoporosis (which will be discussed in the next section). An abnormal ventral lumbar curvature is called *lordosis*, and is shown in Figure 1.2d, which can result from pregnancy, a potbelly, spinal tuberculosis, or osteomalacia.

In Figure 1.3, various parts of a vertebra are labeled. A vertebra is subdivided into two sections: the vertebral body and the vertebral arch (indicated in Figure 1.3a). The vertebral body is the largest bony part of each vertebra. Due to its flat shape with a large horizontal surface, the vertebral body is optimized for resisting vertical loads. Approximately 80% of the weight of the body is supported by the vertebral body [16]. On top of that, it protects the vulnerable spinal cord, indicated in Figure 1.3b. Vertebral dimensions vary per person, depending on sex, age, and body length. A study by Maclaughlin and Oldal [17] showed that the average diameter of the lower thoracic and first lumbar vertebral bodies in the medial-lateral direction for grown males is 30.8 mm and for females 26.3 mm, and in the anterior-

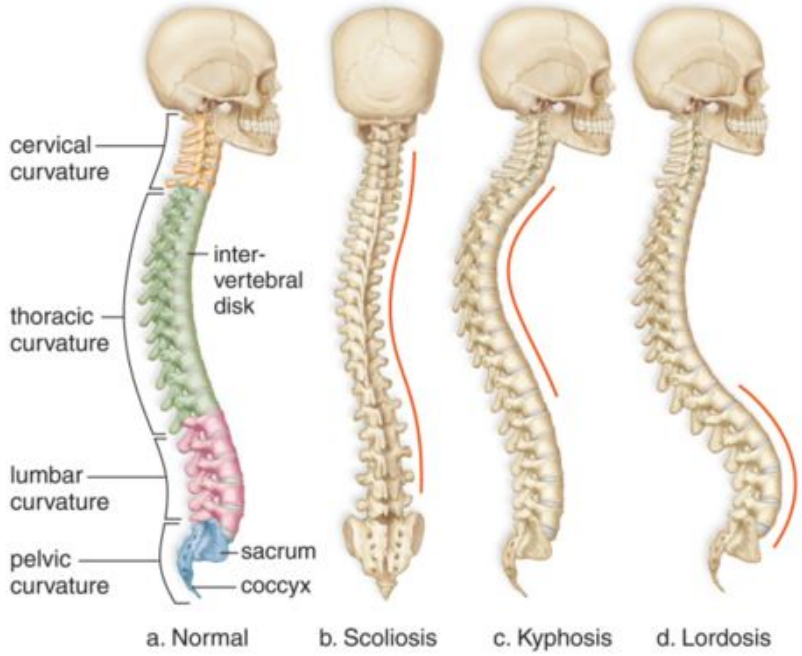

Figure 1.2: Spinal anatomy and several spinal diseases [2]

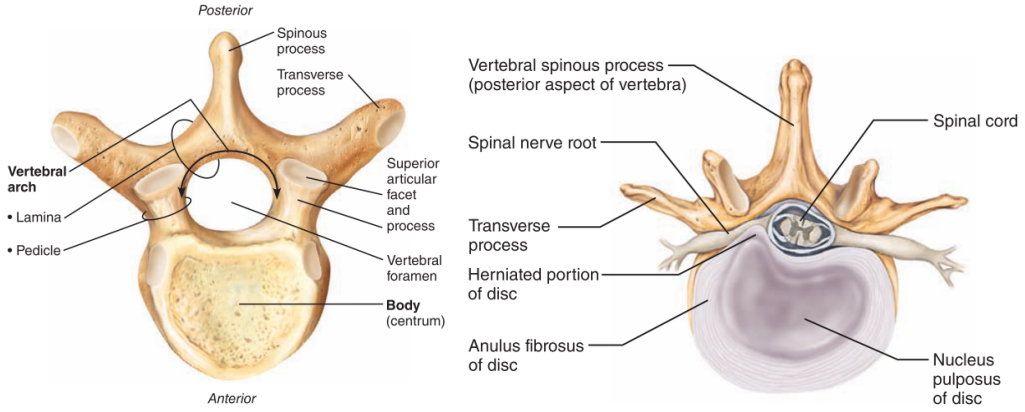

(a) Vertebral bone **(b)** Vertebral disk

Figure 1.3: Vertebral anatomy [3]

posterior direction for males 27.3 mm and for females 19.5 mm. Furthermore, Urrutia et al. [18] showed that the average diameter of the lumbar vertebral bodies in the medial-lateral direction is 43.6 mm and in the anterior-posterior direction 33.1 mm.

Vertebral bodies consist of a dense cortical shell surrounding a porous cancellous core. The thickness of the cortical shell at the anterior vertebral body region was found to vary greatly between studies and was determined to be between 0.2 and 0.4 mm by Ritze et al. and Eswaran et al. [19, 20], to be between 0.4 and 0.5 mm by Mosekilde [21], and to be between 1 and 2 mm thick by Swamy et al. [14, 22] for healthy bone.

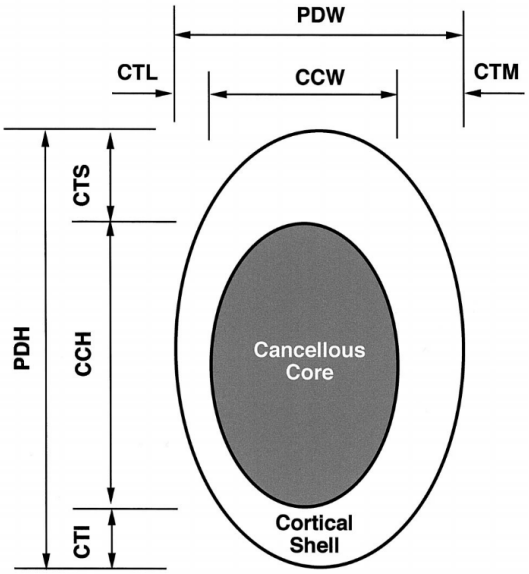

Figure 1.4: Generalized shape of a pedicle. *PDH = pedicle height, PDW = pedicle width, CTS = cortical shell thickness of the superior, CTI = cortical shell thickenss of the interior, CTL = cortical shell thickness of the lateral, CTM = cortical shell thickness of the medial, CCH = cancellous core height, CCW = cancellous core width* (adapted from [4])

The vertebral arch consists of one lamina with three processes (one spinous process and two transverse processes) and two pedicles. The spinal processes provide attachment points for muscles that stabilize the spine and enable trunk movement. The two pedicles protect the spinal cord and nerves laterally and also provide a bridge between the anterior and posterior part of the spine [16].

Just like other parts of the vertebra, the pedicle also consists of a dense cortical shell surrounding a porous cancellous core. The shape of the pedicle varies per vertebra but on average, the inner cancellous core is oval-shaped. The superior and inferior cortical shell thicknesses are approximately the same but the lateral cortical shell thickness is structurally lower than the medial cortical shell thickness. A simplified figure of the cross section of a pedicle is shown in Figure 1.4.

Subsequent vertebrae are separated by vertebral discs, the oval-shaped area indicated in gray in Figure 1.3b. The vertebral disc is made out of soft pad-like material and gives the spine its flexible, elastic structure. Furthermore, it damps forces acting on the spine. As can be seen in Figure 1.3, the spinal canal hosts the spinal cord. The spinal cord connects the brain to the rest of the body and is protected by the spine. Damaging the spinal cord might result in paralysis or chronic pain.

1.1.2 Bone structure and material characteristics

As mentioned previously, skeletal bone consists of a dense bony shell surrounding a porous core. The porous bone core is often referred to as *trabecular bone* or *cancellous bone* and contains less than 70% solid Bone Volume Fraction (BVF) [23,24] but typically only 10-50% [25].

The equation for the BVF is given in Eq. 1.1 and is defined as the volume of bony material (stripped from marrow) over the bulk tissue volume (both the hard bony part, as well as its voids). The cancellous bone is an open cellular structure, consisting of trabeculae [21,23,24]. Trabeculae are beam-like elements that make up the spongy structure of cancellous bone. The structure consists of 0.20-0.22 mm wide plate-like shaped vertical columns that are connected horizontally by slightly thinner, approximately 0.18 mm thick struts [21,23]. A visualization of such a cancellous bone structure can be seen in Figure 1.5. The trabeculae are not randomly oriented but are aligned along the direction of stress occurring in each bone in the body. In this manner, an efficient way of resisting forces is developed by nature.

$$BVF = bone\ volume/bulk\ volume \tag{1.1}$$

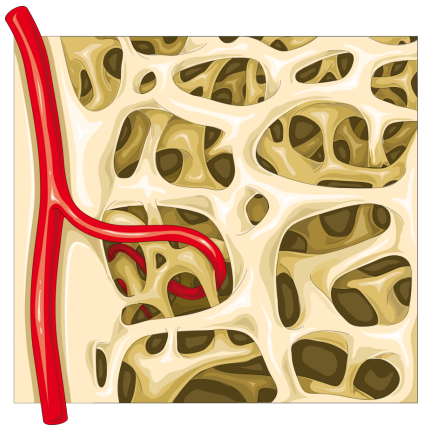

Figure 1.5: Structure of cancellous bone [5]

In the cavities of cancellous bone, a mixture of red and yellow bone marrow is situated, containing more hematopoietic cells and fat cells respectively [21,26]. In the case of adult vertebrae, the cavities are mostly filled with yellow bone marrow [14,26]. The bone marrow volume fraction of cancellous bone increases with decreasing solid BVF and varies between 30 and 95% of the total bone volume. According to Nouh et al. [26], yellow bone marrow consists of 80% fat, 15% water and 5% proteins. According to Sierpowska et al. [27], cancellous bone (the combination of solid bone and bone marrow) contains 18.8% water, 48.4% organic matter (of which 81.6% is fat, 17.8% is collagen and 0.5% is glycosaminoglycan (GAG)), and 20.5% inorganic matter (minerals). This results in a maximum total *(water+fat)* content in cancellous bone of 58.3% [27].

The Fat Fraction (FF) in tissue is defined as the fat content of a fatty aqueous mixture over the total water+fat content, as can be seen in Eq. 1.2 [22]. The FF of cancellous bone was measured with an MRI machine by Swamy et al. [14]. The fat fraction that results from MRI measurements is called the Proton Density Fat Fraction (PDFF) and ranged from 15 to 60% [14]. The fat fraction of cancellous bone was also measured with a DRS device several times by Swamy et al. [28]. The fat fraction that results from DRS measurements is called the Diffuse Reflectance Fat Fraction (DRFF) and ranged between 30 and 70% [28]. In several studies, the fat fraction of the cortical bone was measured as well, which was so small that it

was assumed to be negligible (0%) [8, 14].

$$FF[\%] = \frac{F}{F+W} \times 100 \tag{1.2}$$

According to Roy et al. [25], the material stiffness properties of the individual trabeculae are approximately the same as the cortical bone material stiffness properties. The E-Modulus of individual trabeculae differs per site and orientation (Superior-Inferior (SI), Medial-Lateral (ML), and Anterior-Posterior (AP)) and varies between 15.7 and 22.7 GPa, and the E-Modulus of cortical bone differs per site and orientation as well, and varies between 16.7 and 18.1 GPa. However, the material properties of the overall cancellous bone structure are significantly different than those of cortical bone because of the porous structure of cancellous bone. The structural characteristics of cancellous bone differ strongly per orientation [29]. This is due to the anistropic structure of trabeculae. Because the load in vertebrae is mainly carried in the SI direction, vertebral cancellous bone has a higher strength in that direction compared to the ML and AP directions. In Table 1.1, a summary can be found of the structural characteristics of cancellous bone in various studies. As can be seen in this table, the reported E-Modulus and yield strength of cancellous bone vary greatly. The reason for this is the high inter-patient variance. The structural properties of cancellous bone are among other things dependent on the patient-specific BVF, mineral density, age, sex, and disease. However, multiple studies have found a significant positive correlation between BVF and E-Modulus and yield strength [23, 29, 30]. For this reason, the BVF and additional measurement information of each study is mentioned in the table as well.

The dense shell that surrounds the cancellous bone is often referred to as *compact bone*, *lamellar bone* or *cortical bone*, and contains more than 70% solid BVF [23, 24]. The cortical bone encloses the cancellous bone and provides attachment points for ligaments, tendons and other connective tissue. Although most of the cortical bone is made up out of inorganic components such as mineral salts, it is riddled with canals hosting nerves and blood vessels. According to Carter et al. [24], cortical bone consists of 45% inorganic matter (minerals), 35% organic matter (of which 90-95% is collagen), and 20% water. In total, cortical bone thus consists of maximally 23.5% water+fat.

Since the definition of cortical bone requires the range of solid BVF to be smaller than in cancellous bone (namely 70-100%), the range of structural characteristics of cortical bone that have been measured by various studies is smaller as well. The density of cortical bone was determined to be 1800 kg/m3 by Gibson et al. and Carter et al. [23, 24]. A summary of the measured values of various cortical bone material characteristics can be found in Table 1.2. For simplicity, it is assumed that cortical bone has a BVF close to 100% thus the BVF is not mentioned in this table.

Although bone has been described as a dense cortical shell with a porous cancellous core up until this point, the border between cancellous and cortical bone is not so sharp. In reality, the porous structure of the cancellous bone changes gradually when approaching the cortical bone, resulting in gradually less cavities and more densely packed plate-like trabeculae. This is why cortical bone sometimes is referred to as compact bone. Such a transformation from

Apparent density [kg/m3] (BVF [%])	Direction	E-modulus [MPa]	Yield strength [MPa]	Measurement description	Reference
292.6-367.8* (16.3-20.4)	ML/AP	40-70	-	Human vertebrae, age 20	Mosekilde [31]
125.4-209.0* (7.0-11.6)	ML/AP	2-10	-	Human vertebrae, age 80	Mosekilde [31]
149 (7.6**)	ML	42.9	-	Human vertebra	Nicholson [29]
149 (7.6*)	AP	51.6	-	Human vertebra	Nicholson [29]
149 (7.6**)	SI	164.7	-	Human vertebra	Nicholson [29]
292.6-367.8* (16.3-20.4)	SI	120-150	-	Human vertebrae, age 20	Mosekilde [31]
125.4-209.0* (7.0-11.6)	SI	20-50	-	Human vertebrae, age 80	Mosekilde [31]
180 (10.0)	SI	344	2.0	Human vertebra, unwashed and still containing marrow	Morgan and Keaveny [32]
(20.8)	SI	129	13	Pig vertebra	Teo [30]
(15.0)	ML/AP	0.6-100	0.3-3	Columnar structure, human tibia	Gibson [23]
200 (11.0)	SI	30	2	Asymmetric cancellous structure of human tibial plateau and bovine femoral condyles	Gibson [23]
600 (33.0)	SI	200	20	Asymmetric cancellous structure of human tibial plateau and bovine femoral condyles	Gibson [23]
1000 (55.0)	SI	5000	50	Asymmetric cancellous structure of human tibial plateau and bovine femoral condyles	Gibson [23]
(11.0)	SI	150	2	Columnar structure, human tibia	Gibson [23]
(33.0)	SI	300	5	Columnar structure, human tibia	Gibson [23]
(55.0)	SI	700	10	Columnar structure, human tibia	Gibson [23]

Table 1.1: Summary of measured cancellous bone material characteristics researched in different studies. BVF = bone volume fraction based on trabecular bone material density of 1800 kg/m3, SI = superior-inferior, ML = medial-lateral, AP = anterior-posterior.

*The apparent density was not reported in the paper but is calculated here with the proven ash/apparent density ratio of 0.598 [33].

**The BVF was reported in the paper and was based on a different trabecular bone material density of 1962 kg/m3.

Direction	E-modulus [GPa]	Yield strength [MPa]	Ultimate compression strength [MPa]	Measurement description	Reference
-	18.5	-	-	No measurement description	Eswaran [20]
SI	17.0	-	193	Human femoral cortical bone, mean of a wide variety of ages (19-80)	Carter [24]
ML/AP	11.5	-	133	Human femoral cortical bone, mean of a wide variety of ages (19-80)	Carter [24]
N.M.	16.8	114.1	-	Human femoral cortical bone, mean of a wide variety of ages (19-89)	Carter [24]
SI	18.1	-	-	Human vertebral bone, 55+ age	Roy [25]
ML	16.9	-	-	Human vertebral bone, 55+ age	Roy [25]
SI	16	-	123	human cortical tibial plateau and bovine femoral condyles	Carter [24]

Table 1.2: Summary of measured cortical bone material characteristics researched in different studies. SI = superior-inferior, ML = medial-lateral, AP = anterior-posterior, N.M. = not mentioned

cancellous to cortical bone usually takes place within the first 3 mm of the surface of the cortical bone [22]. The area between the cortical bone and the cancellous bone is referred to as the *pre-cortical zone* [8, 22].

There are some cases in which the structural characteristics of bone deviate from the average. Osteoporosis refers to a group of diseases in which bone density decreases over time. Bones become light, porous and less strong. With osteoporosis, all bones experience a decrease in density, although the cancellous bone of vertebrae is most vulnerable to osteoporosis. Osteoporosis mostly appears with aging but can also be induced by a lack of exercise, a calcium-poor diet or a metastatic disease [21]. Research by Mosekilde showed that age-related thinning of the cortical shell takes place, decreasing the cortical shell to a thickness of 0.2-0.3 mm [21]. On top of that, the thickness and number of transverse trabeculae decrease with ageing, causing a decrease in BVF and surface density, resulting in decreased bone strength. The trabecular thickness for young healthy individuals is approximately 0.18 mm and the decreased trabecular thickness is 0.09 mm [21]. For example, research has shown that the ultimate strength of cancellous bone decreases from 4.6 MPa at age 20 to 1.2 MPa at age 80 in the SI direction and from 2.0 MPa at age 20 to 0.3 MPa at age 80 in the other directions [21]. Furthermore, the ash density of the cancellous bone decreases from 200 kg/m3 at age 20 to 100 kg/m3 at age 80 [21].

When a rise in temperature of bone takes place, the irreversible death of bone cells might occur, which is called thermal osteonecrosis [34, 35]. Both the temperature and the exposure duration are factors that determine osteonecrosis. Research showed that thermal necrosis occurs when bone is exposed to either a minimum temperature of 47°C for a minimum duration of 1 minute, or a temperature of 55°C for a minimum duration of 30 seconds [34–36].

1.2 Spinal fusion

There exists a wide variety of spinal diseases and disorders that cause pain, deformities, and dysfunction, thereby decreasing a patient's quality of life [37, 38]. Spinal fusion, also referred to as *spinal arthrodesis*, is a medical procedure that is often applied to release pain and treat spinal diseases. In spinal fusion, two or more vertebrae grow rigidly together by means of added bone graft, such that no movement between them is possible anymore. The vertebrae that are fused, are fixed relatively to each other during a spinal surgery to release loads, thanks to which the fusion process can take place. Figure 1.6 visualises the spinal fusion healing process.

The diseases that are most often treated with spinal fusion are degenerative diseases [38, 39]. Such degenerative diseases include degenerative scoliosis and degenerative stenosis (narrowing of the vertebral canal). Mechanical causes of pain or dysfunction such as spinal fractures or spondylolisthesis (the downward shift of a vertebra) can also be treated with spinal fusion [37, 39]. When an intervertebral disc prolapses, it can protrude into the spinal canal, pressing on nerves. This is called a *hernia* and can be treated with spinal fusion as well [3]. Spinal fusion can be applied in case of spinal instability either due to disease or after decompressive surgical procedures [37]. Lastly, patients with certain metastatic neoplastic pathologies can also be treated with spinal fusion [37, 40–42].

The number of spinal surgical procedures have increased enormously between 1998 and 2008

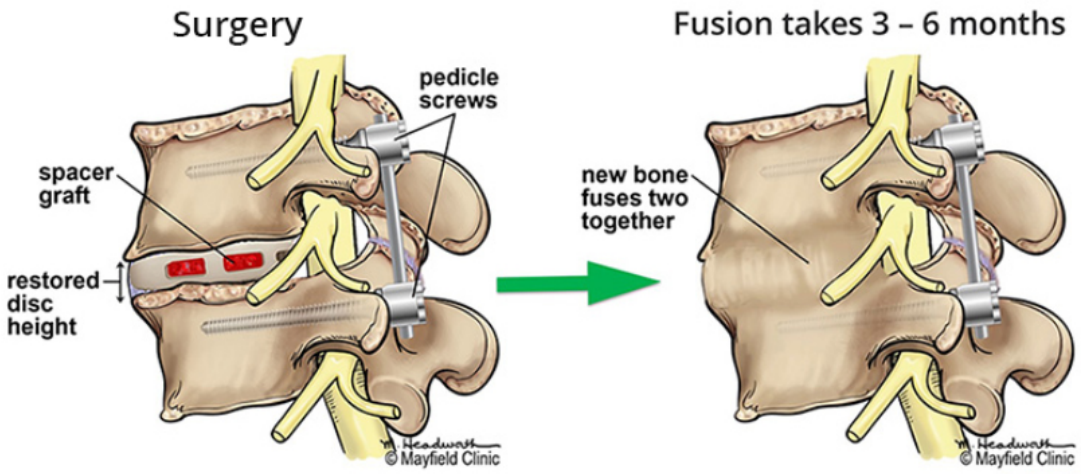

Figure 1.6: Spinal fusion healing process [6]

with 137% [38, 39]. This large increase in total spinal fusion surgeries is caused by multiple factors. First of all, the size of the aging population increased enormously, causing increased number of osteoporosis cases, and resulting in spinal deformities. Secondly, spinal fusion technologies such as pedicle screw fixation, artificial bone graft development, and minimally invasive surgery have advanced, which makes spinal surgery more reliable, widely applicable, and safe [38, 39].

The intervertebral disc that is made out of flexible material and that is naturally in between two vertebrae is replaced by autologous, allogenic or artificial bone graft [38]. The bone graft provides for a bone remodelling scaffold such that the two vertebrae can be fused together, similar to a bone fracture healing process [38]. To correct for deformities, stabilize the vertebra, or fix them relative to each other such that the healing can take place, an internal fixation structure is integrated in the spine. There are multiple techniques for fixating vertebrae. One of the earliest devices was designed by Harrington and spanned multiple vertebrae [37, 40]. Because of among other things, loss of fixation and bone fracture, a newer technique was developed by Luque [37, 40]. This device had a wire running through the spinal canal, making it more flexible and less prone to bone fracture. However, an increased risk of neurological damage arose. Because of this, a different approach was taken by means of hook-lamina segmental fixation, limited to cases with in tact laminae and facets.

The most recent advancements in bone drilling and spatial orientation devices allowed for the development of the Pedicle Screw Fixation (PSF) technique. This technique does not require intact posterior elements, does not require spinal canal intrusion, the fixation force can be directed, and the screws provide good rigidity [37]. The rate of successful fusion with PSF compared to other fusion methods is high, namely 70-97% [37]. PSF is currently the most often used technique for spinal fixation. This fixation approach will be explained in more detail in the following section [4, 37, 43, 44].

1.3 Pedicle screw fixation

As mentioned above, the most commonly applied spinal fusion technique up till now is PSF [4, 37, 44–49]. The procedure of placing a pedicle screw will be explained in the following section. After that, common complications with PSF will be discussed, leading to enhanced PSF solutions.

Spinal fusion using PSF is effective because pedicle screws have a relatively good fixation strength compared to other fixation techniques. The screws are placed through the pedicles because pedicles have a high percentage of dense cortical bone (30-50%) [4,44,50] and a beneficial cortical shell shape for screw tapping (oval). Because of the higher cortical bone content, pedicles have a higher overall bone strength. Research has pointed out that approximately 60% of the fixation strength of the thoracic and lumbar pedicle screws is contributed by the pedicle bone segment (compared to 15-20% by the vertebral body and 20-25% by the anterior cortex) [4, 20, 22, 45, 51].

1.3.1 Procedure

Prior to being able to fix two or more vertebrae to each other with plates and rods, anchor points should be attached to the vertebrae. These anchor points are the pedicle screws. The most common method for placing pedicle screws in vertebrae is the posterior approach. The patient is put under general anaesthesia and turned to the prone position (face down) before the procedure starts [52]. There are several ways to access the spinal region. The most invasive approach is the open approach in which the surgeon performs a standard posterior midline exposure to reveal the transverse process and the midline structures [7]. Less invasive approaches are the mini-open approach and the minimally invasive surgery (MIS), in which small incisions are made in the region of interest, through which surgical equipment is inserted into the patient's body.

The first step in placing the pedicle screws is selecting the entry point. The earliest technique for placing pedicle screws uses anatomical landmarks as reference points to correctly position the pedicle screws. This method is called the *free-hand* (FH) approach. More recent techniques make use of additional intraoperative medical imaging systems such as the C-arm system for more accurate screw placement. After the entry point has been determined, the second step is drilling through the cortical shell of the pedicle. When the cancellous bone is reached, a blunt probe is used to carve the correct trajectory inside the cancellous bone of the pedicle and the vertebral body. When the probe is fully advanced into the vertebra, the next step is to tap the hole while following the trajectory of the probe. The last step consists of inserting the screw into the tapped hole.

It was shown that penetration of the anterior lumbar vertebral body cortex during pedicle screw placement increases screw pull-out strength up to 16-25% [37, 45]. However, anterior cortical breach increases the risk of vascular injury. For this reason, the recommended screw insertion depth is 50-80% of the vertebral body [37, 45].

During the PSF procedure the surgeon uses an orthopaedic drill to make the screw hole. The axial load that is required to drill through cancellous bone differs from the load that

is required to drill through cortical bone at the same feed rate and rotational speed [35]. The force sensed by the surgeon can thus be an indication of the drill tip location inside the vertebra and can be used as a warning signal for cortical breach. Three factors that affect the axial force on an orthopaedic drill are the drill rotation speed, the feed rate, and the drill diameter and geometry [34, 35, 53–56]. According to Duperron et al. [54], the axial load decreases with a factor of 5 when drilling through cancellous bone compared to cortical bone. Marouf et al. [53] have shown that, when drilling through a porcine femur with a feed rate of 2 mm/s, a rotation speed of 3300 rpm and a drill bit diameter of 2.5 mm, the axial force on the drill in the cortical bone peaks at a value of 15-23 N, and the force in the cancellous bone varies between 0-5 N. Hu et al. [55] showed that drilling in bovine vertebrae with a feed rate of 0.5 mm/s, a rotational speed of 8000 rpm, and a 3 mm diameter drill bit resulted in an average axial force of 4-8 N in the cortical bone and 1-4 N in the cancellous bone. Research carried out by Kan [34] used a Sawbones cancellous bone phantom made out of rigid cellular polyurethane foam combined with a cortical bone plate made out of short fiber filled epoxy and measured the axial force on the drill. With a feed rate of 1 mm/s, a rotational speed of 500 rpm and a drill bit diameter of 2.7 mm, the resulting force in the cancellous bone phantom varied from 0-10 N with a mean around 6 N and the force in the cortical bone peaked at 48 N.

1.3.2 Complications

Spinal fusion surgical outcomes vary greatly, which could be caused by the fact that surgical decision-making varies between surgeons [45, 57]. Next to that, patient-specific variables such as anatomic landmarks, bone density, disc-space penetration, and pedicle size, shape and angulation can vary greatly [43, 45, 46, 49, 58, 59]. This makes the procedure of pedicle screw placement a difficult process, which requires extensive prior knowledge and experience [4, 7, 43, 45, 49, 59].

Spinal fusion surgery has shown increased number of complications compared to other surgeries [7, 39, 45–47, 57, 57–61]. During spinal fusion, extensive dissection, longer operative times, increased risk of death, and increased risk of blood loss have been observed [57]. By Vaccaro and Garfin [37], complication rates up to 63% have been reported. Out of these 63%, approximately 5% of the complications were caused by misplacement of pedicle screws. Misplacement of pedicle screws can result in cortical breach, which is defined as the unintended puncture of the vertebral cortical shell during pedicle screw placement. Common examples of pedicle screw breach are depicted in Figure 1.7. In 3-30% of the cases, screw fixation failed due to pedicle screw breakage [37].

When cortical breach occurs, the risk of neurological damage is high because the screws are placed in very close proximity to the spinal canal [4, 43, 45–47, 57, 60]. On top of that, as explained in Section 1.1, around the spine there is a high concentration of vulnerable blood vessels [49]. Damaging these blood vessels during PSF could result in permanent injury as well. Especially PSF in the thoracic spine is challenging because of the small vertebral dimensions [4, 7, 58]. Mirza et al. [7] have reported cortical breach in the thoracic spine in 16-54% of the cases.

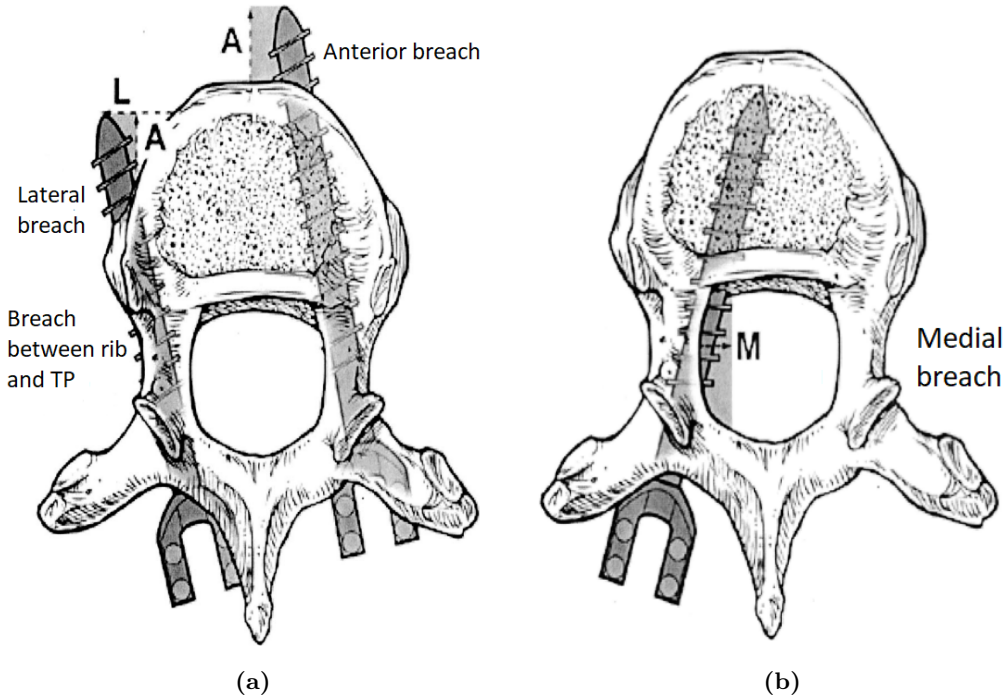

Figure 1.7: Examples of pedicle screw breach (adapted from [7])

Another complication that occurs during spinal fusion is reduced fusion quality due to osteoporosis. A large number of medical indications for pedicle screw fixation are caused by aging and osteoporosis. With osteoporosis, the density of bone decreases, which also decreases bone strength and the self-healing ability of the bone. This in turn causes spinal conditions. However, pedicle screw fixation relies on screw anchoring in bony structure. Because of the reduced bone strength, there exists an increased risk of pedicle screw loosening for patients suffering from osteoporosis [62, 63]. Because of the reduced self-healing ability of the bone, there exist an increased risk of fusion failure as well.

1.4 Enhanced pedicle screw fixation

Because of the high rates of complications during PSF, several techniques were developed to enhance PSF. Firstly, the trajectory of pedicle screws can be improved to reduce risk of cortical breach. Secondly, the fixation strength of screw can be improved.

1.4.1 Guided drilling

Global guiding

In order to improve pedicle screw placement, several devices were developed to track down the location of pedicle screws relative to vertebra parts. These global imaging techniques provide spatial orientation. Intraoperative spatial orientation can be very useful, especially in spinal surgery, because the procedure of PSF is difficult due to the inter-patient anatomic

variations [43, 45, 46, 49, 58, 59]. Even though a surgeon would be highly trained and familiar with the spinal anatomy, anatomic variations due to deformed spines in patients with scoliosis or spondylolisthesis might cause complications during PSF without sensor guidance [45].

First, intraoperative fluoroscopy was introduced, which still remains the most common global guiding tool for pedicle screw placement [40, 43]. Although this resulted in reduced pedicle screw misplacement, fluoroscopy makes use of ionizing radiation, which is harmful for both the patient, as well as the surgical staff [40, 43]. For this reason, other guidance tools such as intraoperative computational tomography-based (CT-based) devices were developed [40, 43]. As shown by Schwarzenback et al. [61], complete preoperative CT scanning resulted in a 2.7% pedicle perforation rate, while incomplete preoperative CT scanning resulted in a 25% pedicle perforation rate. Van Dijk et al. [64] reported a comparable pedicle screw breach rate out of the safety zone of 2 mm of 2.1% by use of a pre-operative CT. Solomiichuk et al. [42] have reported the use of a CT-based robot for pedicle screw trajectory determination, which had a similar screw placement accuracy as fluoroscopy-based guiding solutions. However, CT images still require expert interpretation, which increases operating times and result in calibration errors [43, 65]. Overall, the use of global navigation systems are expensive, time-consuming and require configuration before surgery [43, 58, 65].

Local guiding

To eliminate such drawbacks, the most recent studies focus on the use of local guiding systems. These local guiding systems do not provide the pedicle screw position relative to the vertebra, but rather provide information about the tissue composition at the tip of a probing device. In this manner, the location of the tip of the device can be deduced through tissue differentiation.

Most intraoperative guiding systems are optical sensing systems, including Raman spectroscopy, diffuse reflectance spectroscopy (DRS), fluorescence spectroscopy (FS) and hyperspectral imaging (HSI) [66]. All these optical systems are non-harmful and most (except for FS) don't make use of administered contrast agents. Because of the simple and low-cost setup and short spectral acquisition time of FS, DRS and HSI, these techniques are applied often for local guiding. When comparing DRS and FS, FS has some additional drawbacks. It either suffers from low signal-to-noise ratio and limited applicability (autofluorescence), or potential toxicity, long waiting times and a limited temporal window (FS with contrast agent). If more detailed information about tissue constituents is required, the slightly more complex technique of Raman spectroscopy is usually applied. However, the signal acquisition time for Raman spectroscopy is much higher due to which it can not be used intraoperatively in real time [66].

A research group from the TU Delft has performed several studies in which the DRS signal of reference phantoms, *ex vivo* human vertebrae, and *in vivo* porcine cadavers was measured. The reflectance signal obtained in the cancellous bone was significantly different than the signal obtained in the cortical bone, as well as the signal obtained in the surrounding tissue. An example of the resulting spectra is shown in Figure 1.8.

Because the DRS signal differs per tissue type, it can be used to differentiate between tissues. The most simple approach is to use raw spectra and compare the spectral shape relatively [67].

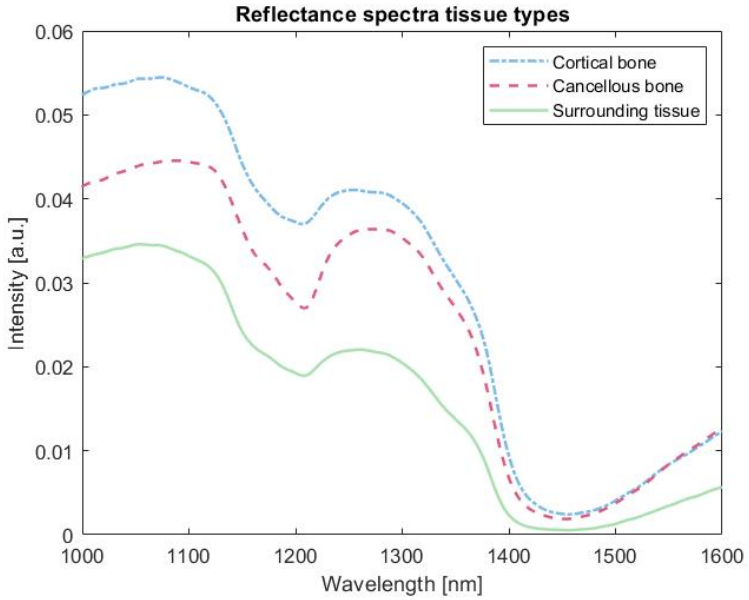

Figure 1.8: Diffuse reflected spectroscopy measurements of different types of human tissue as a function of wavelength. The measurements were obtained by inserting a DRS probe on human cadavers all the way through the pedicle of the vertebra till cortical breach occurred, and measuring the reflectance signal at specified depths with known tissue types. (data obtained from [8]).

One could also take it one step further and construct the physical properties of the sampled material (the absorption and scattering spectra) from the DRS signal and compare them to prior known tissue optical properties [67]. The most intensive approach is to use the constructed scattering and absorption spectra in combination with known scattering and absorption spectra of chromophores to estimate the sample tissue composition [66–68]. The output would be an estimation of the volume percentage of biological substances present in the sample tissue, which can be compared to tissues with known compositions [66].

A research group from the TU Delft has developed an algorithm that employs the most extensive classification method by fitting standard chromophore absorption and scattering spectra in DRS signal spectra [69]. The algorithm combines standardized spectra of tissue components such as blood (hemoglobin), water, and fat, to estimate the composition at different locations in the test specimen. The output of the fitting algorithm is an estimation of the relative content (volume percentage) of components present in the specimen, such as the (water+fat) content, the blood content and the FF. Based on the spectra-derived fitting parameters in combination with prior knowledge about the composition of various tissue types, the tissue type at a specific measurement location can be identified.

The fitting algorithm was used in previous studies to identify the boundary between cancellous and cortical bone, based on the estimated FF of the tissue [8, 14, 28, 70]. Out of all the output parameters of the algorithm, the FF was chosen as a classification parameter because this resulted in the most reliable and stable classification results [69]. When looking at the absorption spectrum of water and fat in the Near Infra-Red (NIR) spectral range, depicted in Figure 1.9, one can notice that the dominant absorber for wavelengths above 1300 nm is

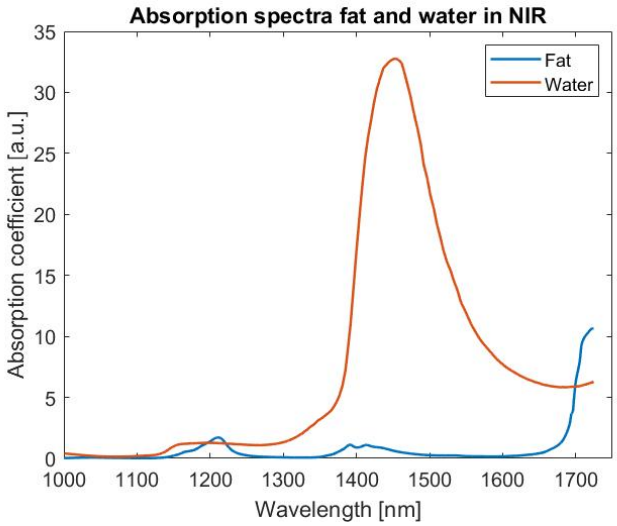

Figure 1.9: Absorption spectra of fat and water in the spectral range 1000-1724 nm

water. Because of least-squares fitting over the entire spectral range of the measured signal, water will most likely be fitted accurately. When comparing the absolute absorption at 1200 nm, fat is dominant over water which increases the chance that fat will be fitted accurately as well. One of the limitations of this algorithm is that the error of the estimated absolute content value becomes bigger with decreasing fiber distance. Since this small fiber distance fitting error is present in both water and fat estimation values, the FF parameter (Eq. 1.2) resulted in a more stable differentiation parameter than the absolute fat and water content estimation values.

Due to the short acquisition time of DRS-based guiding, it has potential for real time tissue distinction. Tissue distinction is a very relevant functionality for the application of PSF because the boundary between cancellous and cortical bone must be identified accurately in real time during hole drilling. Therefore, DRS in combination with a fitting and classification algorithm could be used in a PSF guiding system.

Next to this, electrical conductivity could also be used to provide local guiding. The setup of an EIS system is simple and cost-effective, the tissue distinction accuracy is high and the machine can be small. A drawback could be that the measurement is superficial and the probe has to be in contact with the sample [66]. An example of the integration of EIS in surgical devices for PSF is the dynamic surgical guidance (DSG) technology developed by Allaoui et al. [43]. A probe was developed that measures the conductivity of tissue at the tip of a probe. The conductivity spectra are translated into audio and light signals that are presented to the surgeon. Tissues can be recognized by the frequency and pitch of audio signals and warning lights. The accuracy of the screw placement increased from 92.2% for the free-hand approach to 95.4% for the DSG approach. Furthermore, the device helped to decrease the number of severe lateral breaches, reducing complication rates [43]. This technique was commercialized as the PediGuard device (SpineGuard, Vincennes, France).

Lastly, a technique has been developed by Hu et al. [55] that combines the high stability and accuracy of robotic surgery with operating force feedback by incorporating a 6 degrees-

of-freedom force/torque sensor into a pedicle drilling device. This enhanced drilling device is able to recognize different materials that it encounters during vertebra hole drilling by measuring the force on the drill bit. Initially, a high force is required to drill through the outer layer of cortical bone of the pedicle. After breakthrough, the force decreases because the drill is in the porous cancellous bone. The transition zone from cancellous to cortical bone can again be recognized by an increase in force such that the drill rotation speed and feed settings can be decreased in time.

1.4.2 Enhanced screw placement

Even if the pedicle screw placement procedure was carried out correctly, sometimes, the procedure is not successful because the screw fixation strength was not sufficient [46]. Next to that, if the pedicle screw placement procedure was successful and no cortical breach occurred, in some cases, post-operative pedicle screw loosening takes place [41]. Most often, the reason for intraoperative or postoperative screw loosening is associated with poor bone quality due to osteoporosis [41, 46].

There are a few solutions that can already be applied when insufficient screw fixation strength is suspected. Fist of all, the depth of screw insertion affects fixation strength. In normal, strong bones, the recommended insertion depth of a pedicle screw is approximately 50-80% of the vertebral body [37, 45]. Increasing the insertion depth till anterior cortex breach occurs may increase fixation strength with 16-25%, but it also increases the risk of neurovascular injury. On top of that, it was found that cyclic loading of pedicle screws that are fixated in pedicles as well as the anterior cortex induced increased risk of pedicle fracture or screw bending [71]. For this reason, anterior cortical breach is only aimed for in patients with poor bone quality [37, 45, 71].

Another way of increasing pullout strength of pedicle screws is with the insertion of cement into the cancellous bone. The most frequently used cement is Polymethylmethacrylate (PMMA) [45] [71]. The usage of PMMA was found to increase pullout strength with up to 257% [71]. PMMA is inserted in the screw hole as a cement and hardens out after the screw is inserted. Because curing of the cement is an exothermic reaction, the cement can heat up to 110 °C during hardening. Due to this, the risk of necrosis of bone tissue and surrounding neural tissue is severe. On top of that, there exists the risk of leakage of the PMMA resin before hardening, possibly causing neural damage. Furthermore, it is believed that long term exposure to PMMA can result in toxicity. Lastly, PMMA can not be removed from the cancellous bone without causing severe and irreversible damage [71]. For all the reasons mentioned above, PMMA augmentation for PSF is controversial and will only be applied if the benefits outweigh the potential risks [71].

A novel high-potential method for enhancing PSF strength that does not induce increased risks is curved trajectory drilling. Previously, it was found that the pedicle resists most of the forces subjected to the screws because of the high fraction of cortical bone in the screw trajectory spanning the pedicle, as opposed to the low fraction of cortical bone in the screw trajectory spanning the vertebral body [4, 20, 22, 45, 51]. To increase fixation strength, the screw could be placed along a different trajectory, containing a higher fraction of cortical bone. Since the vertebral body consists of a porous cancellous core surrounded by a shell

of dense cortical bone, it would be advantageous to fixate the pedicle screws in the shell of the vertebral body. To accomplish this, the trajectory of the pedicle screws must be curved, following the outer contour of the vertebral body. Research is currently being conducted on how to drill such a curved screw hole, and on how to fixate flexible screws into the curved hole.

3D steering of medical device has been researched for several applications already. For example, the *Sigma* catheter was developed by Ali et al. [72]. This catheter is developed for heart surgeries and consist of two steerable segments, each having two degrees of freedom. The tip diameter is 3 mm and the segments consist of steering elements. Steering per segment is controlled independently by pulling four cables. The length of the cables is controlled by manual movement of joysticks.

Furthermore, a steerable device consisting of four steerable segments and a total of eight degrees of freedom was developed by Sakes et al. [73] for the application of improving minimally invasive surgery dexterity. Tip steering is based on a similar principle as the *Sigma* device. Each segment is actuated by four cables. The device could in the future be used to safely navigate through delicate environments and allow for tissue identification [73].

The *Ovipositor* steerable needle is based on a different working principle [74, 75]. The needle is inspired by the ovipositor of wasps and consists of seven wire valve elements. The needle is self-propelling by pulling and pushing the valves separately, resulting in a net forward propelling force. The total diameter of the tip is only 1.2 mm and the propelling mechanism enables the tip to be very long and slender without buckling.

1.4.3 Guided steerable surgical drill

A research group of the TU Delft is currently developing a device that combines guided drilling with curved drilling to improve pedicle screw fixation strength. This device consists of a drill bit with integrated sensory system. An example of how the guided steerable drill could look like is presented in Figure 1.10. The sensor system is based on DRS and provides real time feedback on the drilling trajectory, based on measured spectra of the tissue at the tip of the drill bit. Since cancellous bone has a microstructure composed of cavities filled with bone marrow, the overall content of cancellous bone is significantly different from that of cortical bone [14]. When approaching the cortical shell, the density of the cancellous bone increases, the number of cavities decrease, and the total marrow fraction drops [14, 22]. When the cortical shell has been reached, the tissue consists nearly only out of solid bone [14]. By making use of DRS at the drill tip, an estimate on the distance from the drill tip to the cortical shell can be made. With this method, a drilling trajectory inside the vertebral body, along the cortical shell can be maintained, to provide optimal screw fixation. On top of this, a drilling system is being designed that is able to drill a curved path accurately. Next to the curved path drill, a compatible flexible anchoring mechanism is being designed that will be inserted into the curved hole to provide attachment points for the stabilizing rods and plates.

The guiding system operates based on the DRS sensing technique, discussed in detail previously [8, 28, 69, 76, 77]. The device consists of one emitting optical fiber and one collecting optical fiber, each having a core diameter of 200 μm. The center-to-center distance of the two optical fibers is 1.22 mm. The emission source is a tungsten halogen broadband light source

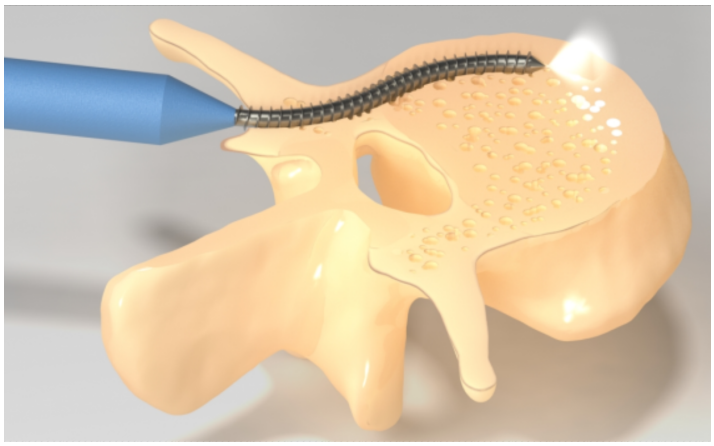

Figure 1.10: Possible design of the guiding steerable surgical drill currently being developed by the TU Delft [9]

which emits light in the Visible (VIS) and NIR spectrum (together 360-2500 nm). The collecting system consists of two spectrometers which together operate in a predetermined range which can be varied between 400 and 1600 nm. The acquisition time of each measurement can be set to 50-500 ms.

The raw signal is post-processed with a smoothing algorithm, and an in-house developed algorithm estimates various parameters from the collected signal such as the absorption and scattering spectra. The fitting algorithm is based on prior knowledge of the absorption spectra of the main components of the tissue, namely blood, oxygenated blood, water, and fat, and additional desired components such as collagen. When a collected spectrum is inputted into the algorithm, a non-linear least squares (Levenberg-Marquardt) optimization process is being carried out that fits a linear combination of the standardized spectra of the tissue components into the measured signal [8, 78]. Using this optimization method, the estimated component fractions are given as output. The fitting model is based on the Farrell model equations and adjusted to compensate for the fiber distance [67, 79]. This method of using DRS for tissue identification is the most detailed one, deducing tissue component fractions by use of prior obtained standardized component spectra [67].

The design of the mechanical part of the steerable surgical drill is still in an early phase. The mechanical design is subdivided into two components, namely steered drilling and flexible anchoring. Since there already exist techniques to drill curved tunnels for other applications, the research focus is on the novel challenge of anchoring a flexible screw-like device in a curved hole. A first prototype is not yet developed.

1.5 Problem statement and design objective

Since spinal surgery numbers are rising, the need for qualified spinal surgeons increases as well. However, the previous section discussed why spinal surgeries, including PSF, are generally difficult to carry out and require extensive training. Because of the high level of difficulty, a large amount of complications still occur, causing patient discomfort, pain or even nerve injury.

Next to the need for extensive surgical staff training, this creates high research momentum for enhanced spinal surgery devices, such as the devices discussed above. All of these devices must pass through a large series of medical tests during the development, production, and testing phase, before they are approved to be used in the operating room on patients.

The time span of development, production and testing of medical devices depends on the risk of the device. In case of a high risk procedure like PSF, it is likely that such a guided steerable drill device described in the previous section, is categorized in the highest medical device class (the highest risk to the patient). The time between concept and approval of such a device can take up to seven years [80]. The newly developed device must first pass a number of preclinical bench tests and animal tests, before it proceeds to clinical testing. The cycle of preclinical tests typically takes 2 to 3 years and costs between 10 and 20 million US dollars [80].

In the case of a guided steerable drill, the guiding system as well as the steerable drill system should be tested frequently and eventually simultaneously. To test the optical guiding system and the drilling system separately, various optical phantoms, optical phantom recipes, or structural bone phantoms are available. However, to accomplish simultaneous testing of the guiding system and drilling system in the preclinical trials, currently the most reliable test setup comprises of an animal vertebra. This brings about several disadvantages such as the fact that animal vertebrae are anatomically not the same as human vertebrae and their compositions differ as well, inducing testing errors. Furthermore, testing on living animals brings about a heap of ethical issues and considerations. On top of that, excised animal vertebrae have a limited preservability and the accuracy of measurements decrease as the sample resides longer out of the body of the animals. Lastly, the process of obtaining animal vertebrae similar to human vertebrae is cumbersome and expensive, and testing on tissue samples is not allowed on every testing site [81]. For all the reasons mentioned above, a more accurate, less expensive, less cumbersome, and more preservable alternative to animal vertebrae testing would be highly valuable for enhancing the development and approval process of PSF medical devices.

Furthermore, the amount of training hours before a surgeon becomes qualified to perform PSF is high, because the spinal region varies anatomically between patients, and PSF is a complicated procedure. A closely simulating synthetic bone phantom would be the optimal way of performing a high number of training sessions in an easy, effective and low-stress environment, without having to use animal vertebrae [81, 82]. Lastly, phantoms are perfect objects to compare devices or techniques on, because they provide an objective, standardized reference for repeatable measurement results. Measurements on real vertebrae would be more inconsistent and unreliable because two vertebrae will never have exactly the same characteristics.

Therefore, the objective of this research is **developing a bone phantom that simulates a human vertebra and that can be used for optical guiding system testing as well as structural steerable drill testing, which is competitive on the market, highly stable over time and easy to produce and handle.**

1.6 Report outline

This report consists out of three parts. The first part discusses all the knowledge that is required to understand the problem and to introduce the novel concept (Chapter 1). Furthermore, the first part contains an overview of the state of the art phantoms (Chapter 2), and the problem analysis (Chapter 3), including the research goal, functional requirements, and requirement quantification. The second part of the report builds upon the functional requirements by generating concept solutions and selecting the most promising concept (Chapter 4). After that, preliminary tests are carried to validate the feasibility of the concept (Chapter 5). This brings us to the third and last part of the report in which the concept is worked out into a detailed design tool and an example design is validated (Chapter 6). Lastly, the highlighted results, impact, limitations, and recommendations are discussed (Chapter 7).

Chapter 2

State of the art

There are several phantoms or phantom recipes available that mimic different human tissue types. To structure the state of the art phantoms and phantom research for the current application, a division is made into available phantoms for mimicking the optical properties of tissues (optical phantoms) and phantoms for mimicking the structural properties of bone (structural bone phantoms). A description of these phantoms and studies will be given in this chapter.

2.1 Optical phantoms

A wide variety of optical phantoms are available that mimic different human tissues. Generally, optical phantoms consist of a base material enhanced with scattering agents and absorption agents [82, 83]. In this manner, both scattering and absorption characteristics of the phantom can be controlled separately and precisely. With early optical liquid phantoms that consisted of milk, non-dairy cream, or blood suspensions, it was not possible to induce inhomogeneous optical material characteristics. Because of this, solid optical phantoms were developed that immobilized the absorption and scattering components. This section will discuss common solid base materials and additives.

2.1.1 Base materials

The base material of optical phantoms can be hard, flexible, or soft. Hard plastic base materials that are often used, are Polyurethane (PU), polyester, Polyvinyl Chloride (PVC), or epoxy [82]. Phantoms with a PU base material have been reported to be superior in use over polyester phantoms because of their compatibility with NIR absorbing and scattering dyes [82,84]. The curing time of polyesters can be extremely long as well (up to one week) [84]. PU and PVC exist in a wide variety of stiffnesses and can range from very hard material to flexible material. PU, polyester, PVC and epoxy phantoms are usually produced through

casting, by mixing a resin and a hardener, degassing the mixture, pouring it into a mould, and curing it. Another plastic that can be used as a base material is silicone, which has a similar casting production process to PU, polyester and epoxy [82]. Silicone phantoms range from a harder, flexible rubber-like texture to a soft gel-like texture. Silicone phantoms are stable and have a refractive index similar to soft tissue [85]. Flexible and deformable silicone phantoms can be advantageous over hard plastic phantoms when contact is required between the probe and the tissue [85]. One type of silicone is polydimethylsiloxane (PDMS), which is a rubber-like or liquid resin organic silicon-based polymer that is used in a very broad range of applications such as the food industry and the medical industry.

Softer phantom base materials are gelatin, agar, and polyvinyl alcohol (PVA) [82,86]. Gelatin and agar are natural base materials and the phantoms are produced by mixing the gelatin or agar powder with heated water and letting it harden at reduced temperatures. Phantoms based on gelatin and agar are the cheapest solid phantoms. The gelatin or agar raw material price for a 10x10x10 cm phantom (based on a 6% gelatin or agar solution), is approximately €1.50 [87].

PVA is a water-soluble synthetic polymer. A PVA phantom is produced by mixing PVA powder with water at elevated temperatures. The stiffness of PVA phantoms can be altered by going through freeze/thaw cycles. During these cycles, the phantom is frozen for 10-12 hours and slowly defrosted again till room temperature, due to which the number of cross links increase and the stiffness goes up. Because of the cycles, the intrinsic scattering characteristics change. When this is undesired, dimethyl-sulfoxide (DMSO) can be added to the phantom in order to keep it transparent [82,86]. Another way of increasing the amount of cross links is adding sodium trimetaphosphate (STMP) to the PVA base material [86]. NaCl, NaOH, or epichlorohydrin (ECH) can be added to a PVA suspension to improve internal interaction between PVA chains. This results in a decrease in curing time and an increase in homogeneity [86]. The price of PVA is higher than that of gelatin or agar. The raw material price of a 10x10x10 cm PVA phantom (based on a 10% PVA solution) is approximately €41,60 [88].

Because gelatin, agar and PVA phantoms are composed of water and have a low melting temperature, they are unstable and suffer from dehydration over time, which alters the concentration of additives [82, 86, 89]. Multiple studies have mentioned a limited shelf life of refrigerated optical hydrogel-based phantoms ranging from a few hours to a few days [90–92]. In order to increase the melting temperature of gelatin, formaldehyde can be added to gelatin phantoms, thanks to which they can be used at room temperature [82,86].

2.1.2 Scattering additives

There exists a wide variety of scattering agents in a large range of wavelengths. First of all, fat in the form of lipid microparticles can be used as a scattering additive in phantoms. The advantage is that the scattering characteristics of lipid particles are assumed to be similar to human tissue scattering characteristics because the bilipid membrane of cells and organelles is thought to cause light scattering in tissue. The disadvantage is that fat is hydrophobic which means that it does not dissolve well in an aqueous suspension [93]. For this reason,

thorough mixing is required before usage, and homogeneity only lasts for hours when used without gelling agent [82]. Fat can either be bought in the form of Intralipid (or nutralipid, liposyn) [82,86], or extracted from animal tissue that is commercially available, which is more time-consuming. The advantages of using Intralipid are that the content of this suspension is highly consistent, it is clinically approved and widely available in every hospital, and the optical properties are well-documented [94]. The disadvantage of Intralipid is that the maximum fat content of the suspension is 20%. Shokoufi and Golnaraghi [94] used Intralipid in combination with India ink to mimic the optical characteristics of a breast tumor. Another example of a fat-based scattering phantom is the phantom produced by Avtzi et al. [95]. A stable optical mouse phantom was produced by mixing Intralipid and India ink in an epoxy resin. The mixture was then poured into a mold to cure. The absorption and scattering spectra were stable over a period of several months.

Commonly used synthetic scattering agents are titanium dioxide (TiO2), aluminum oxide (Al2O3), or barium oxide (BaO) [82, 86]. These scattering agents are used in paint and coatings. They are relatively inexpensive and widely available. However, TiO2 tends to precipitate during hardening of the gelling agent or when used in a liquid phantom if not stirred well enough, causing material inhomogeneity. It was shown that TiO2 particles uniformly disperse after 3 hours of steering [84].

In some phantoms, polystyrene microspheres are added as scattering agents. The scattering is not induced by the chemical structure of the polystyrene, but by the microstructure of the sphere. Because manufacturing of the spheres happens in a controlled matter, the optical properties of polystyrene microspheres are highly consistent, but the cost is higher too [82]. Polysciences Incorporated sells 15 ml of 2.5% weight percentage aqueous solution of microspheres for approximately €180. Polystyrene microspheres are highly stable and they can be reused if desired [82]. Other microstructure-based scattering agents are quartz glass beads. These glass beads induce scattering while preserving the optical clarity of the material [86].

Lastly, materials can be used that scatter light intrinsically. For example, Delrin is an acetin plastic with high scattering characteristics and low absorption characteristics [96]. Because of this, the optical characteristics are similar to human fat tissue. A study by Shokoufi and Golnaraghi [94] used this Delrin material to mimic healthy breast fat tissue.

2.1.3 Absorption additives

There also exist a wide variety of absorption agents in a large range of wavelengths. First of all, since the sensing system to be tested on the phantom differentiates cortical and cancellous bone based on the fat fraction, fat can be used as an absorption additive. The advantage of using fat is that the absorption characteristics are very similar to those of fat in human tissue. This increases the chance that the optical measurements of a fat-based phantom are representative for *in vivo* measurements. However, just like when using fat as a scattering agent, the disadvantages are that it is not well soluble in water, which might cause inhomogeneity over time when used without gelling agent. Furthermore, phantoms with a high fat content have a limited shelf life because of deterioration due to bacterial growth[1] [89].

[1] "Private communication PhD candidate M. Losch"

If one seeks to replace the absorption characteristics of fat in of human tissue with similar absorption agents, ink or molecular absorbing dyes can be used [82,86]. The most commonly used ink is India ink, which is composed of a suspension of carbon particles and results in a relatively flat absorption spectrum across NIR light range [82]. Furthermore, its solubility in water is good [94]. A disadvantage of using India ink is that it also produces significant scattering in the VIS light range [83]. A wide variety of ink types are available that have wavelength-dependent absorption spectra (such as 900NP ink). Examples of studies that use black India ink to simulate tissue absorption spectra are the studies conducted by Shokoufi and Golnaraghi and Royston et al. [83,94].

Black plastic colorant (BPC) can also be used as an absorption agent for in plastic-based phantoms. This agent consists of a plasticizer, mixed with carbon black molecules. Many studies have reported the use of fluorophores for tissue absorption simulation, and hydrophilic molecules are used most often [82].

A study by Shokoufi and Golnaraghi [94] have used a protein assay reagent (PAR) combined with bovine serum albumin (BSA) to mimic the specific absorption coefficient of oxygenated hemoglobin (HbO2) at 750, 800, and 850 nm [94].

There are also off the shelf optical phantoms available. INO is a company specialized in manufacturing solid, highly stable optical phantoms [97]. These phantoms are made out of PU solid plastic, carbon black is added as an absorption agent, and TiO2 is added as a scattering agent. The wavelength range of desired optical properties is 450-940 nm. Custom optical phantoms can be manufactured with a absorption coefficient between 0.05-1 cm^{-1} and a reduced scattering coefficient between 5-25 cm^{-1} for one specific reference wavelength. The maximum phantom dimensions are 11x11x11 cm. The price of such optical phantoms varies depending on the size between US$1300 and US$2000. The optical stability and preservability of the phantoms has been reported to be over 10 years.

2.2 Structural bone phantoms

2.2.1 Classic manufacturing

Several companies and research groups have developed bone phantoms mimicking bone material characteristics for structural testing. One of the companies that manufactures structural phantoms is *Sawbones*. They offer base materials mimicking cortical bone and base materials mimicking cancellous bone, as well as a composite bone, combining cortical and cancellous bone. The cortical bone material is made out of solid polyurethane foam or short fiber filled epoxy (laminated in sheets on top of the desired cancellous bone). Various types of cancellous bone are available: solid rigid foam, cellular rigid foam (mostly closed cell), and open cell rigid foam (mostly open cell). The foam types mimicking cancellous bone are available in different densities, ranging from 80 kg/m3 to 800 kg/m3, giving them different compression, tension, and shear strengths. The (mostly) closed cell cancellous bone phantoms are made out of PU foam which gives the blocks transverse isotropic characteristics. This means that the material properties in-plane vary along different layers of the foam, but the material properties out

Figure 2.1: Sawbones model block of cancellous bone made out of cellular PU foam with a density of 160 kg/m3. The price of such a block is US$46 [10]

of plane are equal everywhere in the block. The open cell cancellous bone blocks that are suitable for cement augmentation and dynamic loading are made out of urethane, epoxies and structural fillers. The production process of these open cell phantoms increases the cost of these material blocks. The price of the phantom blocks is dependent on the size and type of foam. The PU foam block prices range between US$9 and US$65 and open cell block prices range between US$50 and US$125. An example of a cancellous bone material block made out of cellular PU foam with a density of 160 kg/m3 is depicted in Figure 2.1.

On top of providing bone phantom blocks, Sawbones also offers whole vertebrae or spine composite bone phantoms. These phantoms have a short fiber filled epoxy outer layer mimicking the cortical bone, and a solid foam polyurethane core with various densities mimicking the cancellous bone. Sawbones have researched the average strength of real cortical and cancellous bone to determine the most suitable material for composite bones. The material data sheet that Sawbones provides, states that solid rigid PU foam with a density of 17 PCF (270 kg/m3) is the standard foam used for cancellous bone in composite models. This foam has a compression strength and E-Modulus of 6.2 MPa and 155 MPa respectively, and a tension strength and E-Modulus of 4.6 MPa and 205 MPa respectively. Furthermore, the standard foam used for cancellous bone in phantoms mimicking osteoporosis, is the 10 PCF (160 kg/m3) solid rigid PU foam. This foam has a compression strength and Modulus of 2.2 MPa and 58 MPa respectively, and a tension strength and Modulus of 2.1 MPa and 86 MPa respectively. These single vertebra phantoms that mimic human vertebra mechanical characteristics have an approximate price of US$136. One example of a study using Sawbones bone phantoms is the study conducted by Sternheim et al. [98]. A pelvic tumor Sawbones phantom was used made out of solid rigid PU closed cell foam. Another study by Tasinkevych et al. [99] used a cellular rigid PU foam core with a short fiber filled epoxy to simulate the cancellous bone and cortical shell respectively. This phantom was used for acoustic measurements.

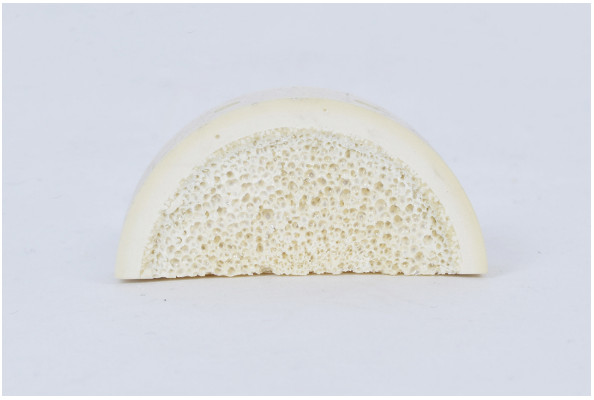

Figure 2.2: Generic bone model slice with a cortical outer layer of 3 mm and a cancellous core. The diameter of the bone model is 40 mm. The price is approximately US$6. [11]

Another company offering similar structural bone phantoms is *Synbone*. This company provides base materials mimicking hard cortical bone, light cortical bone, cancellous bone, and composite bone. The phantom material blocks are all made out of one type of PU foam (not specified which type). Various densities of cancellous foam are available, with corresponding compressive and flexural strengths. It is possible to order foam blocks consisting of two layers with different densities. The price of the material blocks depends on the dimensions, the density of the foam, and the number of layers and ranges between US$9 and US$25. It is mentioned on the website that the phantoms are not as strong as real human bone because of the complex composition of real bone, but closely simulate bone material composition.

Furthermore, they offer generic bone models or whole vertebra phantoms, made out of various materials. An example of a generic bone model slice can be seen in Figure 2.2. The vertebra phantoms are made out of solid rigid foam or composite material. The composite vertebra phantoms consist of a solid foam outer layer with an open cell foam core, which can be soaked with acrylic. Such a vertebra phantom has a price of approximately US$37. A more advanced vertebra phantom they offer is a phantom made out of 'LSS material with cancellous bone density'. This material resembles human bone because it has a harder outer shell and a porous core. The price of such a vertebra phantom depends on the dimensions of the vertebra and ranges from US$39 to US$50.

2.2.2 Additive manufacturing

A totally different approach can be taken by manufacturing the structure of vertebrae by use of additive manufacturing (3D printing). Although not many 3D printed phantoms have been reported yet, the rise of interest in 3D printed medical parts, tools and replicas is high [12,81]. 3D printing provides several great advantages over traditional manufacturing methods. First of all, one can exactly control what the microstructure of the part will be. This decreases variability between parts, resulting in even more standardized phantoms [12]. Furthermore, 3D printing offers the possibility for personalized bone phantoms. By adjusting the trabecular bone architecture in the 3D printing file, different bone types can be manufactured easily such as osteoporotic vertebral bone, healthy vertebral bone, or femur bone [12, 81]. One can

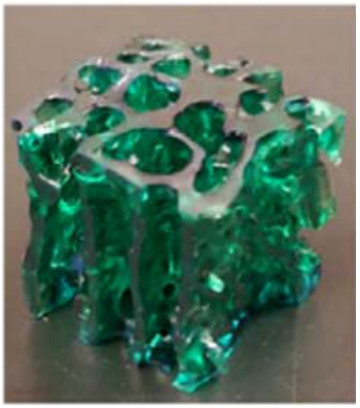

Figure 2.3: Micro-CT based 3D printed cancellous bone of a chimpanzee's metacarpal head (adapted from [12])

even take it a step further by printing an exact replica of a patient's bone by converting a micro-CT scan to a 3D printed part. Thanks to the micro-CT, even the smallest trabecular structures can be imaged and 3D printed. This gives rise to personalized training for preventative treatment [12].

One example of a study on personalized bone is the research conducted by Barak and Black [12]. A micro-CT scan was made of the internal structure of a chimpanzee's third metacarpal head, which was reconstructed to a 3D volume. After segmentation and reconstruction, the model was 3D printed using the Stereolithography (SLA) ProJet 1200 printer and VisiJet FTX Green printing resin. A picture of the resulting phantom can be seen in Figure 2.3. Apart from the original micro-CT scanned bone, they also reconstructed an adjusted model by thinning of the trabeculae in order to test what the effect was on the strength of the material. The original model resulted in a bone volume fraction of approximately 40% and the thinned model had a bone volume fraction of 32%.

A more simplified approach was taken by Burkhard, Furhnstahl and Farshad [81], as they mimicked the cancellous bone as the generalized 3D structure of a gyroid inside a solid cortical shell (all 3D printed). The cortical shell was made out of a 75-25% mixture of hard rigid material (VisiJet CR-CL 200, 3D Systems, Rock Hill, SC, USA) and soft elastomeric material (VisiJet CE-BK, 3D Systems, Rock Hill, SC, USA) respectively. The cancellous structure was made out of 100% of the same hard rigid material. The structure was printed with an inkjet printer. The shape of the 3D gyroid structure can be seen in Figure 2.4. Several models with varying gyroid parameters and cortical thickness parameters were produced and tested for haptic fidelity by four trained spinal surgeons on several spinal surgery steps. A summary of the parameters can be found in Table 2.1. On top of that, a Sawbones vertebra model made out of PU foam with distinct cortical and cancellous materials was tested as well. All vertebra models were categorized by surgeons into: categories 1 & 2 (too soft), categories 3 & 4 (osteoporotic), categories 5 & 6 (normal), categories 7 & 8 (hard) and categories 9 & 10 (too hard). The sawbones model and the gyroid model α were overall categorized as osteoporotic, the 3D printed model β as too soft, the 3D printed models $\gamma 1$ and $\gamma 2$ as normal, and the 3D printed model $\gamma 3$ as hard.

Figure 2.4: Gyroid 3D structure [13]

Table 2.1: Vertebra model cortical thickness and gyroid matrix parameters. GCT = general cortical thickness, LPCT = lateral pedicle cortical thickness, MPCT = medial pedicle cortical thickness, TT = trabecular thickness

Vertebra	GCT (MM)	LPCT (mm)	MPCT (mm)	TT (mm)
α	1.3	0.6	0.8	0.2
β	1.1	0.3	0.4	0.15
$\gamma 1$	1.7	1.2	1.6	0.3
$\gamma 2$	2.6	1.8	2.4	0.4
$\gamma 3$	3.4	2.4	3.2	0.5

A different approach was taken by Bohl et al. [100], as they 3D printed the cortical shell of vertebral models from solid material with a certain thickness, and filled the rest of the models in with several infill patterns, infill percentages and printing orientations. The models were printed with a Fused Deposition Modeling (FDM) printer in three different materials, namely Acrylonitrile Butadiene Styrene (ABS), polyactic acid (PLA) and nylon. They tested the models on screw insertional torque (IT), axial pullout (APO) force and model stiffness (ST). When performing the tests, surgeons decided that, out of all three materials, the models made out of ABS were most similar to human vertebral bone. When comparing test results to historical data, the ABS models with an infill of 25% were most similar to cadaverous vertebral bodies in IT and APO, but were 1.6 times higher in ST.

Up till now, no phantom was reported that mimics both the optical and structural material characteristics of (vertebral) bone. As stated before, such a highly specific phantom that is compatible with the DRS device and the fitting algorithm, and on top of that facilitates similar drilling characteristics to real bone, is required for testing the novel guided steerable drill device currently being developed for improved PSF.

Chapter 3

Problem analysis

3.1 Research goal

The goal of this research is designing, developing and validating a bone phantom that simulates an average human vertebra in terms of mechanical, as well as optical material properties. In this manner, the phantom can be used for steerable drill testing, while simultaneously employing the DRS guiding feedback system. The main reason for developing such a phantom is the ever increasing amount of spinal surgeries and the thereby increasing demand for more accurate and reliable spinal surgery devices. Overcoming the drawbacks of testing on mechanically and optically different vertebrae such as (excised) animal vertebra, would result in more reliable test outcomes, as well as a less costly and more convenient test setup.

The design of a tissue phantom can be very elaborate, closely mimicking most real tissue properties. Designing a phantom with such a high degree of similarity would be defined as a high physical fidelity simulator. Developing a high physical fidelity simulator is usually very time consuming and costly. Given the timeline of this project, the design requirements are prioritized such that the design of the bone phantom does not reflect high physical fidelity, but it only reflects the most important features for reaching the goal. In the current case, the most important features would result in a similar drilling environment and similar fitting component outcomes, comparable to *in vivo* human spinal surgery measurements.

3.2 Functional requirements

Before starting on concept generation of possible phantom designs, a list was made of all functional requirements the phantom must meet. These functional requirements were established by evaluating the steerable drilling process, the DRS measurement system, and the tissue differentiation algorithm. Furthermore, a market analysis was performed, which was discussed in Chapter 2. The functional requirements were subdivided into three categories: general requirements, optical requirement, and structural requirements. The choice was made

to evaluate the structural material characteristics by means of the drill characteristics and the material stiffness and strength. The resulting functional requirements are listed below.

- General functional requirements
  - Size
  - Shape
  - Cost
  - Manufacturability
  - Heat resistance
- Optical functional requirements
  - Absorption spectrum
  - Optical gradient
  - Optical stability and preservability
- Structural functional requirements
  - Material drill characteristics
  - Material stiffness
  - Material strength
  - Microstructure
  - Structural gradient

As explained in Section 1.1.2, bone characteristics can vary greatly between patients. Often, especially cancellous bone is affected by osteoporosis resulting from disease or age. However, the probability of need for spine stabilizing surgery increases with osteoporosis. For this reason, spinal surgeries are frequently carried out on patients with decreased bone strength. It would therefore be beneficial to have different types of phantoms with varying material strengths to test devices on or to practise on. This design flexibility is not a functional requirement of this project but will be kept in mind throughout the design phase. The goal would then be to develop a phantom of which the cancellous microstructure can be adjusted to specific needs. As a result, both healthy and osteoporotic bone phantoms can be manufactured easily.

3.3 Requirement quantification

To check if the functional requirements are met, a method for validation has to be determined. This is done by determining a target and a measurement setup. For every functional requirement mentioned above, the rationale, validation method, and target are given in Tables 3.1, 3.2, and 3.3. A substantiation of the targets is given in this section.

3.3.1 General requirements

The phantom must be convenient to handle, clamp, and test, such that the outer dimensions of the phantom must not be too big nor too small. For this reason, the design choice was made to aim for a phantom with outer dimensions of approximately 100x100x100 mm.

Because the phantom will be used to test novel guided steerable drills on, the size and shape of the phantom should be adjusted to that need. For perceptual fidelity reasons, it is not required to exactly simulate the complex and organic shape of vertebrae, but only the specific features that are required for testing. Following this approach, the complexity of the phantom design is kept at a low level, while still all desired tests can be carried out resulting in reliable data. Because the novel device must drill along a trajectory following the outer cortical shell of the vertebral body, the interface of the cancellous and cortical bone phantom material must be curved with a radius simulating the vertebral body radius. The average diameter of vertebral bodies in the ML and AP directions were stated in Chapter 1 and were determined to vary between 26.3 mm and 43.6 mm (ML direction) and between 19.5 mm and 33.1 mm (AP direction) [17, 18]. For this reason, the radius of the phantom in the ML direction should be approximately 17.5 mm, and the radius in the anterior-posterior direction should be approximately 13.2 mm.

The price of the bone phantom must be viable. Commercially available open cell cancellous bone phantoms made out of urethane, epoxy and structural filler with an approximate outer dimension of 100x100x100 mm are available for a price ranging from US$50 to US$125 [10,11]. Off the shelf stable optical phantoms made out of PU are available and range in price from US$1300 to US$2000 [97]. Less stable, non-preservable hydrogel-based optical phantoms with a 100x100x100 mm dimension can already be manufactured in-house for approximately US$4.30. This means that one should balance between the price and the stability, preservability, and accuracy of the optical phantom. To conclude, the cost of the combined optical and structural phantom must be (well) below US$2125 to be viable, which is €1878 when you convert it to euros.

One of the research goals is to design a phantom or phantom recipe that is manufacturable with basic lab instruments and machines. Manufacturability is a very broad concept that is, among other things, dependent on available resources, machines, and knowledge, and because of this, no straightforward method exists to assess the manufacturability of a part. Despite this, manufacturability is an important requirement for making design decisions concerning the current application because the phantom should be produced and used easily and repeatedly. For this reason, no target can be set for concept selection and validation of manufacturability, but the concepts should be assessed subjectively.

The bone phantom must be able to resist increased temperatures due to drilling maneuvers. Since bone necrosis happens when living bone is subjected to temperatures above 47°C for longer than 1 minute or 55°C for longer than 30 seconds, the phantom must have a melting temperature of least 47°C.

Requirement	Rationale	Validation method	Target
1.1 Size	The phantom must be convenient to clamp onto a test setup. The size of the phantom can be expressed in terms of outer dimensions.	The outer dimensions of the phantom can be measured with a caliper.	100x100x100 mm
1.2 Shape	The shape of the phantom should be such that one is able to obtain accurate results during testing of a steerable drill device following a curved cortical shell trajectory. For this reason, the shape of the phantom should be curved in a similar manner as the outer shell of human vertebrae. The radius of the curve is a good measure for comparing the phantom to real vertebra.	The radius of the curve can be measured with a caliper.	17.5 mm
1.3 Cost	The price of the phantom must be viable. For this reason, the manufacturability cost should be approximately the same or lower than similar available products.	The manufacturing cost of a phantom can be calculated by dividing the total expenses through the total of manufactured phantoms. The total expenses can be calculated by adding the raw material cost, machining cost, and tooling cost.	< €1878
1.4 Manufacturability	The phantom must be manufacturable in a basic lab employed with equipment such as a mixing station and a 3D printer. No highly complex or expensive equipment should be necessary to manufacture the phantom.	No effective scale exists to measure the level of manufacturability. For this reason, the manufacturability of the possible designs will be assessed subjectively.	-
1.5 Heat resistance	The phantom must be able to resist the heat generated during drilling. A good measure for heat resistance is the melting temperature of the phantom.	To validate the heat resistance of the phantom, it can be heated up till the desired temperature and inspected visually.	47 °C

Table 3.1: General functional requirements of the bone phantom

3.3.2 Optical requirements

As we know by now, diffuse reflectance signals can be used to distinguish tissue types. The raw spectra can be compared relatively to distinguish between tissue types but the constructed absorption and scattering spectra can be used too, as well as the fitted tissue content estimation values (discussed in Section 1.4.3). Since the design objective is to develop a phantom that is compatible with the guided steerable surgical drill currently being developed, for which a DRS-based fitting algorithm was developed, the output parameters of this fitting algorithm were used as a design target.

The phantom does not have to consist of exactly the same components as real bone, as long as its characteristics mimic the most relevant optical properties, such that the tissue classification algorithm is able to identify relevant tissue components correctly. In this case, although bone types can be differentiated using many aspects of the spectrum such as deoxyhemoglobin (Hb) and oxyhemoglobin (HbO2), a TU Delft research group has proven that differentiation solely on the fat fraction (FF) could be enough [8, 14, 28, 70]. The measured FF (PDFF and DRFF) in cancellous bone varies between 15-70% and as the cortical bone is approached, the FF drops to 0% respectively, as depicted in Figure 3.1. The aim of the phantom design is mimicking the fitting algorithm output values for cancellous bone tissue, cortical bone tissue, and the pre-cortical transition zone (between the cancellous and cortical bone bone, 3 mm from the cortical boundary).

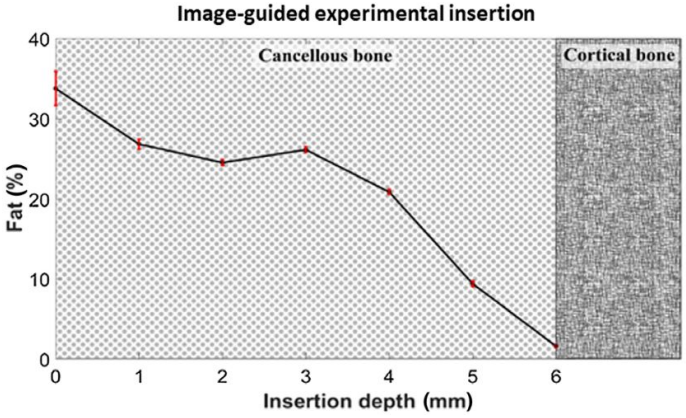

Figure 3.1: Example of estimated FF data in cancellous and cortical bone, obtained from human cadaverous vertebrae [14].

Because there exists a transition region between cortical bone and cancellous bone of approximately 3 mm thick which is called the pre-cortical zone, the optical properties of the phantom in this region should have a gradient too. The optical gradient in the pre-cortical zone is a very important bone characteristic because it is used as a warning sign when the cortical bone is in close proximity to the probe tip. The gradient should be clearly visible in the DRS measurements to avoid cortical breach. The gradient should be linear, increasing from 0% FF in the outer layer (cortical shell) to 50% FF after 3 mm (cancellous bone).

One of the design pillars of this project is delivering a phantom that has excellent optical stability and preservability. This means that the optical (and structural) properties of the

phantom do not change over time, such that the phantom can be stored before usage. Most readily available optical phantoms are made out of hydrogels and have limited preservability because of evaporation and deterioration (discussed in Chapter 2). They generally have a shelf life ranging from hours to days. Fully inorganic phantoms like those from INO [97] have a shelf life of over 10 years. To find a good compromise between phantom complexity and shelf life, the choice was made to opt for a shelf life of at least 8 weeks.

Requirement	Rationale	Validation method	Target
2.1 Absorption characteristics cortical bone	The cortical bone part of the phantom must mimic the absorption characteristics of cortical bone tissue in order to identify the tissue type correctly and guide the drill.	The chosen measures to evaluate the optical characteristics of the phantom are the fitting algorithm output parameters, in specific the estimated FF. The FF can be obtained by measuring the DRS signal and applying the fitting algorithm to the raw spectra.	0% FF
2.2 Absorption characteristics cancellous bone	The cancellous bone part of the phantom must mimic the absorption characteristics of cancellous bone tissue in order to identify the tissue type correctly and guide the drill.	The chosen measures to evaluate the optical characteristics of the phantom are the fitting algorithm output parameters, in specific the FF. The FF can be obtained by measuring the DRS signal and applying the fitting algorithm to the raw spectra.	50% FF
2.3 Optical gradient	The phantom must have an optical gradient incorporated in the pre-cortical zone. In this manner, the guiding system can provide a warning when the drill approaches the cortical shell.	A measure for the gradient is the gradual change in reflectance spectrum as a function of depth of insertion.	Series of relative reflectance spectra ($R(\lambda)$) measured in the pre-cortical zone, gradually changing shape from the cancellous bone towards cortical bone phantom reflectance.
2.4 Optical stability and preservability	The phantom must be reasonable stable such that it can be preserved for several weeks before usage which makes testing more convenient. Results will be more reliable if the optical characteristics do not change over time.	The optical stability of a phantom can be validated by inspecting the phantoms visually and comparing the reflectance spectra at several time intervals.	8 weeks

Table 3.2: Optical functional requirements of the bone phantom

3.3.3 Structural requirements

The hole that is required for enhanced screw fixation with a guided steerable drill will be located along the boundary of cortical and cancellous bone. Ideally, the material characteristics of cancellous, as well as cortical bone would be mimicked. The most important application of the guided steerable drill is to prevent cortical breach but still increase fixation strength compared to screw fixation in mainly cancellous vertebral bone. For this reason, the choice was made to prioritize mimicking the material characteristics of cancellous bone over those of cortical bone, thereby maintaining a low level of design and production complexity.

The focus of the phantom design will be on developing a phantom with normal (healthy) bone characteristics, but considering additional benefit of developing an osteoporotic bone phantom, it is useful to include bone material characteristics of osteoporotic bone in the structural requirement targets as well. Cortical bone is not affected as much by osteoporosis as cancellous bone is. For this reason, the structural targets of osteoporotic cancellous bone concerning the drill force, E-Modulus, strength, microstructure, and structural gradient are stated between brackets after the healthy cancellous bone targets. The cortical bone target is the same for healthy and osteoporotic bone.

Since the main structural bone manipulation procedure in PSF is hole drilling, the structural requirement that is most important is the drill force (Requirement 3.1). As mentioned in Section 1.3, various studies have measured the axial force on a drill operating at a predefined rotation speed, feed rate, and drill diameter. The best validation method would be to compare the axial drill force in the phantom to the axial drill force in a human vertebral bone. However, such data on human vertebrae was not found during the literature search. Data that was available, was obtained on animal vertebrae with a setup consisting of high predefined rotation speed drills (>3300 rpm). The setup that is available for the current research has a rotation speed limit of 1800 rpm and since the axial force is strongly affected by the rotation speed of the drill, this data can not be used to validate the phantom design. Lastly, a previous research in the this research group by Kan [34] measured the axial drill force on a Sawbones cancellous bone phantom made out of rigid cellular PU foam combined with a short fiber filled epoxy cortical layer, with a low rotation speed of 500 rpm. Since this rotation speed is under the speed limit, the data can be used to compare the current phantom design to. With a 2.7 mm diameter drill bit, a rotation speed of 500 rpm and a feed rate of 1 mm/s, the force in the Sawbones cancellous bone phantom fluctuated between 0.0-10.0 N with a mean around 6.0 N. Therefore, the target drill force of healthy cancellous bone will be between 0.0-10.0 N with a mean around 6 N.

Ong and Bouazza-Marouf [101] have investigated the correlation between Bone Mineral Density (BMD) and drill force in cancellous bone. They concluded that there is a strong relation between the BMD and the drill force in cancellous bone with a constant rotation speed and feed rate. Furthermore, the correlation between BMD (ash density) and apparent density has been reported previously to be 0.598 by Schileo et al. [33]. Taking this into account, drill force can be correlated to BVF. As mentioned before, the variability of bone strength is very large due to multiple patient-specific factors. However, for simplicity reasons, it is assumed that the BVF of healthy cancellous bone is approximately 25% (which gives it an apparent density of 450 kg/m3 and a BMD of 269 kg/m3), and that of osteoporotic bone is 10% (which gives it an apparent density of 180 kg/m3 and a BMD of 108 kg/m3). When looking at the results

of Ong [56], it can be concluded that the axial drill force decreased from from approximately 10 N at a BMD of 215 kg/m3 to 2 N at a BMD of 108 kg/m3. This means that the axial drill force decreased with a factor of 5. Therefore, the targets for osteoporotic cancellous bone are estimated to be a factor of 5 lower as well, resulting in a cancellous drill force fluctuating between 0.0-2.0 N, with a mean around 1.2 N. The microstructure of osteoporotic bone is known to be more porous than the microstructure of healthy bone [31]. For this reason, the microstructure and the gradient of osteoporotic bone phantom should be larger than those of a healthy bone phantom.

According to Duperron et al. [54], the peak drill force in cortical bone (F_p) increases with a factor of 5 compared to cancellous bone. Since the aim is to maintain a low level of design and production complexity, the phantom will not be optimized for cortical material characteristics, but the choice was made to set the drill force target in cortical bone to at least 3 times that of cancellous bone, which results in a peak drill force of at least 30.0 N for healthy bone (F_{ph}). Because cortical bone is not significantly affected by osteoporosis, the cortical peak force value of osteoporotic bone is equal to the value of healthy bone (F_{po}).

For cancellous bone, measured stiffness and strength values have an extremely large variability between studies. This is most probably due to the large inter-patient variance and the difference in employed methods. When looking at the three most relevant studies, conducted on human vertebral bone, Mosekilde et al. [31], Nicholson et al. [29], and Moran and Keaveny [32] have measured the E-Modulus of cancellous bone. Mosekilde et al. [31] reported an E-Modulus between 40-70 MPa for human vertebral cancellous bone of healthy individuals around the age of 20 in the ML/AP direction, with a BVF varying between 16.3 and 20.4%. However, Nicholson reported a similar average E-Modulus of human vertebral cancellous bone in the ML/AP direction of 47.3 MPa, with a very low average sample BVF of 7.6% (which can be categorized as osteoporotic). When comparing the values obtained by Mosekilde to the remaining reported E-Modulus values in Table 1.1 (the ML/AP direction as well as SI direction), it was concluded that the values reported by Mosekilde were significantly lower compared to the majority of the values, when taking into account the corresponding BVF of the samples. For this reason, only the studies by Morgan and Keaveny [32] and Nicholson et al. [29], were taken as a reference, and the study by Mosekilde et al. [31] was excluded.

Because of the low average BVF of the samples of the study by Nicholson, it was assumed that the resulted E-Modulus of this study was representable for osteoporotic bone. The average of the values in the ML and AP direction was used, which results in desired osteoporotic cancellous E-Modulus of 47.3 MPa. Because the values obtained by Mosekilde were excluded from the references unfortunately, no reliable data was found on the E-Modulus of healthy cancellous bone in the ML/AP direction. However, the measured value of the E-Modulus in the SI direction is a factor of 2.1 higher in the study conducted by Morgan and Keaveny (with a slightly higher BVF of 10%, thus more representable for healthy bone) compared to that of Nicholson. For this reason, the assumption was made that the E-Modulus of the cancellous bone in the ML/AP direction for healthy bone is also a factor of 2.1 higher than that of osteoporotic bone in the ML/AP direction, which results in an approximate E-Modulus of 99.3 MPa for healthy cancellous bone phantom material.

There was no data provided for the yield strength of the samples in the ML/AP direction of the study by Morgan and Keaveny. However, because it was already shown that the strength

of vertebral cancellous bone is much higher in the SI direction than in the ML or AP direction, it can be assumed that the desired material strength of cancellous bone in a healthy bone phantom is smaller than the value measured by Morgan and Keaveny in the SI direction, which is 2.0 MPa [32]. There was no data provided by Nicholson et al. on the yield strength of osteoporotic bone samples either. For this reason the yield strength of osteoporotic bone phantom material is assumed to be less than 2.0 MPa as well, and lower than the yield strength of healthy cancellous bone.

Since the vertical trabeculae are approximately 0.2 mm in width and the BVF of cancellous bone varies between 8% and 50%, the trabecular spacing should range between 0.4 and 2.5 mm. Mimicking the exact trabecular spacing is less important than mimicking the material drill characteristics, stiffness and strength because a porous material will already be useful to simulate bone drilling and anchoring. For this reason, the microstructure should be within the stated range, but the definitive value will depend on the desired material stiffness and strength characteristics.

There should be a structural gradient in the phantom because having a structural gradient automatically ensures an optical gradient. The structural gradient is dependent on the production method and material type of the cancellous bone material and thus a target cannot be specified in the early design stage. What can be specified is that the pores of the microstructure should decrease in the pre-cortical zone from the cancellous bone phantom towards the cortical bone phantom, resulting in solid phantom material at the cortical shell of the phantom. Also, there should be a visual axial drill force, stiffness and strength increase in the pre-cortical zone.

Requirement	Rationale	Validation method	Target
3.1 Drill force cancellous bone	The cancellous part of the phantom must provide a similar drilling environment as real cancellous bone because drilling is the main action in PSF.	The axial force that is exerted on a drill which operates with a predefined rotation speed and feed rate is a good measure for comparing drilling environments. This force can be measured with force sensor.	0.0-10.0 N/ mean 6.0 N (0.0-2.0 N/ mean 1.2 N)
3.2 Drill force cortical bone	The cortical part of the phantom phantom must provide a similar drilling environment as real cortical.	The axial force that is exerted on a drill which operates with a predefined rotation speed and feed rate is a good measure for comparing drilling environments. This force can be measured with force sensor.	>30.0 N
3.3 Stiffness cancellous bone	The phantom must mimic the material stiffness of the cancellous core of the vertebra in the ML and/or AP direction to increase phantom handling similarity.	A compression test can be carried out and from the stress-strain curve, the E-modulus of the cancellous bone material can be approximated.	94.5 MPa (47.3 MPa)
3.4 Strength cancellous bone	The phantom must mimic the material strength of the cancellous core of the vertebra in the ML and/or AP direction to increase phantom handling similarity.	A compression test can be carried out and from the stress-strain curve, the yield strength (σ_y) of the cancellous bone material can be approximated.	<2.0 MPa (<2.0 MPa)
3.5 Microstructure (MS)	The porous structure of the cancellous core of vertebra influence screw insertion and fixation heavily. Therefore, the pores in the phantom must have approximately the same pore size as cancellous bone.	The pore size can be measured with a caliper.	0.4-2.5 mm (> healthy MS)
3.6 Structural gradient	The phantom must have a structural gradient incorporated in the pre-cortical zone. In this manner, the pedicle screw can be fixated near the strong cortical shell in stead of in the less strong cancellous bone.	The BVF distribution can be validated by measuring the density of different layers within the phantom.	Linearly increasing, value t.b.d

Table 3.3: Structural functional requirements of the bone phantom

Part II

Second part: Conceptual design

Chapter 4

Concept generation and selection

Based on the functional requirements stated in Chapter 3, a brainstorm was conducted. Thanks to this brainstorm session, several new phantom concepts were generated. After that, the concepts were evaluated, based on the functional requirements. After evaluation, the most promising concept was selected.

4.1 Concept generation

In order to not overlook any promising options, a structured design approach was taken. This approach consisted of organizing the concepts in a design tree. By walking down the branches of the tree, different design options can be generated. The design tree is given in Figure 4.1.

In the tree, just as in the rest of the report, two separate regions of design can be identified: the structural phantom part and the optical phantom part (separated by the vertical dotted line). At the top of the tree, a structural phantom design is chosen, after which the optical phantom design follows. Since cancellous bone has a complex, organic structure composed out of cavities, a logical option would be to mimic this microstructure. However, this complex structure significantly limits the material and production method possibilities. For these reasons, the structural design has three main design options of which two contain a microstructure and one is a solid without mimicking the cancellous bone microstructure. The tree design options are: a 3D printed microstructure, a PU foam microstructure, or no microstructural matrix but a solid rigid block.

When looking at the microstructural options, the choice can be made between closed cell or open cell microstructure. The open cell microstructure is porous and can therefore be augmented with an optical filler. The cavities of the closed cell microstructure can not be filled and for that reason, no optical phantom filler can be used to enhance the phantom. Because of that, these option do not carry on to the optical filler design. If the choice is made to use the open cell microstructure or no microstructural matrix, the design decision tree carries on to the optical filler and the cavities or structural material can be enhanced with optical

properties.

The optical filler is subdivided into three main categories: inorganic filler, organic filler, or hybrid filler. The inorganic filler is made out of a polymer base material and added to that base material are inorganic scattering and absorption agents. The polymer base materials range in stiffness and are available in hard, flexible, and soft versions. The organic filler is only made out of organic materials which are inherently soft or liquid, and the additives that induce scattering and absorption are mainly based on lipids. The organic filler generally suffers from dehydration and deterioration due to bacterial growth which can be solved by sealing it properly. When considering organic filler, the choice can be made between an organic hydrogel thickening base which gives it a rigid gel-like structure, or no base (water/fat liquid emulsion), which must always be prevented from leaking by a sealant. The hybrid filler consists of a polymer base material that is enhanced with organic scattering and absorption additives, based on lipids. Because the base material is made out of polymer chains, it can be varied from hard to soft.

In principle, the design decision tree can be used to combine design choices in order to generate concepts. However, not all combinations are possible. For example, when considering the mechanical property requirements of vertebral bone, one can conclude that if a structural matrix is chosen, the cavities must not be filled up with a hard filler, but with a soft or flexible filler to mimic bone marrow material properties. On the other hand, when no structural matrix is chosen, the filler must not be made out of soft or flexible material, but bone structural properties should be mimicked by a hard filler. Following this deduction method, four promising and feasible concepts are shown in the design decision tree by colored pathways, and described in the list below. This, however, is not the full spectrum of concepts, since combining all structural options (3D printed matrix, PU matrix, and no matrix) with all optical options (inorganic filler, organic filler without sealing, organic filler with sealing and base, organic filler with sealing without base, and hybrid filler) would result in twelve concepts (excluding soft phantoms without structural matrix).

- Red: The structural part of the phantom consists of a 3D printed structure with a cortical shell and a cancellous cellular core with open cells. The cavities of the cancellous core are filled up with an organic filler with a soft base material made out of gelatin. To prevent dehydration and deterioration, the phantom is sealed. The scattering and absorption spectra are mimicked by mixing the gelatin with a high fat content peanut oil emulsion.
- Blue: The structural part of the phantom consists of a 3D printed structure with a cortical shell and a cancellous cellular core with open cells. The cavities of the cancellous core are filled with a soft hybrid polymer filler made out of silicone. For absorption and scattering spectra, a high fat content peanut oil emulsion is mixed into the silicone.
- Green: The structural part of the phantom consists of a PU foam cancellous core with open cell and a solid PU foam cortical shell. The cavities of the cancellous core are filled up with an organic filler with a soft base material made out of gelatin. To prevent dehydration and deterioration, the phantom is sealed. The scattering and absorption spectra are mimicked by mixing the gelatin with a high fat content peanut oil emulsion.

- Orange: The phantom does not have a microstructure but is a solid block, and the mechanical properties of the phantom are not determined by the matrix, but by the material properties of the optical filler. The filler is made out of the hard inorganic epoxy base material. The scattering additives are yet to be determined and to obtain a tissue mimicking absorption spectrum, a combination of dyes is used with absorption peaks equal to the absorption peaks of water and mammalian fat.

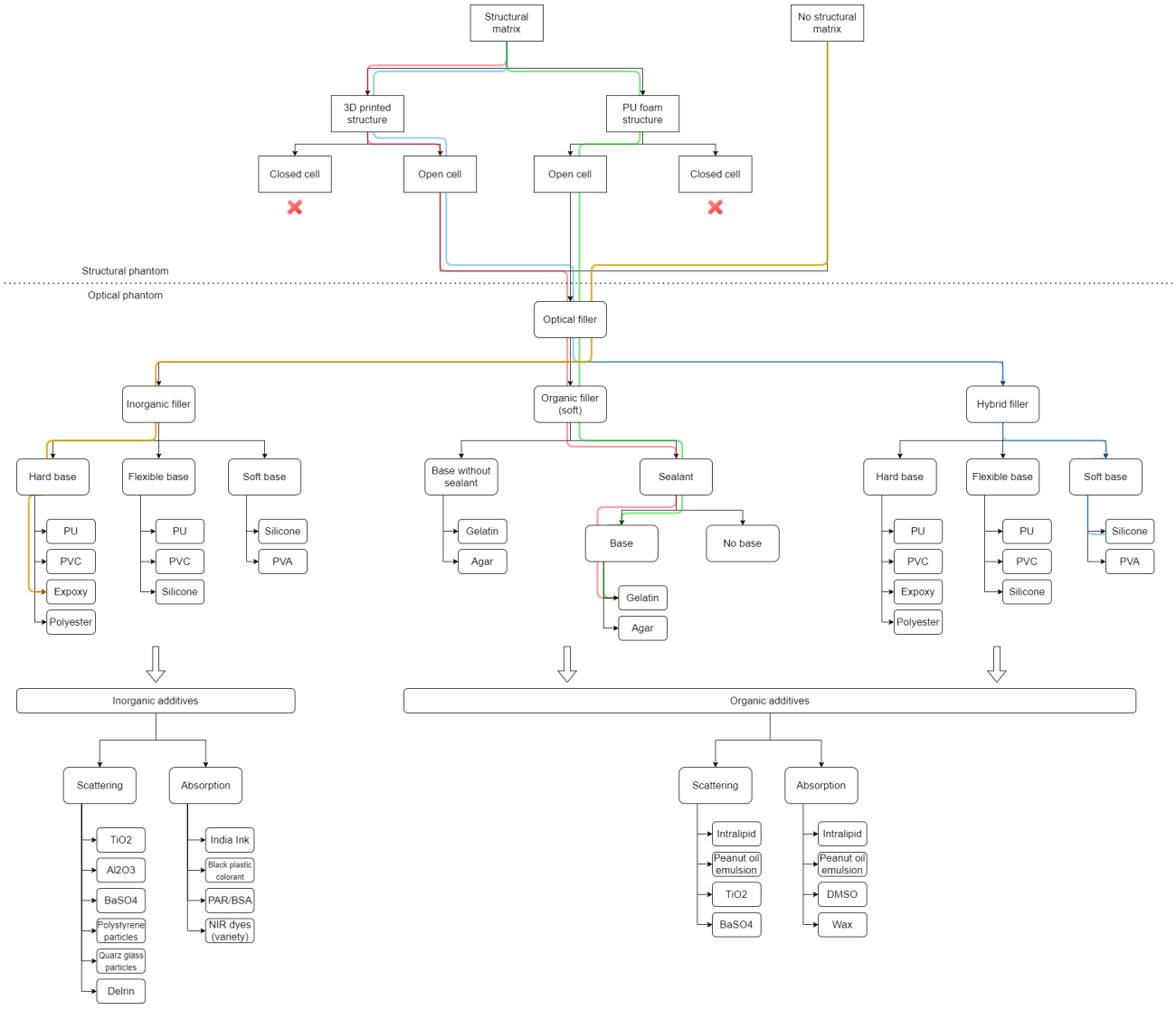

Figure 4.1: Design tree

4.2 Concept selection

When looking at the feasibility of all the design options in the design decision tree, several advantages and limitation can be identified per option. First, these advantages and limitations

will be discussed. After that, all possible concepts will be graded by use of the Pugh's systematic multi-criteria decision making (MCDM) method [102].

4.2.1 Design options

To start with the 3D printed structure design option, the accuracy and reliability of 3D printed parts depend on the type of printing technique and the type of printer. In this study, two different printers were available, namely a Formlabs 3B (Formlabs, Somerville, USA) SLA printer and an Ultimaker 3 (Ultimaker, Utrecht, The Netherlands) FDM printer. The specifications of these printers will be considered throughout the concept generation and selection process. Generally, 3D printing allows for an extremely flexible design. Using 3D printing, the design of the phantom can be adjusted to the research it will be used for. For example, the thickness of trabeculae, the trabecular spacing, the cortical thickness, and the shape of the phantom can be tailored per print. This allows for easy fabrication and testing of osteoporotic bone phantom, healthy bone phantom, strong bone phantom, small curvature shell and large curvature shell. Furthermore, the fabrication process is fully controlled due to which complex, organic shapes can be made, such as a porous cancellous core structure. Another advantage is that 3D printing (both stereolithography (SLA) and fused deposition modeling (FDM)) is a very resource-efficient process. In FDM there is no residue material and in SLA the residue material can be reused for a next print. Unfortunately, all materials compatible with the available printers have much a lower E-Modulus and strength than solid bone material.

When considering a microstructural matrix made out of PU foam, it is difficult to find a strong, open cell PU foam with documented material properties for in-house production. Furthermore, the fabrication process of a PU foam can not be controlled precisely which results in inter-phantom variety, differently sized cavities, and closed cells. Lastly, the E-Modulus and strength of PU foam is generally much lower than that of bone.

Obviously, the main disadvantage of no structural matrix is that the microstructure of cancellous bone cannot be mimicked. This will inevitably induce discrepancies in test results of drilling and anchoring tests between the phantom and the real human bone. However, the fabrication of a solid, rigid block with similar overall material properties to human bone, will be much easier than the fabrication of a porous structural matrix. Such a block can for example be made with casting and machining.

The most straight forward method for mimicking the correct fat fraction is actually using the desired ratio of water and fat in the phantom. The biggest advantage of using a fully organic optical filler with water and fat to mimic the correct fat fraction is that it is commonly used. The optical properties of enhanced hyrdogel organic phantoms are well documented, and a wide variety of organic compounds have been tested in combination with organic base materials [90]. For this reason, the design of such an organic optical filler is relatively straight forward and the test results are predictable. Furthermore, hydrogels such as gelatin and agar are, besides being a gelling agent, also inherent emulsifiers, which means that they allow water to mix well with fat. For this reason, a homogeneous water-fat emulsion can be established. The biggest disadvantage is that the hydrogel organic phantoms are subjected to dehydration

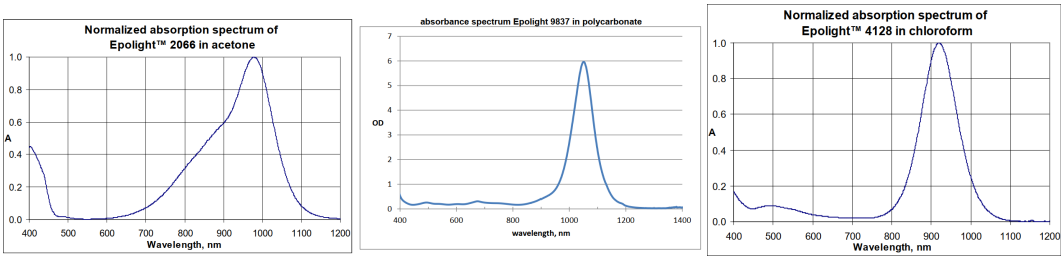

(a) (b) (c)

Figure 4.2: The absorption spectra of different commercially available NIR dyes [15]

and oxidation and therefore, the shelf life is limited. Several reports have mentioned a limited shelf life of refrigerated optical hydrogel-based phantoms ranging from a few hours to a few days [90–92].

Another method is finding synthetic materials that have the same continuous optical properties as water and fat respectively, and combining them in desired ratios, which will result in a fully inorganic optical filler with an absorption spectrum similar to bone tissue. The biggest advantage of an inorganic optical filler is the unlimited shelf life and extremely high stability. However, a major challenge is finding the optimal inorganic additives to mimic the continuous spectra of fat and water over a large range of wavelengths. Very little papers were found on the addition of inorganic NIR absorption agents in a phantom. The difference in number between commercially available VIS absorption agents and NIR absorption agents is large. Common inorganic dyes such as India ink provide a semi-flat absorption spectrum over a large range of wavelengths. For this reason, such dyes can not be used to mimic the highly wavelength-dependent absorption spectrum of fat and water over a range of wavelengths. This complication might be overcome by selecting a more narrow bandwidth for tissue measurement and fitting, in which well documented NIR dyes are effective.

For example, Epolin [15] offers several NIR dyes with distinct absorption peaks. By combining NIR dyes, the absorption spectrum of water and fat may be approximated. The absorption spectra of three types of dyes is shown in Figure 4.2. They can be combined to mimic fat and water absorption spectra. Figure 4.3a shows the shape of the absorption spectrum of a combination of the three dyes, as well as the DRS measured absorption spectra of real water and fat. It can be seen that for a wavelength range of 900-1100 nm, the shape of the real fat/water and inorganic phantom spectra are similar. However, since the fitting algorithm is designed for organic constituent identification based on exact organic standardized absorption spectra over the wavelength range 400-900 nm, 1000-1600 nm, or both, the translation of spectra obtained from inorganic phantoms to organic tissues might result in large fitting errors, due to slight differences in obtained spectra and an incomplete mimicking wavelength range. Furthermore, because NIR dyes are not widely available and complex to fabricate, the prices of these dyes is relatively high, ranging from US$64 to US$300 per gram. Although the absorption of these dyes differs and the exact required amount per phantom must be tested, the dyes are much more expensive than commonly used dyes such as India ink, which has an approximate price of €10 per 100 g.

Although the stable material characteristics of a plastic, in combination with the optical

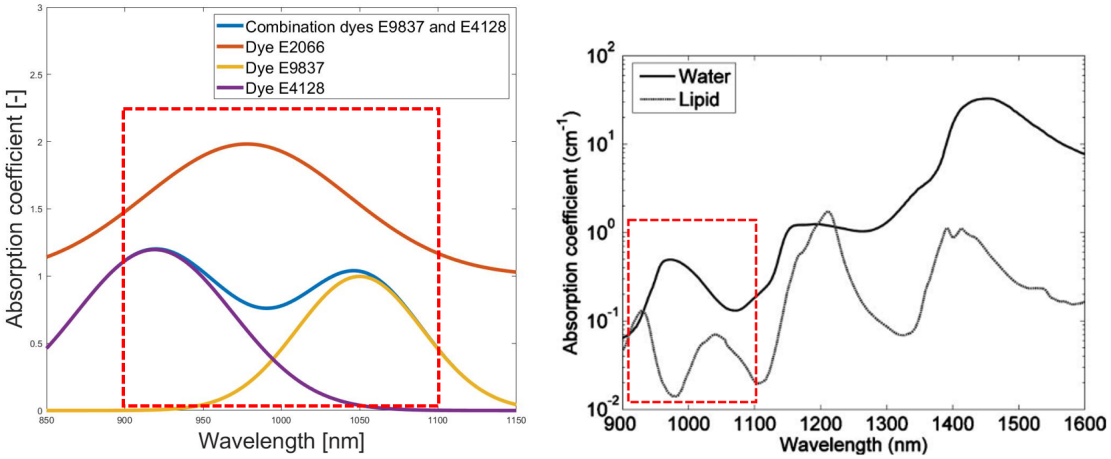

(a) An approximation of the combined absorption of dyes E9637 and E4128, and dye E2066

(b) The absorption spectrum of water and lipid [76]

Figure 4.3: A comparison between the absorption spectra of synthetic dyes and the absorption spectra of water and lipid

characteristics of a water/fat emulsion, which results in a hybrid optical filler seems like an optimal solution for this design problem, recent tests within our research group and within other research groups have not succeeded in mixing the two materials. A hybrid optical filler could be difficult to accomplish because most plastics are hydrophobic or lipophobic or both. For example, epoxies, PVC, PLA, ABS, silicone, polyester and PU are generally hydrophobic. PVA on the other hand is hydrophilic. Contradictory, the paper by Avtzi et al. showed great results when mixing Intralipid (water/fat emulsion) with an epoxy [95], although the Intralipid content (1% of solid by volume) was significantly lower than the content aimed for in the current research. Before a conclusion can be drawn on the feasibility of a hybrid optical filler, the fabrication process must be tested.

4.2.2 Pugh's MCDM

The multi-criteria decision making (MCDM) method developed by Pugh uses the criteria defined in the functional requirements and their weight of importance to rank concepts. The working principle of the Pugh's matrix is shown in Figure 4.4. This figure shows the criteria on the left side. Each criteria receives a weight from 1 to 10, depending on the importance of the criteria (1 is least important, 10 is most important). All possible concepts are listed at the top, which are in this case all options of the design decision tree. After the criteria, weights, and concepts are defined, each concept is rated on a scale value of +2, +1, S, -1 or -2. In order to assign scores to the concepts, a quantitative reference is determined that usually refers to the neutral score *S*. Quantitative values are defined for every other score, based on the deviation from the neutral.

For this project, all possible concepts derived from the design decision tree are numbered and organized in Table 4.1. The concepts discussed previously and marked in the design decision tree are shown in the table with their corresponding colors (concepts 3, 5, 8 and 11). The

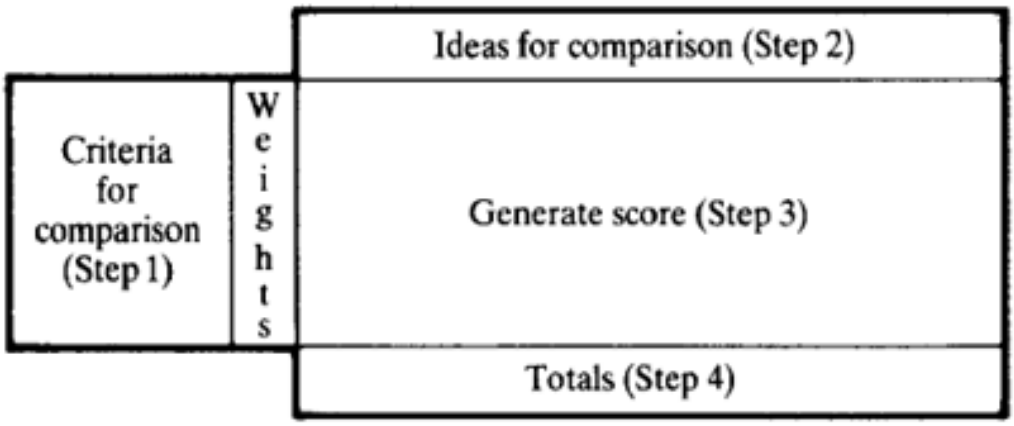

Figure 4.4: Pugh's matrix for concept selection based on multiple criteria and their respective weights

Filler / Structure	Inorganic	Organic with base without sealing	Organic with sealing with base	Organic with sealing without base	Hybrid
3D print	1	2	3	4	5
PU foam	6	7	8	9	10
No matrix	11	X	X	X	12

Table 4.1: Overview of the generated concepts and their numbering

numbers of the concepts correspond to their scores in the final Pugh's matrix outcome (Table 4.3).The reference value of each criteria, as well as the threshold values for deviating from the neutral score, are presented in Table 4.2.

Now that the criteria, weights, concepts, and thresholds have been determined, the full Pugh's matrix can be constructed. The complete matrix with resulting scores is shown in Table 4.3. It should be noted that although there is no assessment target value for the manufacturability of concepts, the concepts still scored differently due to subjective assessment. All concepts with organic filler and an open structural matrix are assumed to be easier to produce than concepts with a hybrid filler since the feasibility of the production and infusion of a hybrid optical filler was never validated before. Furthermore, concepts with a structural matrix made out of PU foam are assumed to be easier to produce than 3D printed matrices because of the need for a reliable and accurate 3D printer.

As can be seen, concept 5 has the highest overall weighted score of 116. Furthermore, the score of concepts 3 lies very close to the score of concept 5, namely 115. To conclude, the

Criterion	Reference	+2	+1	S	-1	-2
1.1	10x10x10 cm	-	-	10x10x10	10x10x10 +/- 5x5x5	-
1.2	17.5 mm	-	-	17.5	17.5 +/- 5.0	-
1.3	€100.0	50.0	75.0	100.0	150.0	>200.0
1.4	-	-	-	-	-	-
1.5	55.0°C	>150.0	100.0	55.0	45.0	<40.0
2.1	Deviation from spectrum (cortical)	0%	+/-5%	+/-10%	+/-20%	+/-30%
2.2	Deviation from spectrum (cancellous)	+/-0%	+/-5%	+/-10%	+/-20%	+/-30%
2.3	Deviation from spectrum (precortical)	+/-0%	+/-5%	+/-10%	+/-20%	+/-20%
2.4	8.0 weeks	>52.0	16.0	8.0	4.0	<1.0
3.1	0.0-10.0 N (mean 6.0 N)	0.0-10.0 (mean 6.0)	0.0-10.0 (mean 6.0) +/-0.6	0.0-10.0 (mean 6.0) +/-1.2	0.0-10.0 (mean 6.0) +/-3.0	0.0-10.0 (mean 6.0) +/-4.5
3.2	30 N	48	40-48	30-40	20-30	<20
3.3	94.5 MPa	94.5	94.5 +/- 9.5	94.5 +/- 18.9	94.5 +/- 47.3	94.5 +/- 70.9
3.4	<2.0 MPa	-	-	<2.0	2.0-3.0	>3.0
3.5	0.4-2.5 mm	0.4-2.5	0.4-2.5 +/-0.5	0.4-2.5 +/-1.0	0.4-2.5 +/-1.5	0.4-2.5 +/-2.0
3.6	Perfect linear relation	Perfect linear relation	step wise, 6 steps	step wise, 3 steps	step wise, 2 steps	no gradient

Table 4.2: Quantitative reference value and threshold values for performing Pugh's ranking

most feasible concept is concept 5, which consists of a 3D printed open cell microstructure with a cortical shell. The cavities of the open cell microstructure are filled with an optical filler consisting of a mixture of plastic, water, and fat. The second most feasible concept has the same 3D printed microstructure but the filler is a fully organic filler consisting of a mixture of water and fat, with hydrogel base, and with proper sealing.

Criterion	Concepts→ Weight ↓	1	2	3	4	5	6	7	8	9	10	11	12
1.1	2	s	s	s	s	s	s	s	s	s	s	s	s
1.2	8	s	s	s	s	s	-1	-1	-1	-1	-1	s	s
1.3	5	-2	+1	+1	+1	+1	-2	+2	+2	+2	+2	-2	+2
1.4	9	s	s	s	s	-1	+1	+1	+1	+1	-1	+1	s
1.5	7	+1	s	s	s	+2	+1	s	s	s	+1	+1	+1
2.1	6	s	s	s	s	s	-2	-2	-2	-2	-2	s	s
2.2	10	-2	+2	+2	+2	+1	-2	+2	+2	+2	+1	-2	+1
2.3	10	+2	+2	+2	+2	+2	-1	-1	-1	-1	-1	-2	-2
2.4	8	+2	-2	s	s	+2	+2	-2	s	s	+1	+2	+1
3.1	10	+2	+2	+2	+1	+1	s	-1	-1	-2	s	+2	+2
3.2	4	-1	-1	-1	-1	-1	-2	-2	-2	-2	-2	+1	+1
3.3	5	+2	+2	+2	+2	+2	s	s	s	s	s	-2	-2
3.4	5	+2	+2	+2	+2	+2	s	s	s	s	s	-2	-2
3.5	8	+2	+2	+2	+2	+2	s	s	s	s	s	-2	-2
3.6	9	+2	+2	+2	+2	+2	-1	-1	-1	-1	-1	-2	-2
	Weighted score	83	99	115	105	116	-45	-34	-18	-28	-21	-48	-15

Table 4.3: Resulting scores per concept of the Pugh's MCDM method

Although the scores of concepts 3 and 5 are very close, the choice was made to proceed with the most innovative and promising concept, namely concept 5 which consists of a 3D printed structural matrix and a hybrid optical filler. Since the hybrid optical filler concept has never been investigated before, its production feasibility remains questionable. Furthermore, the fitting algorithm was not designed for a hybrid tissue phantom which could lead to fitting challenges. Several papers were written on 3D printing bone structures, but the exact production and material characteristics have never been documented for the current manufacturing facilities and application. Lastly, infusing the optical filler in the structural matrix could induce production challenges. All these aspects of the novel concept will have to be tested before proceeding to the detailed design and testing phase. The preliminary tests will be discussed in more detail in the following chapter.

Chapter 5

Preliminary testing

Just like the state of the art, problem analysis and conceptual design, the preliminary tests are subdivided into two parts: optical tests and structural tests. Two optical tests have been carried out, which are a hybrid optical filler feasibility test and a stability test. Next to that, three structural tests have been carried out as well, to asses production methods, material compression characteristics and material drill characteristics. The methods, test setup, results, and conclusions of these five tests will be discussed in this chapter.

5.1 Optical tests

Based on the scores mentioned in Chapter 4, the choice was made to investigate a phantom containing an optical filler made out of a mixture of silicone, water, and fat. The water and fat are integrated in the optical filler because the design target is to mimic the FF of cancellous bone. The silicone is added to this mixture to improve stability and preservability. Previously, problems were encountered with mixing silicone with organic substances. For this reason, the production and optical feasibility of various optical fillers was tested. The effect of the added silicone on the stability and preservability of the optical filler was analyzed as well. This was done using both the raw (normalized) spectra, as well as the fitting output parameters that resulted from the custom made fitting algorithm. The effect of the added silicone to the water/fat mixture was assessed by monitoring optical filler samples over a longer period of time and comparing the raw spectra, as well as the fitting output parameters.

5.1.1 Hybrid optical filler feasibility

In order to evaluate if production of the hybrid optical filler is possible and if the DRS measurement in combination with the fitting algorithm gives desired absorption characteristics, various combinations of hybrid filler contents were manufactured and tested.

Since the FF is the ratio of fat content over water+fat content in a tissue, the absolute amount of water and fat in the phantom should not influence the FF fitting estimation significantly, as

long as the ratio is kept constant. In order to test this hypothesis, optical fillers with various amounts of water+fat were produced and tested. Because silicone is hydrophobic, it would be advantageous to have a low water+fat content in the optical filler, while maintaining the correct FF fitting estimation. The investigated water+fat content of the optical filler samples were 5%, 20% and 50%.

Because the FF reported for cancellous bone has a large variability (it ranges from 30 to 70%), different fat fractions were tested to investigate the effect of the fat fraction on the measurement and fitting results. Three different FFs were manufactured, namely 30%, 40% and 50% FF.

Because the optical filler in the bone phantom represents bone marrow in cancellous bone, the aim is to mimic the material characteristics of the marrow as closely as possible as well. This means that the optical filler should be a very soft, gel-like substance. To investigate the influence of silicone on the optical filler manufacturability and material characteristics, three different silicone types were used. Firstly, very soft and flexible silicone with shore hardness A-5 (Siliconen Additie Kleurloos 5 voor maskers en flexibele mallen, Silicones and More) was used. Next to that, a slightly harder silicone with a shore hardness of A-20 (Elastosil FX 20, Silicones and More) was used. Lastly, a harder silicone with a shore hardness of A-40 and a very short pot life of 2 minutes (Silconen Additie Transparant 40 Snel, Silicones and More) was used as well. As a reference for production, stability, and preservability, three phantoms (30%, 40% and 50% FF) without any silicone were manufactured and tested as well.

Method

Since optical filler samples with three different water+fat contents, three different FFs and three different silicone types were manufactured, together with three pure water+fat samples, the total number of optical filler samples was 30. The pure water/fat samples and the oily emulsions with varying FFs as ingredient for the hybrid samples were manufactured according to the production protocol of Bush et al. [93]. This protocol is designed for making limited preservable pure water/fat phantoms with agar agar as gelling agent and emulsifier. Each of the oily emulsions included demineralized water as the water base, peanut oil as the fat base, agar agar as natural emulsifier and gelling agent (Agar agar gom powder E406, Natural Spices, Mijndrecht, The Netherlands), Tween20/polyethylene glycol sorbitan monolaurate as water-soluble surfactant (P1379, Sigma Aldrich, Amsterdam, The Netherlands), Span80/sorbitan oleate as oil-soluble surfactant (S6760, Sigma Aldrich, Amsterdam, The Netherlands), and sodium benzoate as preservative (Unique Products Schuurman, Nieuwegein, The Netherlands). The Gadolinium-DTPA surfactant was left out because the phantoms are not designed for MR imaging. Although the molecular structure of peanut oil is slightly different than that of human fat, the absorption peaks of several edible oils including peanut oil, and mammalian fat absorption peaks match very well, as validated by several studies [76, 86, 93, 103].

After the oily emulsions were produced, they were heated till liquid and mixed with the appropriate amount of silicone with a blender. After that, the hybrid filler was poured into a mold and left at room temperature for 2 days to fully harden out. After that, they were stored with a plastic wrap in a fridge. The optical filler samples are coded according to the following structure: firstly the silicone type is mentioned, S equals soft silicone, M equals medium silicone, H equals hard silicone. On top of that, pure water/fat phantoms that do

FF \ WFC	5%	20%	50%	100%
30%	S30-5, M30-5, H30-5	S30-20, M30-20, H30-20	S30-50, M30-50, H30-50	P30
40%	S40-5, M40-5, H40-5	S40-20, M40-20, H40-20	S40-50, M40-50, H40-50	P40
50%	S50-5, M50-5, H50-5	S50-20, M50-20, H50-20	S50-50, M50-50, H50-50	P50

Table 5.1: Summary of the code names of the samples of the preliminary optical tests. FF = fat fraction, WFC = water+fat content.

not contain any silicone are coded with P. Secondly the FF is mentioned (30%, 40% or 50%), and lastly, the water+fat content is mentioned (5%, 20%, 50%, or a blank for the pure water/fat phantoms). A summary of the code names of all the samples is given in Table 5.1.

The DRS measurement setup consists of a probe containing one excitation fiber and one collection fiber, each with a diameter of 200 μm. The fibers are placed inside the probe with a center-to-center distance of 1.22 mm. The excitation fiber is connected to a tungsten halogen broadband light source (Avantes, Apeldoorn, The Netherlands). The collecting fiber is connected to two spectrometers, one measuring the VIS reflectance spectrum from 400-1600 nm (Mayapro2000, Ocean Optics, Dunedin, USA) and one measuring the NIR reflectance spectrum from 1000-1600 nm (NIRQuest 512, Ocean Optics, Dunedin, USA). The data acquired by the spectrometers is processed with the FlexPn measurement software program (Labview, National Instruments, Austin, USA). Because of the dominant absorption characteristics of fat in the NIR range (1000-1600 nm), only this spectral range will be analyzed and discussed in the remainder of this report. The integration time for the NIR spectrum was set to 500 ms. The output of the DRS console is a .txt file that contains the reflectance intensity at a corresponding wavelength for 255 distinct wavelengths in the range 839-1724 nm.

Before any measurements were taken, the DRS console was calibrated internally and probe calibration was performed in a dark room using a white reflectance standard (Ocean Optics, Dunedin, USA). After calibration and validation, the probe was inserted halfway through into the hardened optical filler samples. In total, the DRS signal at three different locations in the phantom was measured and for redundancy, ten measurements were recorded at each measurement location. After obtaining the raw spectral data, the .txt files were pre-processed by converting them to .mat files for further processing and visualization.

In case of using the raw spectral data for analysis, the ten measurements taken at one location were averaged. Because the absolute intensity signal differs per location due to varying measurement conditions, the averaged spectra were normalized with respect to 1200 nm. Pre-processing, processing and visualization of the raw spectral data was accomplished by in-house developed MATLAB scripts.

In case of using the fitting algorithm for analysis, each of the ten measurements per location was inputted into the fitting algorithm. For the pure water/fat phantoms, the option for fitting the additional silicone chromophore was turned off, and for phantoms that contained silicone it was turned on. The algorithm returns an excel sheet that contains, among other things, the estimated FF, the water+fat content, and the silicone content (all volume percentages). On top of that, it returns an excel sheet containing the confidence interval for each estimated value. The fitting algorithm does not always result in reliable estimation values, for example

because the optimization ended up at a local minimum in stead of a global minimum due to a sub-optimal starting value. In order to increase reliability, the fitted values with a confidence interval above 15% were excluded from the results. The remaining fitted results for each measurement and each location were organized per sample in a separate document, after which they could be plotted easily. Unfortunately, due to transfer errors, the spectra of sample S40-5 were not saved correctly due to which they are not shown in the results.

Results

During the production of the optical filler samples, already some valuable results were obtained. It was concluded by inspection that all the samples with medium or hard silicone and a water+fat content of 50%, no matter the fat fraction, did not result in homogeneous mixtures. Mixing the desired amounts of silicone and oily emulsion with the blender for these samples caused a lumpy composition in which the silicone and fat parts were clearly distinguishable. The mixture did not harden out well either. Figure 5.1 shows examples of well mixed samples on the left and an inhomogeneous sample on the right. During production, it was therefore decided that the last sample that was not yet manufactured with medium or hard silicone and a water+fat content of 50%, which was M50-50, would not be produced and tested anymore.

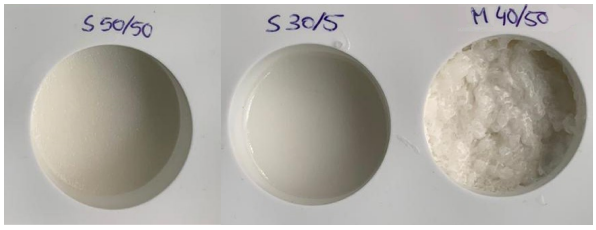

Figure 5.1: Hardened out optical filler samples of S50-50, S30-5 and M40-50

Inserting the DRS probe into the soft silicone samples with 50% water+fat content was relatively easy, without inducing high forces on the probe tip. With decreasing the amount of water+fat and thus increasing amount of silicone, the required insertion force on the probe tip increased. All the samples manufactured with the medium silicone were harder and less flexible than the samples produced with soft silicone. The samples produced with the hard silicone were even harder and less flexible. The force required to insert the DRS probe into the hard silicone samples, especially the hard silicone samples with a low water+fat content, was too large to preclude probe damage. For this reason, two perpendicular cuts were made in these phantoms in which the DRS probe was inserted.

The homogeneity of the samples can be assessed by comparing the obtained DRS signal at different locations inside the sample. For this purpose, all the spectra were normalized with respect to 1200 nm, which is approximately the wavelength at which the absorption of fat peaks. Figure 5.2 shows three examples of such plots. The remainder of the plots can be found in Appendix A. In Figure 5.2a and c, obtained from the S50-50 and S50-5 samples, the three spectra are very similar. In Figure 5.2b, obtained from the S50-20 sample, two of the three spectra are very similar, but the the third spectrum differs, especially at much lower and much higher wavelengths than the normalization wavelength.

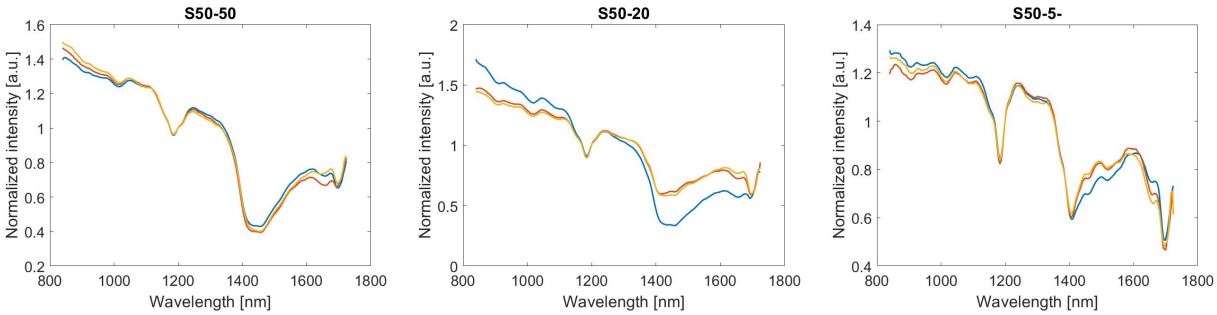

(a) (b) (c)

Figure 5.2: Plots of the averaged and normalized spectra at three different locations inside a phantom. a) spectra obtained from a hybrid optical filler sample with soft silicone, a FF of 50%, and a water+fat content of 50%. b) spectra obtained from a hybrid optical filler sample with soft silicone, a FF of 50%, and a water+fat content of 20%. c) spectra obtained from a hybrid optical filler sample with soft silicone, a FF of 50%, and a water+fat content of 5%.

In order to understand the physical meaning of the obtained spectra better, the observed dips and peaks in the example spectra of Figure 5.2 will be interpreted below. This is done by use of the standardized absorption spectra of silicone, fat, and water, shown in Figure 5.3. It should be noted that the absolute absorption per component in a phantom is not accurately represented by Figure 5.3, because it depends on the total amount present in the phantom. For example, the theoretical absorption spectrum of an optical filler sample consisting of 95% silicone and 5% water+fat with a FF of 50% is depicted in Figure 5.4a and that of a sample containing 50% silicone and 50% water+fat with a FF of 50% in Figure 5.4b. As can be seen, the silicone absorption peaks are more prominently present when the sample has a higher silicone content.

When looking at the general shape of the measured spectra, one can notice a first clear dip in the reflectance intensity around 1200 nm. The exact location of the dip for all three samples lies at 1187 nm, which is equal to the location of the absorption peak of silicone, as can be seen in Figure 5.3. Especially in Figure 5.2a, the dip is not symmetric but an additional decrease in reflectance intensity can be observed between 1203 and 1211 nm. The location of this additional absorption is in close proximity to the location of the absorption peak of fat at 1211 nm. The clearest drop in reflectance intensity for all three samples occurs between 1400 nm and 1500 nm. As can be seen in Figure 5.3, an enormous absorption peak corresponding to water coincides with this reflectance dip in the specified range.

When comparing the spectra of S50-50 and S50-5, the shape of the dip around 1400 is different. For S50-50 a broader dip can be seen that is centered around 1446 nm and for S50-5 the dominant dip, that is much more narrow, is shifted and centered around 1406 nm, followed by multiple inferior dips at 1455 nm, 1520 nm, 1554 nm, and 1660 nm. When comparing this to the standardized absorption spectra of silicone, fat, and water, the broad reflectance dip of S50-50 is in close proximity to the broad water absorption peak at 1453 nm. Sample S50-5 displays a reflectance dip that is closer to the more narrow absorption peak of silicone at 1402 nm.

Lastly, the dip at 1697 nm is present for all three samples, although on average, the dip becomes larger with increased silicone content. When looking at the standardized absorption

spectrum of silicone in Figure 5.3c, there is a coinciding absorption peak present at 1696 nm.

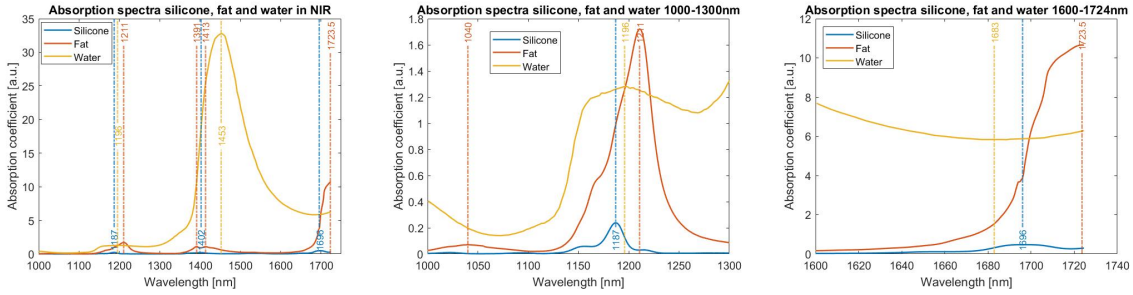

Figure 5.3: Standardized absorption spectra of silicone, fat, and water a) in the wavelength range 1000-1600 nm b) in the wavelength range 1000-1300 nm c) in the wavelength range 1600-1800 nm

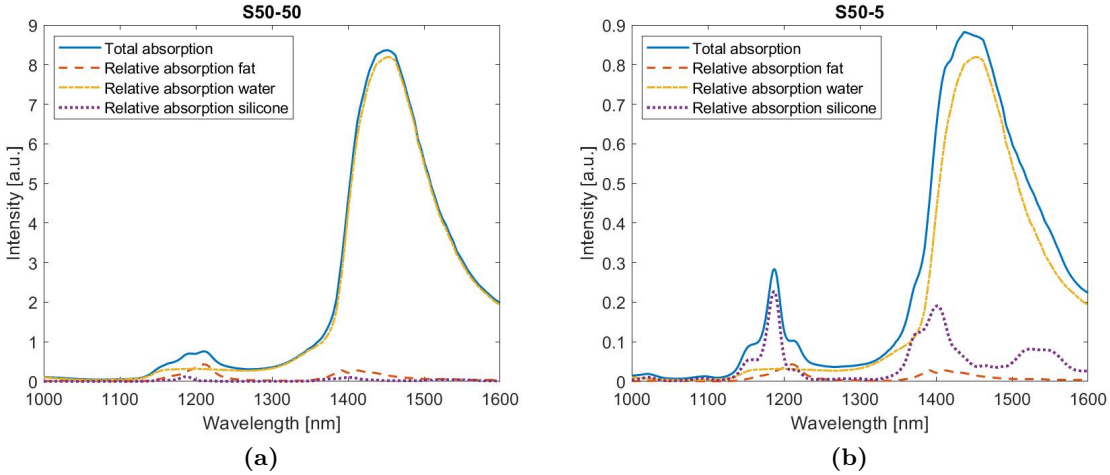

Figure 5.4: Relative absorption magnitude per component and total absorption spectrum for samples S50-50 and S50-5

Figure 5.5 shows three plots containing a measured DRS curve, the fitted curve, and the estimated scattering curve. The measurement and fitted curves seem to match very well. However, in Figure 5.5b, the fitted curve deviates from the measured curve at a wavelength just over 1200 nm, which is not the case for Figure 5.5a or 5.5c.

Figures 5.6 and 5.7 show a summary of the fitted results of all the optical filler samples. In these figures, the fitted FF, water+fat content, and silicone content are displayed. The plots are organized based on the FF of the samples and within each plot, groups are organized based on the water+fat content. It can be clearly seen that the fitted FF differs significantly from the actual FF of the samples, and that the FF variability is high for a large number of samples as well. For example, the fitted FF of the S30-5 sample varies between 0 and 60%, and should be around 30%. With the exception of S30-5 and P50, the mean estimated FF of each sample increases with increasing water+fat content in stead of staying constant.

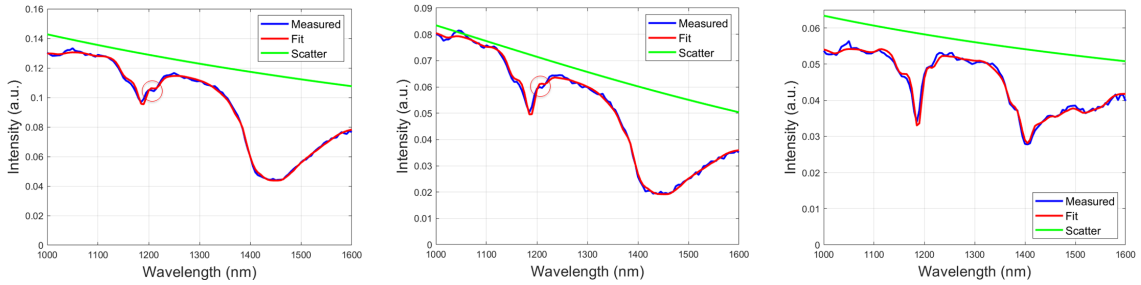

(a) Sample S50-50 **(b)** Sample S50-20 **(c)** Sample S50-5

Figure 5.5: Measured and fitted curves resulting from the fitting algorithm for a sample with soft silicone, 50% FF and a water+fat content of a) 50% b) 20% and c) 5%

When looking at the fitted water+fat content of each silicone type separately, for all samples with different FFs, the water+fat content shows a clear trend. With lower actual water+fat content, the fitted water+fat content is also low. Samples with an actual water+fat content of 5% display a fitted water+fat content mean of 8.5% (varying between 3.5% and 15.3%), samples with an actual water+fat content of 20% display a mean fitted content of 21.0% (varying between 10.1% and 35.2%), and samples with an actual water+fat content of 50% display a mean fitted content of 45.9% (varying between 25.0% and 84.6%). The mean fitted water+fat content lies relatively close to the actual water+fat content for all samples.

The fitted silicone content per silicone type also shows a trend. Samples with an actual silicone content of 95% show a mean fitted silicone content of 164.6% (varying between 115.2% and 221.2%), samples with an actual silicone content of 80% result in a fitted silicone content of 75.3% (varying between 25.4% and 158.2%), and samples with an actual silicone content of 50% result in a mean fitted silicone content of 50.8% (varying between 19.6% and 95.0%). The mean fitted silicone content of samples with an actual content of 95% deviates from the expected value a lot. The fitted silicone content of samples with an actual content of 80% and 50% lie very close to the expected values.

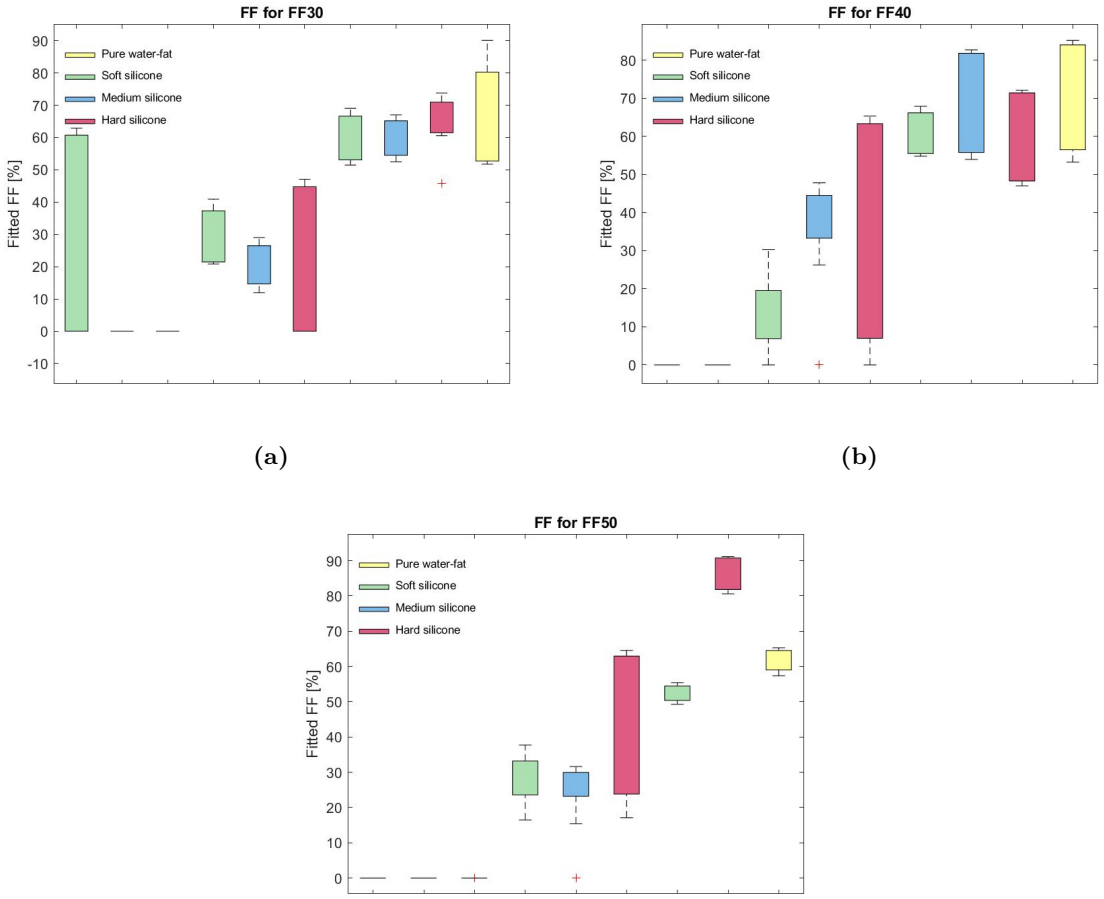

(a) (b)

(c)

Figure 5.6: Summary of the fitted FF values resulting from the fitting algorithm. Each plot shows the result per group of samples with the same FF. The samples in each plot are organized based on their total water+fat content.

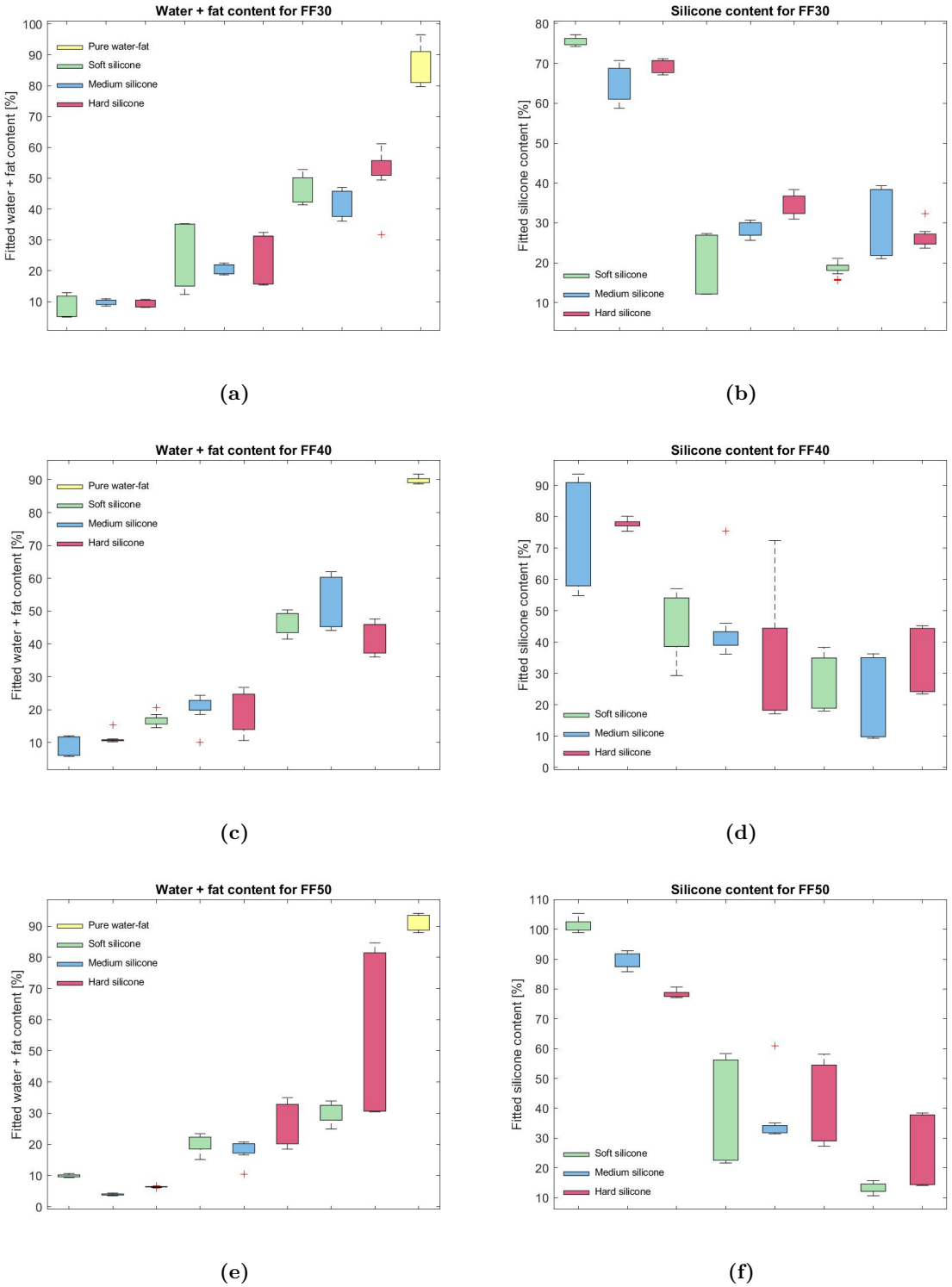

Figure 5.7: Summary of the fitted water+fat and silicone content value resulting from the fitting algorithm. Each plot shows the result per group of samples with the same FF. The samples in each plot are organized based on their total water+fat content.

Discussion

When handling the optical filler samples, it was concluded that the soft silicone samples were most similar to actual bone marrow in consistency. Furthermore soft silicone samples with the highest amount of water+fat (50%) were softest and thus resembled bone marrow best. Samples that contained a high amount of water+fat (50%) and either medium or hard silicone did not mix well. The large variance in the fitted water+fat content of sample H50-50 could be due to this inhomogeneity, although the same effect cannot be noticed for other samples complying to these requirements.

When comparing different normalized spectra within one optical filler sample (Figure 5.2 and Appendix A), one can conclude that generally, the spectra have the same shape and magnitude which could indicate homogeneity within the samples. However, some samples still show variations in spectra at different locations in the samples. This could be either due to inhomogeneity, or due to measurement errors. For example, the DRS measurement is force-dependent. Because the measurement setup did not include a probe tip force control system, the force that is present on the probe tip could have affected the measurement signal.

As more silicone is present in the S50-5 sample, the silicone absorption spectrum becomes more dominant, peaking at 1402 nm, which is in close proximity to the dominant reflectance dip of S50-5 at 1406 nm.

One can conclude from Figure 5.6 that the estimated FF from the fitting algorithm does not correspond to the actual sample FF. This means that the FF of the fitting algorithm cannot be used as a reliable parameter for distinguishing different parts of the bone phantom.

There could be multiple reasons why using the algorithm does not result in the desired FF values. First of all, the algorithm was developed and tested for (soft) human tissues and not for synthetic bone phantom [68,104], which could induce unknown factors. Furthermore, the standardized silicone absorption spectrum is a general spectrum, not necessarily exactly corresponding to the absorption spectrum of the silicone used for these specific phantoms. Although it was shown before that the absorption spectrum of peanut oil closely resembles the absorption spectrum of mammalian fat [76,86,93,103], the fact that animal fat is incorporated in the algorithm while the samples consist of peanut oil, could induce fitting errors.

Another noticeable fact is the mismatch in fitted curve just over 1200 nm for samples with a water+fat content of 20%. As explained in Chapter 1, the fitting algorithm relies on the fact that the fat content is fitted correctly in human tissues because absorption of fat at 1211 nm is dominant over the absorption of water at this wavelength. The absorption peak of silicone is centered at 1187 which introduces an additional dip in the reflectance signal. Because of the incorporated optimization method (Levenberg-Marquardt non-linear least squares optimization), it could be that the added silicone in the samples introduces an error in the fat curve fitting, especially for samples with a high silicone content. With higher silicone content, the silicone dip at 1187 nm becomes more pronounced and the fat dip at 1211 nm becomes less pronounced. Therefore, during fitting, the silicone dip mainly determines the curve shape and match, and the effect of the fat dip is overshadowed. This would result in an incorrect fat content and thus an incorrect FF as well.

Apart from the closely estimated water+fat content, there exists a close relation between the actual water+fat content and the fitted water+fat content for phantoms with varying water+fat contents. Since the water+fat content in cortical bone is significantly lower than the water+fat content in cancellous bone (23.5% vs 58.3%, as discussed in Chapter 1), the water+fat content could be a good alternative to the FF parameter that was investigated previously, while still being able to make use of the same DRS and fitting algorithm for optical guiding.

Because the aim is to design a phantom that can be used for drilling with a DRS-based optical guiding system to detect the boundary between cortical and cancellous bone, the cancellous bone phantom that consists of a 3D printed structural matrix and an optical filler, should aim for a water+fat content of approximately 58.3%. This means that the optical filler should consist of an even higher water+fat content, of which the exact value is dependent on the BVF of the cancellous bone structure. For example, it was investigated by Nouh et al. [26], that yellow bone marrow consists of 95% water+fat. For optical filler samples containing water, fat, and silicone, like the ones discussed above, such a high water+fat content is not feasible because it will result in, amongst other things, mixing issues due to silicone hydrophobia, lipophobia, and saturation. Since producing samples with a water+fat content and a silicone content of 50% was still feasible, this option would result in the closes approximation of water+fat content in bone marrow situated in cancellous bone, and thus in the most reliable differentiation results.

There exists a positive relation between the actual silicone content and the fitted silicone content too, as can be seen in Figure 5.7. However, the variability per sample is generally larger and fitted silicone content for samples with an actual silicone content of 95% is greatly overestimated.

5.1.2 Optical phantom stability

One of the functional requirements states that the phantom should maintain its physical and optical characteristics for at least 8 weeks. Because standard optical phantoms degrade over time and only maintain their intended composition for a period of a few hours to a few days, the phantoms were enhanced with silicone. To test if the added silicone contributes to the optical stability and preservability of the optical samples, the appearance and optical properties of the samples were monitored over a period of 10 weeks.

Method

In week 0 the samples were produced and DRS signals were obtained as described previously. After that, the samples were stored with a plastic wrap in a fridge. In week 10 after production, all the samples were removed from the fridge and inspected visually. On top of that, DRS measurements were performed for promising samples, defined as samples that were easy to produce, mixed well, had predictable optical properties, and seemed stable after inspection in week 10. As discussed in the previous section, optical filler samples containing soft silicone and a high water+fat were most promising, first of all because their consistency was most similar to bone marrow, and secondly because the fitting output parameters most

resembled cancellous bone (filled with bone marrow). For this reason, the DRS signals of only six samples were measured, namely samples S30-30, S30-50, S40-20, S40-50, S50-20 and S50-50.

The DRS measurements were performed in the same manner as the DRS measurements of week 0. Both the raw spectra (at a normalization wavelength of 1200 nm) and the fitting output parameters the samples were compared over time. Out of the fitting parameters, only the fitted water+fat content of the samples was used to assess stability because this parameter showed the most reliable fitting results and was therefore proposed as an alternative to the previously investigated FF differentiation parameter.

Results

Firstly, all the samples that were initially produced, were inspected visually. Figure 5.8 shows a selection of optical samples after 10 weeks storage in a fridge. The samples that are in the left top and bottom of Figure 5.8a are full of mold and are surrounded by leaked oil. These samples are pure water/fat samples without silicone enhancement. All the samples made out of soft silicone do not show any signs of mold. Sample M40-50 in the bottom of Figure 5.8b and sample H30-50 in the upper right corner of Figure 5.8c do show signs of mold.

In Figure 5.9, the averaged raw spectra at three different locations inside soft silicone optical filler samples with 20% and 50% water+fat content at week 0 and at week 10 are displayed. As can be seen in this figure, not all six spectra are exactly the same. However, there is no consistent significant relation between the two different time intervals. Both time intervals contain spectra that differ.

Figure 5.10 shows the fitted water+fat content of the same samples. As can be seen, for every different FF, the fitted water+fat content of samples with an actual water+fat content of 20% is structurally lower than that of samples with a water+fat content of 50%. The fitted values of week 0 differ from the fitted values of week 10, but there is no trend present. For samples with a FF of 30%, the fitted value of week 10 is within the same range as the fitted value of week 0 for 20% water+fat, and for 50% water+fat, it is slightly lower. For samples with a FF of 40%, the fitted value with a water+fat content of 20% is slightly higher in week 10, and for a water+fat content of 50% it is in the same range with a larger variance. For samples with a FF of 50% the fitted values of samples with a water+fat content of 20% are in the same range, but the variance is larger in week 10, and the fitted values of samples with a water+fat content of 50% are larger with a larger variance as well.

Discussion

Figure 5.8 showed very well that samples without silicone enhancement deteriorated a lot, leading to oil leakage and mold growth. Comparing these samples with samples containing (large) amounts of silicone, we see a big difference in preservability, as none of the samples with 95% silicone or 80% silicone grew mold. This fact confirms the hypothesis that adding silicone to a homogeneous mixture of water and fat improves optical phantom preservability.

Already during production of the test samples, it was concluded that samples with medium or hard silicone and a water+fat content of 50% did not mix well and resulted in a lumpy sample texture. When looking at these samples after a period of 10 weeks, we see that multiple

deteriorated and grew mold on them. This is yet another indication that the phantoms are inhomogeneous and unsuitable for reliable, stable bone phantom production. None of the soft silicone samples grew mold on them which is a very promising result because it indicates that the silicone was mixed well with the water and fat, and that the silicone actually improves the stability and preservability of optical phantoms.

Because the spectra obtained at the two time intervals did not structurally differ from each other (Figure 5.9) and the fitted water+fat content values obtained in week 10 are not structurally lower or higher than the values obtained in week 0 (Figure 5.10), it was concluded that the difference between the spectra and the fitted values of the two groups was not caused by sample age, but for example by small inhomogeneities, measurement errors, or fitting errors.

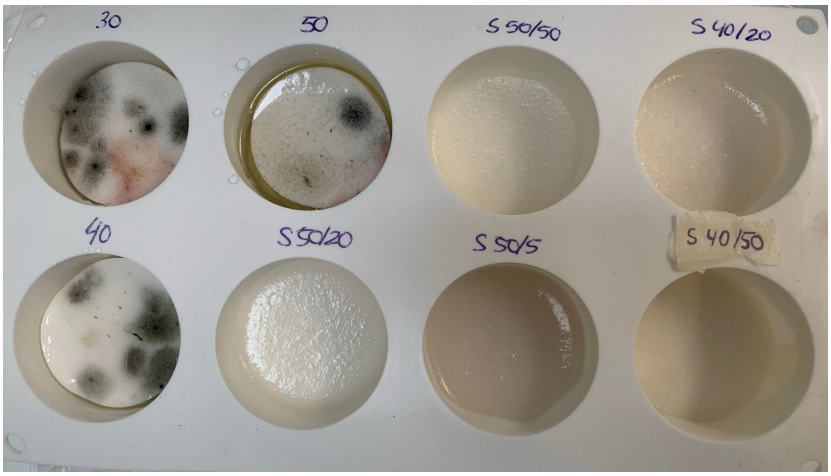

(a)

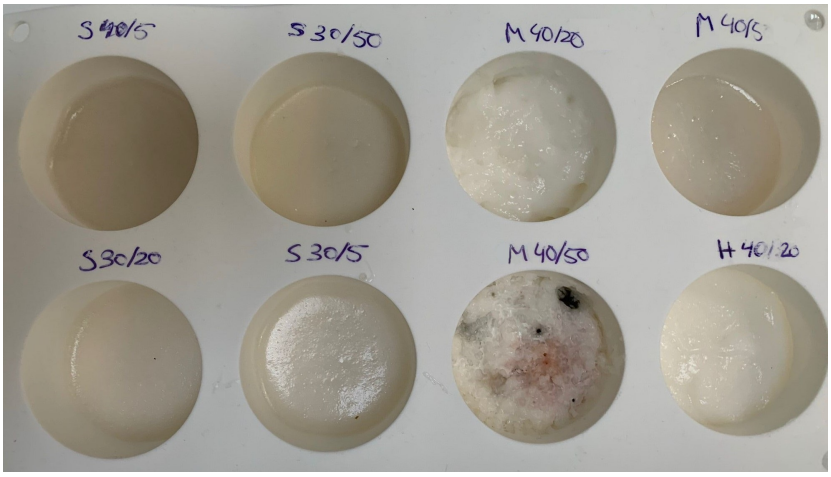

(b)

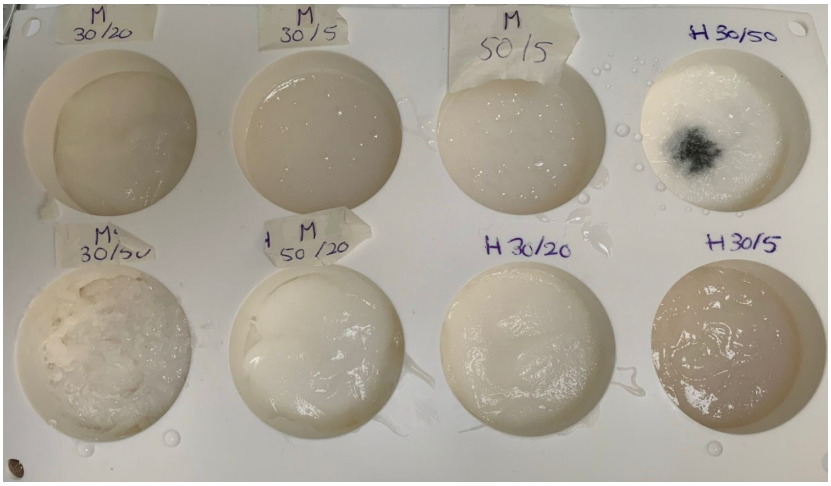

(c)

Figure 5.8: Pictures of the appearance of a selection of optical filler samples after 10 weeks storage in a fridge

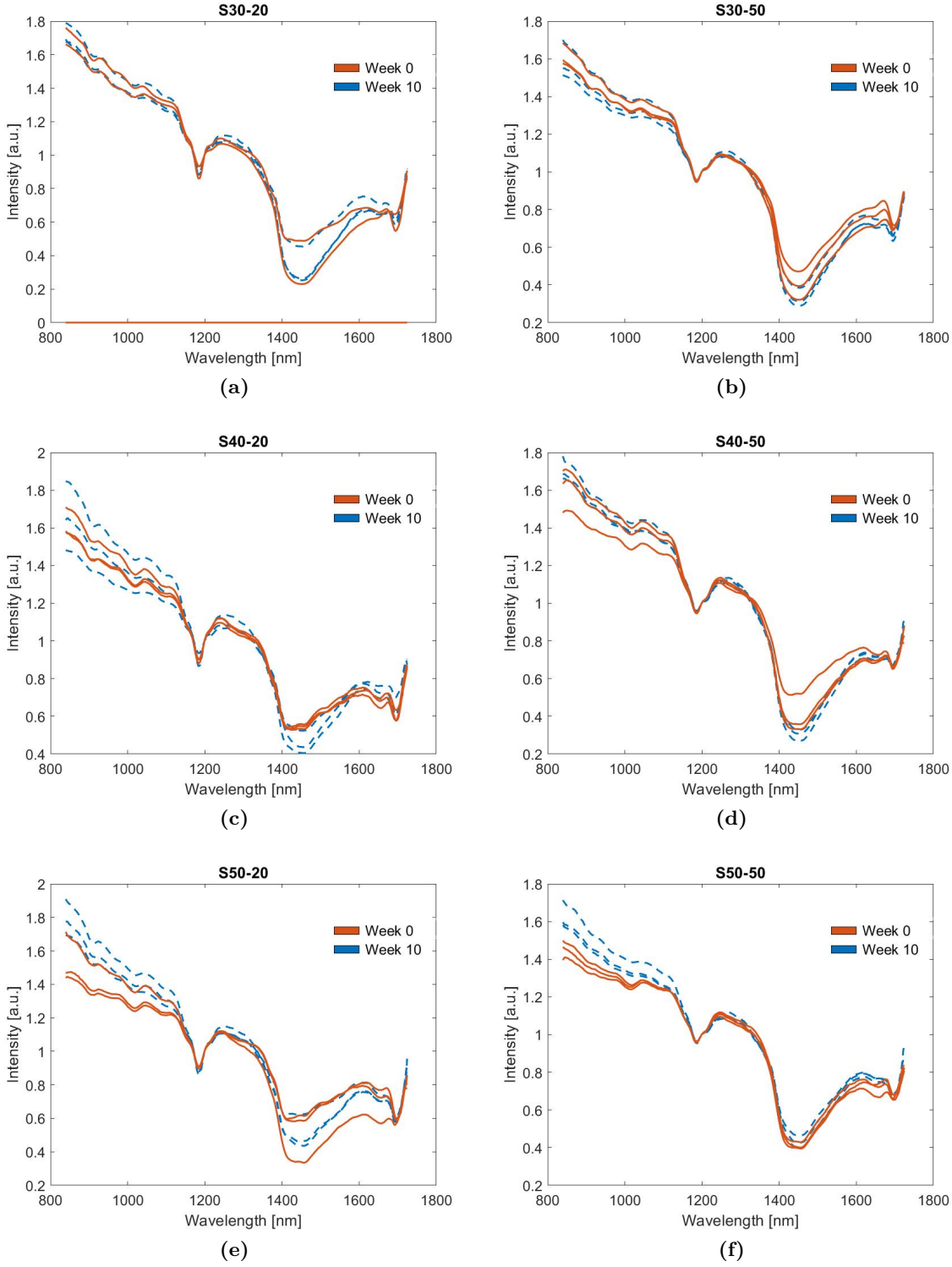

Figure 5.9: Averaged raw spectra at three measurement locations in week 0 and week 10.

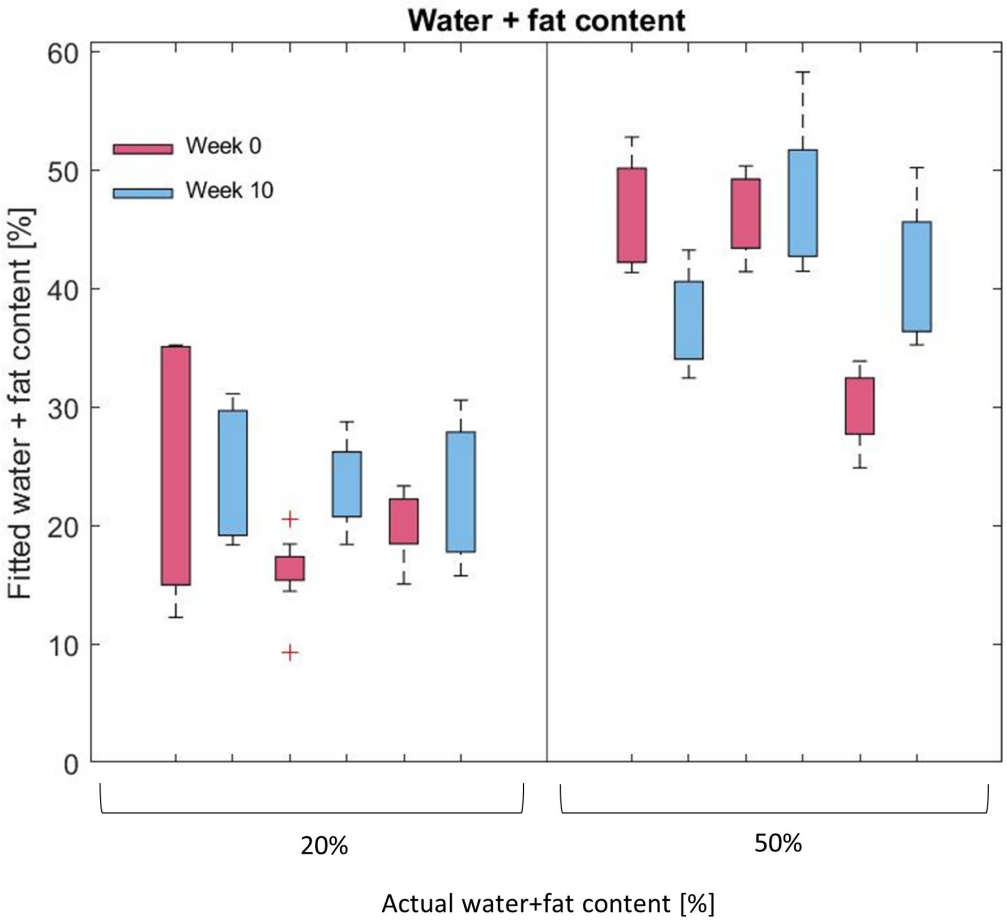

Figure 5.10: Summary of the fitted water+fat content of all soft silicone samples with different FF and either 20% or 50% actual water+fat content.

5.2 Structural tests

The design choice was made to 3D print a structural matrix to mimic the material properties of cortical and cancellous solid bone. There are various methods for modelling the porous cancellous structure of the matrix and 3D printing the obtained model. To investigate which modelling and 3D printing method is most suitable for this application, first, various models and 3D printers were tested in the 3D printing feasibility test. After a modelling method and 3D printer were chosen, the structural characteristics of various modelling parameters was investigated by performing a material drill test and a material compression test.

5.2.1 3D printing feasibility

There are several modelling methods and 3D printing methods for manufacturing the structural matrix of a bone phantom. As discussed in Chapter 2, previous studies have 3D printed a replica of a chimpanzee's cancellous bone structure, of which the model was obtained from a 3D micro-CT scan [12]. The 3D printer that was used, was an SLA printer. Another study printed a generalized porous cancellous bone phantom of which the model consisted of a gyroid structure which was printed by an inkjet printer [81]. A different study investigated the use of different printing materials, infill patterns, infill percentages and infill orientations on an FDM printer [100].

Because the previously mentioned studies did not try to mimic the absolute material properties of human vertebral cancellous bone, but rather compared different model parameters, the results of these studies cannot simply be adopted for this specific application. In order to investigate what the most suitable approach is for 3D printing a cancellous bone matrix with the structural properties reported in Chapter 3, different models, printers, and materials were tested.

Method

First of all, the structural characteristics of cancellous bone are different for every individual, due to differences in organic shape, BVF, BMD, age, loading direction etc. Because of this, there exists no standard cancellous structure that represents all cancellous bone. Therefore, the choice was made not to use a micro-CT scan of real cancellous bone for the structural matrix model, but rather the symmetric, organic, mathematical 3D structure of a gyroid, as investigated by Burkhard et al. [81]. The gyroid roughly fulfills the description of isotropic plate-like trabeculae. One of the conclusions of their study was that a gyroid structure with a unit cell of 0.9 mm and a trabecular thickness of 0.3 mm, printed with the VisiJet CR-CL 200 (3D Systems, Rock Hill, SC, USA) material on an inkjet printer best mimicked real healthy human vertebral bone.

The model depicted in Figure 5.11 was made with the nTopology (New York, USA) modelling software and printed on both available printers, the Formlabs SLA and the Ultimaker FDM printer. This software was chosen because it includes a function that generates a thin walled triply periodic minimal surface (TPMS) gyroid structure, of which parameters such as the unit cell size and the wall thickness can be adjusted according to preferences with a

high degree of flexibility. The outer shape of the model is based on the average dimensions of the human vertebral body discussed in Chapters 1 and 3. The model ML diameter is 35 mm while the AP diameter is 26 mm. The model only represents half of a vertebral body in order to expose the internal structure of the 3D print. The model has an outer solid cortical layer of 1 mm thick and an inner core made out of a TPMS gyroid structure with a unit cell dimension of 0.9 mm and a trabecular thickness of 0.3 mm. The dimensions of the gyroid structure are based on the findings reported by Burkhard et al. [81]. The model also contains a pre-cortical zone with a thickness of 3 mm in which the trabecular thickness of the gyroid structure linearly increases from 0.3 mm to 0.9 mm (100% infill).

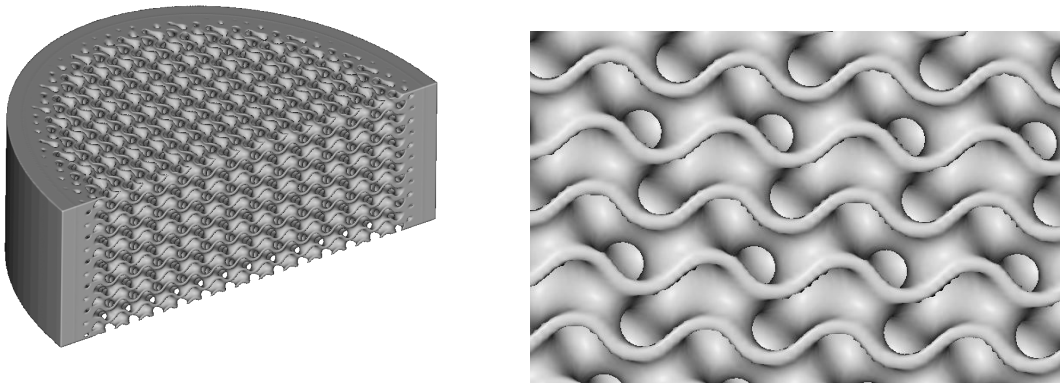

(a) **(b)**

Figure 5.11: Figure a) shows the CAD model that was printed on the Formlabs SLA printer and Ultimaker FDM printer. Figure b) shows a zoomed in view of the gyroid structure of the model

Since, in the research by Burkhard et al. [81], gyroid structures with different trabecular thicknesses were subjectively assessed by surgeons upon handling, no absolute material characteristics were reported such as material stiffness or strength. To meet the requirements generated in Chapter 3, these material properties should be tested and validated before the same model can be adopted. Because the available printers are not compatible with the VisiJet CR-CL material, other materials that have the same characteristics and that are compatible with the Formlabs and Ultimaker printers should be selected.

The reported E-Modulus of the VisiJet CR-CL material varies between 1.4-2.1 GPa and the ultimate tensile strength varies between 30-43 MPa. The two most commonly used materials for FDM are (tough) PLA and ABS. When comparing ABS and PLA, ABS has a higher E-Modulus of 1.6 GPa and a higher ultimate tensile stress of 33.9 MPa, which are both within the values reported for the VisiJet CR-CL material. On top of that, ABS has a higher glass transition temperature of 97°C compared to PLA ($\tilde{6}$0°C), which is favourable for Requirement 1.5. For these reasons, the choice was made to use ABS material to print the structural matrix on the Ultimaker printer. Research by Bohl et al. [100] confirmed that ABS is a better material for bone mimicking than PLA. For the Formlabs SLA printer, the material that was most similar to the VisiJet CR-CL material, was the uncured standard resin that has an E-Modulus of 1.6 GPa and an ultimate tensile strength of 38 MPa.

On top of that, another research group at the Delft University of Technology recently used

a novel FDM material that was especially designed for printing bone structures. This material was developed by Smart Materials [105] and consists of PLA enhanced with minerals (calcium). Because of the added minerals, the print would give better contrast on optical images and would have increased strength and stiffness. Because not much is known about the material and its printing, optical, and structural characteristics, this material was also included in the preliminary testing phase.

The Formlabs print was printed by use of full ramp supports and a layer thickness of 0.05 mm. The Ultimaker print was printed with a 0.2 mm nozzle, a 0.1 mm layer thickness, no supports and either standard ABS print material settings (for the ABS print, printing temperature 225°C and build plate temperature 80°C) or PLA print material settings (for the Smart Materials print, printing temperature 190°C and build plate temperature 80°C).

Results and conclusions

When meshing the model containing the gyroid structure depicted in Figure 5.11, the size of the meshed file becomes enormous. The reason for this is the highly detailed internal structure of the model. The size of the meshed file caused handling issues during loading into the slicing softwares Preform and Cura. Because of the high detail, Cura was not able to read the mesh file properly and to slice the model efficiently, due to which model fixing had to be carried out in the Meshmixer (Autodesk Meshmixer, Autodesk. Inc., San Rafael, California, USA) program before slicing.

Figure 5.12 shows two pictures of the printed parts of the model described above from the Formlabs SLA printer and from the Ultimaker FDM printer. The SLA print is supported by full ramp supports. The small pores in the model, in combination with the SLA printing method, resulted in clogged pores. The resin that is naturally viscous, could not be removed from the pores, even after extensive cleaning in an alcohol bath. The FDM print made out of ABS came out really well, with high detail and open pores. The FDM print made out of calcium enhanced PLA had a rough surface finish and a messy-looking gyroid structure. On top of that, the weight of the part was 3.98 g in stead of the intended 2.66 g, which is an indication that the printing process did not result in the designed model.

In general, SLA printers are able to print parts with more detail and a better surface finish. However, because the working principle of SLA printing is based on curing liquid resin, printing a detailed porous structure will cause problems with removing the residual resin from the pores. For this reason, an FDM printer is better suitable for printing this bone phantom part. Because the part made out of calcium enhanced PLA did not result in the desired weight and surface finish but the ABS part did, the choice was made to use ABS as the final structural matrix material.

Because the enormous mesh file of the model already containing the gyroid structure caused loading and reading problems in Cura, an alternative modelling approach was opted for. Only a solid block of the outer dimensions of the model was used as in input for Cura, and the gyroid infill pattern was modelled inside Cura. Unfortunately, by taking this approach, some gyroid model parameters could not be controlled anymore, such as the trabecular thickness (gyroid wall thickness) and the linearly increasing gradient. As an alternative, the gyroid infill density per model section could be controlled.

(a) Formlabs SLA print made out of Formlabs standard resin

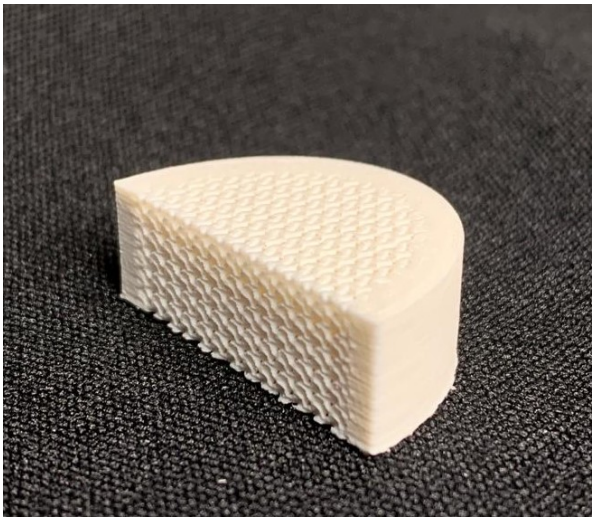

(b) Ultimaker FDM print made out of ABS

Figure 5.12: Pictures of the prints of the model shown in Figure 5.11.

5.2.2 Structural drill characteristics

As can be seen in Table 3.3 the most important structural requirement is the drill force in the cancellous bone. Various different structural matrices made out of ABS with different infill densities were tested for their structural drill characteristics in order to determine which infill density mimics healthy and osteoporotic human vertebral cancellous bone best.

Method

In total, three 3D printed designs were tested on their drill material characteristics. The three designs were made out of ABS and had a Cura infill density setting of 40%, 50% and 65%. Each test sample was a square block of 30x30 mm with a height of 20 mm, of which 17 mm was cancellous bone and the bottom 3 mm was solid printed material. For now, no structural gradient was incorporated into the structural matrix. The test samples were manufactured with an Ultimaker 3 printer. A schematic drawing and a picture of the test setup can be seen in Figure 5.13. Figure 5.13a shows the side view of the setup, with the rotation speed and feed rate as inputs, and the axial force as an output. Figure 5.13b shows the front view of the setup. For redundancy, three drilling cycles were measured of each sample, and the drill penetrated

The linear stage that provides the feed rate is driven by a magnetic direct drive linear motor. A custom mount is bolted on to the linear stage, that connects the drill to the stage. The drill is driven by a NEMA 23 Makeblock 57BYG stepper motor. An Arduino UNO USB board is used to control the rotation and acceleration of the drill. A 25 lbs Futek load cell is used to measure the axial force on the drill bit. It is placed under the sample and the middle of the load cell is aligned with the longitudinal axis of the drill. All details of the mount, stepper motor, linear stage and load cell used in this drill test setup have been described

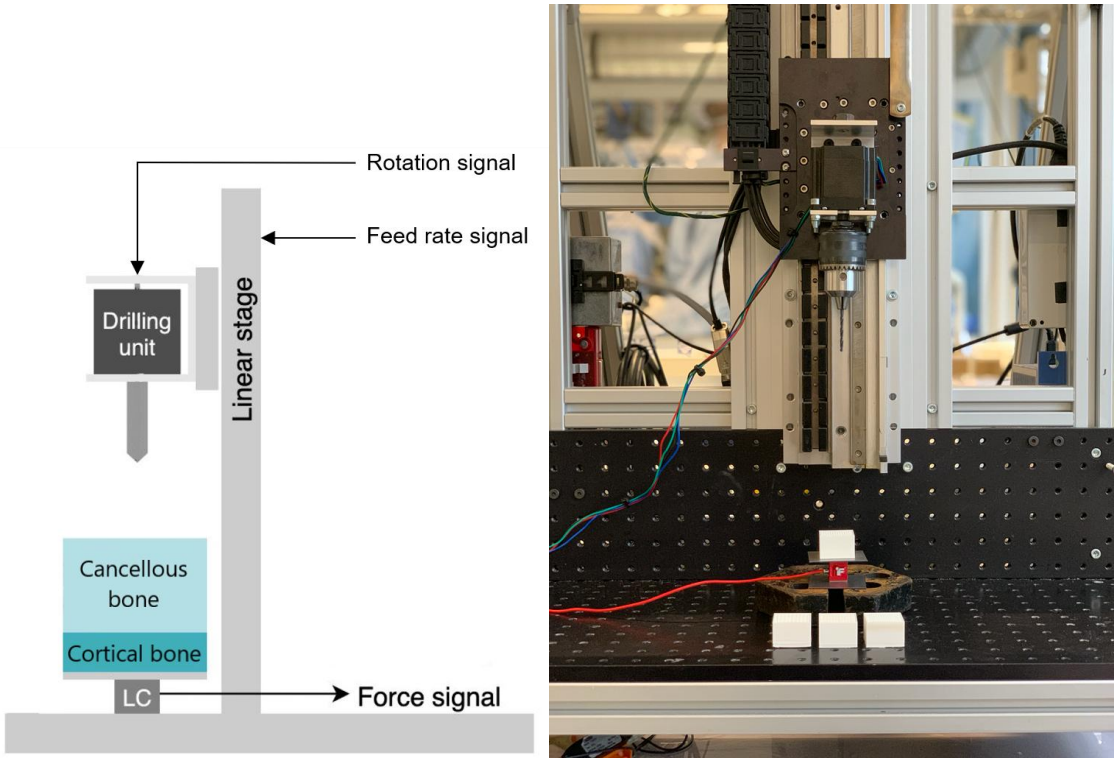

(a) Schematic drawing of the drill test setup. LC = load cell (adapted from [34])

(b) Picture of the drill test setup. The red part is the load cell connected to the Labview measurement hardware and the white blocks are the test samples, of which one is lined up for the drill test and three are in stand-by.

Figure 5.13: The drill test setup

previously [34]. Two adjustments were made to the test setup. Firstly, the sample is only resting on the load cell and is not placed on a hinge. In this manner the axial force on the drill is directly measured. Secondly, no optical measurements were taken during drilling, such that the specifications mentioning the DRS console can be discarded.

Results

Two examples of clear force measurement signals are presented in Figure 5.14. The results of all the samples can be found in Appendix B. With signal post-processing, the time of sample penetration is determined, which is the first time instance at which a force increase is registered. The time at which the axial force on the drill is twice as high as the average after insertion, is depicted in the graph as the second force increase (the solid line). The third time instance that is shown in the graph, is the time at which the drill actually reaches the cancellous-cortical boundary, which is deduced from the sample penetration time, the thickness of the cancellous bone, and the feed rate of the drill.

From the figure, a clear difference can be seen between drilling environments. The first 17

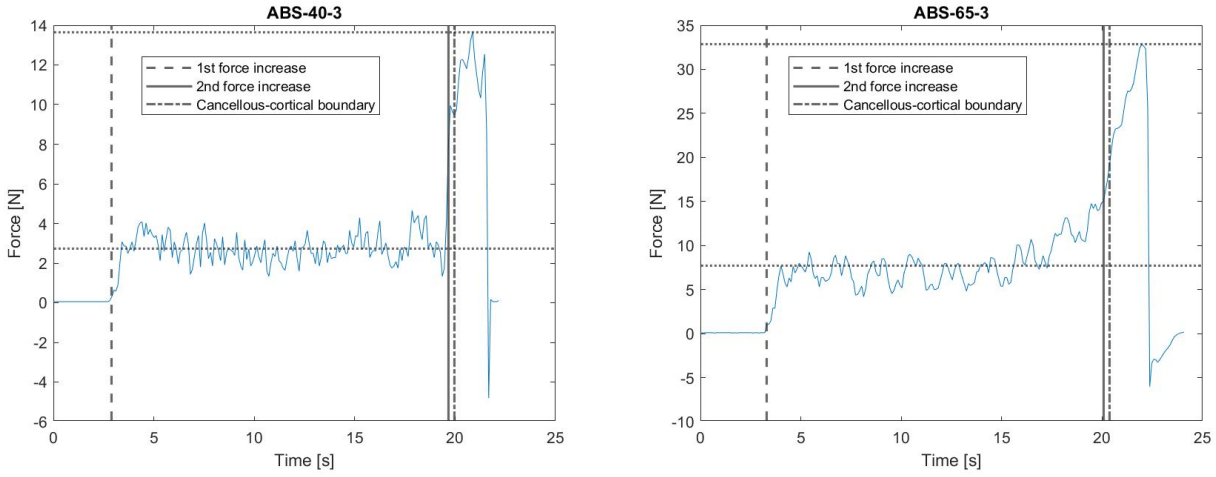

(a) **(b)**

Figure 5.14: Axial force on the drill as a function of time while drilling in an ABS sample with a) 40% infill density and b) 65% infill density. The samples do not contain an optical filler. In the figure, the mean force in the core of the phantom is indicated with a horizontal dotted line, as well as the peak force in the cortical part of the phantom.

seconds after sample penetration the force signal fluctuates heavily and has a lower mean force. Just before the cancellous-cortical boundary the force suddenly increases and experiences a peak value. During retraction of the drill, a negative force minimum is registered. The average axial force on the drill in the cancellous bone is lower than the force in the cortical bone layer. Lastly, the time instance of the second force increase generally corresponds well with the time instance of the actual cancellous-cortical boundary penetration.

In order to compare different infill densities, the mean force measured in the cancellous bone layer, the force range in the cancellous bone layer, and the peak force measured in the cortical bone layer of the tree subsequent measurements in the same test sample are summarized in Table 5.2, together with the target values determined in Chapter 3 (F_{ph} is the peak force in cortical bone of healthy bone material and F_{po} is the peak force in cortical bone of osteoporotic bone material).

Discussion

The fluctuating force signal in the cancellous bone can be explained by the discontinuous contact between the drill and the trabeculae, which is caused by the microstructural architecture of the cancellous bone, and has been reported previously for cancellous bone phantom and real human bone as well [34, 55]. Because the drill bit and the drill axes were slightly misaligned, the test sample vibrated during insertion, which could also be an explanation for the fluctuations in the cancellous bone part of the sample.

The average axial force on the drill in the cancellous bone is lower than the force in the cortical bone layer, which was expected and has been reported before as well [34, 53–55, 65, 106, 107]. The mean cancellous force, the cancellous force range, and the peak cortical force increase with increasing infill density, which is also a logical result.

Sample	Mean cancellous force (N)	Range cancellous force (N)	Peak cortical force (N), F_p
ABS 40%	2.6 ± 0.4	$0.0 - 7.9$	13.3 ± 0.4
ABS 50%	4.6 ± 0.1	$0.0 - 11.5$	21.2 ± 3.2
ABS 65%	7.6 ± 0.3	$0.0 - 17.2$	33.7 ± 2.6
Target healthy	6.0	$0.0 - 10.0$	>30.0 ($=F_{ph}$)
Target osteoporotic	1.2	$0.0 - 2.0$	$F_{po}<F_{ph}$

Table 5.2: A summary of the mean force measured in the cancellous bone part, the force range in the cancellous bone part, and the peak force in the cortical bone part of the phantom, for three phantom designs with different infill densities. The standard deviation is mentioned behind the corresponding values. The target values for healthy and osteoporotic bone that were determined in Chapter 3 are mentioned as well.

When comparing the measured mean cancellous force of the samples to the requirements generated in Chapter 3, we can conclude that the part with 50% infill with a mean force of 4.6 N comes closest to target value of 6 N for healthy bone. The cancellous bone drilling force range of 0.0-11.5 N of the 50% infill part also comes closest to the target range of 0.0-10.0 N. The target peak force in cortical bone is at least 30 N, which means that the ABS part with 65% infill is more suitable to meet this requirement. However, since the requirement for the drill force in cancellous bone is considered more important than the drill force in the cortical bone, the design choice was made to print the structural matrix of the bone phantom with a Cura infill density of 50%.

When comparing the target for osteoporotic bone to the values measured for different infill densities, we can conclude that the mean cancellous force of a phantom with 40% infill density, which is 2.6 N, is still more than a factor 2 too high. The range in the cancellous force of this phantom fluctuates between 0.0 and 7.9 N which means that it is almost a factor of 4 too high. Because both the measured mean cancellous force and cancellous force range are significantly higher than the target values, a lower infill density than 40% should be investigated to mimic osteoporotic cancellous bone.

5.2.3 Structural compression characteristics

In order to reduce uncertainty about the structural characteristics of the phantom, not only a drill test was carried out, but also a compression test. From the compression test, the structural strength and stiffness of different phantom designs can be deduced. The same structural matrices as mentioned above made out of ABS (40%, 50% and 65% infill density) were tested in compression. The resulting approximate E-Modulus and yield strength of the samples were compared to the strength and stiffness values of human vertebral cancellous bone reported in literature.

Method

The test samples were cylinders with a diameter of 20 mm and a length of 30 mm. Each sample type consisted of only a Cura gyroid infill structure without a solid bottom, top, or

walls, with an infill density of 40%, 50% or 65%. Each sample type was produced and tested five times, and the samples were produced in four different batches to avoid measurement errors due to printing flaws.

The test samples were compressed with a Lloyds Instruments LR5K test bench with a maximum compression force of 5 kN. The samples were clamped between two circular fixtures with a preload between 10 and 20 N. The strain rate was set to 0.001 s^{-1} and the maximum deflection was set to 5 mm.

Results and conclusions

Figure 5.15 shows examples of stress-strain curves of five redundant samples of two print designs. The stress-strain curves of all the samples can be found in Appendix C. The first part of the graph that follows a linear line, represents the linear elastic part of the structural deformation. The slope of the linear part of the graph is an approximation of the E-Modulus of the sample, and is indicated with the dotted line. The yield strength of the samples was calculated by use of the 0.2% offset method. In order to compare the print designs to real human cancellous bone material, the E-Modulus and yield strength of each sample was averaged over the five redundant measurements. The results are shown in Table 5.3.

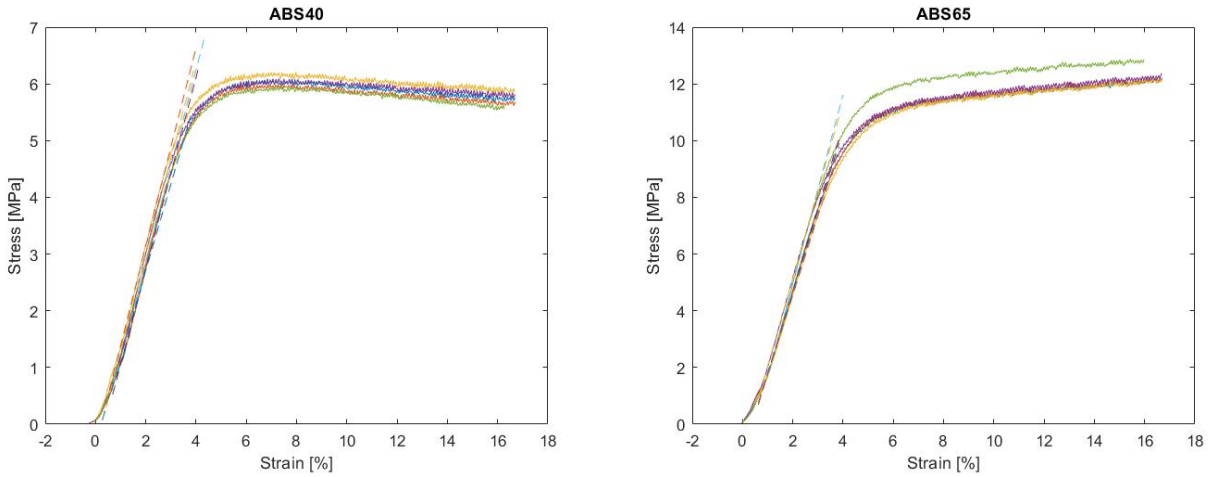

(a) (b)

Figure 5.15: Stress-strain curve of an ABS sample with a) 40% infill density and b) 65% infill density.

As can be seen in Figure 5.15, the stress-strain curves of the five redundant samples are really similar. The slope of the linear-elastic part of the graphs have a big degree of similarity and the maximum force is in the same order of magnitude. From Table 5.3 it can be noticed that both the E-Modulus and the Yield strength increase with increasing sample infill density, which is a very logical result. When comparing the obtained values with the targets set in Chapter 3, all samples have a higher E-Modulus than the target E-Modulus of 94.5 MPa, and a higher yield strength than the target yield strength of 2.0 MPa as well. For this reason, the design with the lowest infill density of 40% (but preferably even lower) would

be the best option for meeting the stiffness and strength requirements. However, from these measurements one can conclude that the E-Modulus and yield strength requirements are conflicting with the drill characteristic requirements. The choice was made to focus on the highest ranked requirement, which is the cancellous bone drill force requirement. This means that the healthy bone phantom will have an infill density of 50%. It was already concluded in the previous section that the osteoporotic bone phantom should have a infill density below 40% and the results in Table 5.3 confirm this.

Sample	**E-Modulus (MPa)**	**Yield strength (MPa)**
ABS 40%	167.2 ± 0.1	5.1 ± 0.2
ABS 50%	237.4 ± 0.1	7.0 ± 0.3
ABS 65%	300.0 ± 0.2	9.0 ± 0.2
Target healthy	94.5	2.0
Target osteoporotic	47.3	<2.0

Table 5.3: Summary of the E-Modulus and Yield strength of three phantom designs with different infill densities. The standard deviation is mentioned behind the corresponding values. The target values for healthy and osteoporotic bone that ere determined in Chapter 3 are mentioned as well.

Part III

Third part: Design validation

Chapter 6

Integrated phantom validation

Up till now, optical and structural parts of the phantom design have been tested and evaluated separately. In order to validate that combining the optical filler and the structural matrix will result in a phantom that meets the requirements set in the problem analysis, an integrated test should be carried out. This chapter will discuss the manufacturability, optical absorption characteristics, optical gradient, structural drill characteristics, and structural gradient. The material stiffness and strength are not tested because it was shown previously that these requirements are conflicting with the structural drill characteristics, which are more important for the application of a pedicle screw fixation procedure.

6.1 Method

Ideally, one would want to perform a drill procedure in the bone phantom that mimics real bone drilling as close as possible, while measuring both the DRS signal and axial force on the drill simultaneously with a high frequency. This measurement setup requires custom equipment and such a test has high degree of complexity if carried out correctly and accurately. Unfortunately, such a measurement setup was not available because the DRS signal acquisition time was too long to do real time measurements. On top of that, no linear stage was available that had a high enough accuracy for drill insertion every 0.5 mm. For the above mentioned reasons, multiple duplicates of integrated test samples were produced that were tested separately for their optical properties and structural properties. It was assumed that the inter-sample differences were negligible.

6.1.1 Structural matrix

The integrated phantom test samples were simple square blocks with a width of 30 mm and a height of 16 mm. The structural matrix of the phantom is made out of ABS, printed on an Ultimaker 3 printer and consists of a gyroid core with an infill density of 50%. Towards the

bottom of the model, there is a structural gradient present. Because the infill was modelled in Cura, which does not contain a function for linearly changing the infill density, the structural gradient was modelled with steps of 2 mm thickness. With increasing distance from the bottom edge of the phantom, the infill density decreased from 100% at the first 3 mm, to 90% at 3-5 mm from the edge, to 80% at 5-7 mm, to 70% at 7-9 mm, to 60% at 9-11 mm, and the remainder of the phantom had a 50% infill. This means that the modelled pre-cortical zone is 8 mm thick in stead of the target thickness of 3 mm. A larger pre-cortical zone was modelled to visualize the gradient better although in the future, a model with the target pre-cortical zone thickness should be tested as well.

6.1.2 Optical filler

The initial idea was to fill the structural matrix described above with the chosen optical filler from the preliminary optical tests of Section 5.1 with a water+fat content of 50% and a FF of 40%, because this optical filler feasibility was already validated. However, some problems were encountered during the infusion process. The infusion of samples with pure silicone as a filler was successful but the infusion of samples with the hybrid filler was not successful because the filler hardened out before it was able to infuse into the structural matrix pores. One explanation for this could be the fact that the silicone fraction of the filler hardens out at elevated temperatures but the oily emulsion fraction hardens out at low temperatures. By mixing the hot oily emulsion (which was hot because of the minimum required melting temperature of agar ($\tilde{8}5$°C)) with the cold silicone fraction, the curing process of both fractions got accelerated and the filler did not get the chance to infuse into the structural matrix before hardening. To solve this issue, alternative emulsifiers were investigated.

Because it was suspected that the optical filler did not infuse well into the matrix because of the difference in curing properties of the silicone and the emulsifier, an emulsifier which is soluble in cold water was used to substitute the agar agar emulsifier. The assumption was made that, as long as the water fraction, FF, and silicone fraction stayed the same, and the hybrid filler well mixed, the absorption, optical stability, and preservability characteristics of the filler were not significantly different compared to the previously evaluated optical filler with agar agar. An optical filler sample with a 1 wt% of Xanthan gum of the oily emulsion as emulsifier, a water+fat content of 50%, a FF of 40%, and 50% soft silicone content mixed well, infused well, and hardened out without lumps. In total, four samples with the structural matrix and hybrid optical filler described above were manufactured for the integrated test, of which two were tested for their optical properties and two were tested for their structural properties.

6.1.3 Integration

The filler that is added to the phantom for its optical properties was infused into the structural matrix. Because the pores of the the structural matrix are small, the filler does not flow into the matrix naturally, but must be forced in. This was done with a vacuum chamber. The 3D printed structural matrix was put in a mould and the liquid optical filler was poured on top of the matrix. After that, the mould was left in a vacuum chamber for at least 40

minutes to pull the air bubbles captured in the pores out and to force the liquid filler in. The infusion process was assessed by measuring the weight of the part before and after infusion and comparing it to the theoretical weight of a successfully infused part.

6.1.4 Test setup

It was shown before that phantoms with different water+fat contents display very distinct spectra with characteristic dips at certain wavelengths. Furthermore, it was shown that the fitting algorithm was able to approximate the water+fat content of the phantoms relatively well, but more importantly, there was a correlation between the actual and fitted water+fat content. If a DRS system would be integrated in the drill tip of a surgical drill, the spectral shape as well as the fitted water+fat value could thus be used to estimate the location of the drill tip inside the phantom. However, in order to use the fitted water+fat content parameter for tissue identification, the fitting algorithm should be able to fit the standardized absorption curve of the ABS structural matrix material as well. Currently, this is not the case because the fitting algorithm is only designed for real tissues. For this reason, the water+fat content inside the integrated phantom cannot be evaluated at this point. Despite this, the raw spectra at various measurement depths can be evaluated, which will be done in this chapter.

The optical part of the integrated test setup consisted of the previously mentioned DRS device, an assembly structure made out of profiles, the drill mentioned previously for the drill test, and a microstage (XR25C, Thorlabs Inc., Newton, New Jersey, United States). First, the DRS device was calibrated. The drill was inserted into the phantom, starting from the top with a 50% infill density, and ending at the bottom with a 100% infill density. An initial hole of 3 mm deep was drilled in the samples without taking any measurements to avoid errors due to undesired external light. After that, the drill was retracted from the hole and the optical probe was inserted to take the first DRS measurement. This routine was repeated for every 0.5 mm till 14.5 mm depth was reached. Ten DRS measurements were taken at each measurement depth and in total, spectra at 24 different locations were measured. The ten measurements of each measurement location were averaged and normalized to a wavelength of 1187 nm, which is equal to the location of one of the silicone absorption peaks. One hole was drilled in each test sample. The test setup is depicted in Figure 6.1.

The test setup of the structural part of the integrated test was exactly the same as the previously discussed test setup of the preliminary drill test. In total 5 holes were drilled in the two test samples to obtain the drill characteristics of the integrated phantom.

6.2 Results

Figure 6.2 shows a plot of the raw spectra of subsequent DRS measurements in the integrated test samples and one DRS measurement of the Xanthan gum pure hybrid optical filler, for each of the two holes. The color of the graphs is assigned based on the measurement depth of the signal, with the darkest graph being the first measurement at 3 mm depth and the brightest graph being the last measurement at 14.5 mm depth.

Firstly, compared to the obtained reflectance signals of the pure optical filler samples discussed in Chapter 5, we can conclude that the most dominant reflectance dips around 1200 nm,

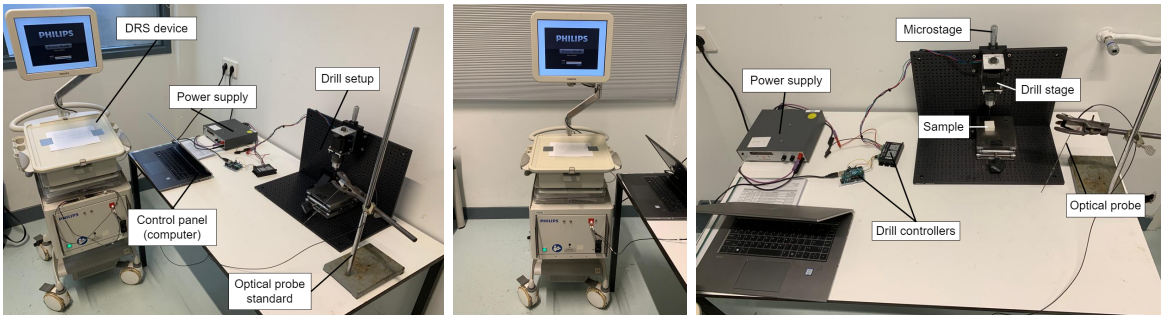

(a) (b) (c)

Figure 6.1: Pictures of the integrated test setup. In the left picture the entire test setup is depicted with the DRS device on the left of the picture and the drill setup on the right of the picture. The middle picture is a closeup of the DRS device. The right picture is a closeup of the drill setup.

1400 nm and 1700 nm are present in both graphs. The spectra obtained in the integrated test display an additional reflectance dip around 1120 nm. When comparing the measured reflectance spectra with the standardized spectral shape of the absorption of water, fat, and silicone, we see that around a wavelength of 1453 nm there is a large dip in the reflectance spectra that coincides with the absorption peak of water. Furthermore, it can be clearly seen that the dip just over 1200 nm is larger for spectra obtained at a large measurement depth. It also seems like the dip just before 1700 nm is larger for measurements obtained at a large measurement depth.

At various wavelengths in Figures 6.2a and c we can see a trend in the graphs. For example, around 1250 nm, around 1450 nm, and just before 1700 nm, the graphs seem to be neatly ordered according to measurement depth. To investigate this trend statistically, effort was put in finding a parameter that showed a significant relation between the measurement depth and the resulting DRS signal. By trial and error, it was found that the parameter of the intensity of the signal at 1203 nm showed this relation statistically. The intensity of the reflectance signal of the measurements at 1203 nm as a function of the measurement depth is depicted in Figures 6.2b and d. A linear fit was applied to the data points, of which the formula and the coefficient of determination (R^2) is shown in the plots as well.

The structural part of the integrated test consists of a graph that shows the axial force on the drill as a function of time. In total, five of such graphs were constructed, obtained from five drilled holes. One example of such a graph is depicted in Figure 6.3. The remainder of the graphs can be found in Appendix D.

From this figure, we can conclude that the graph looks very similar to the previously obtained graphs in the preliminary tests. The axial force on the drill fluctuates in the porous cancellous bone and experiences a large peak in the solid cortical bone. The axial force range in the cancellous bone stays relatively constant in the phantom with cancellous infill density of 50% to 70%, and begins to increase for higher infill densities.

The force range in the cancellous part of the bone (with 50% infill density) is 0.0-7.9 N. The average force in the cancellous core of the phantom with 50% infill density of all five measurements was 4.2 N, and the average peak force in the phantom part with 100% infill

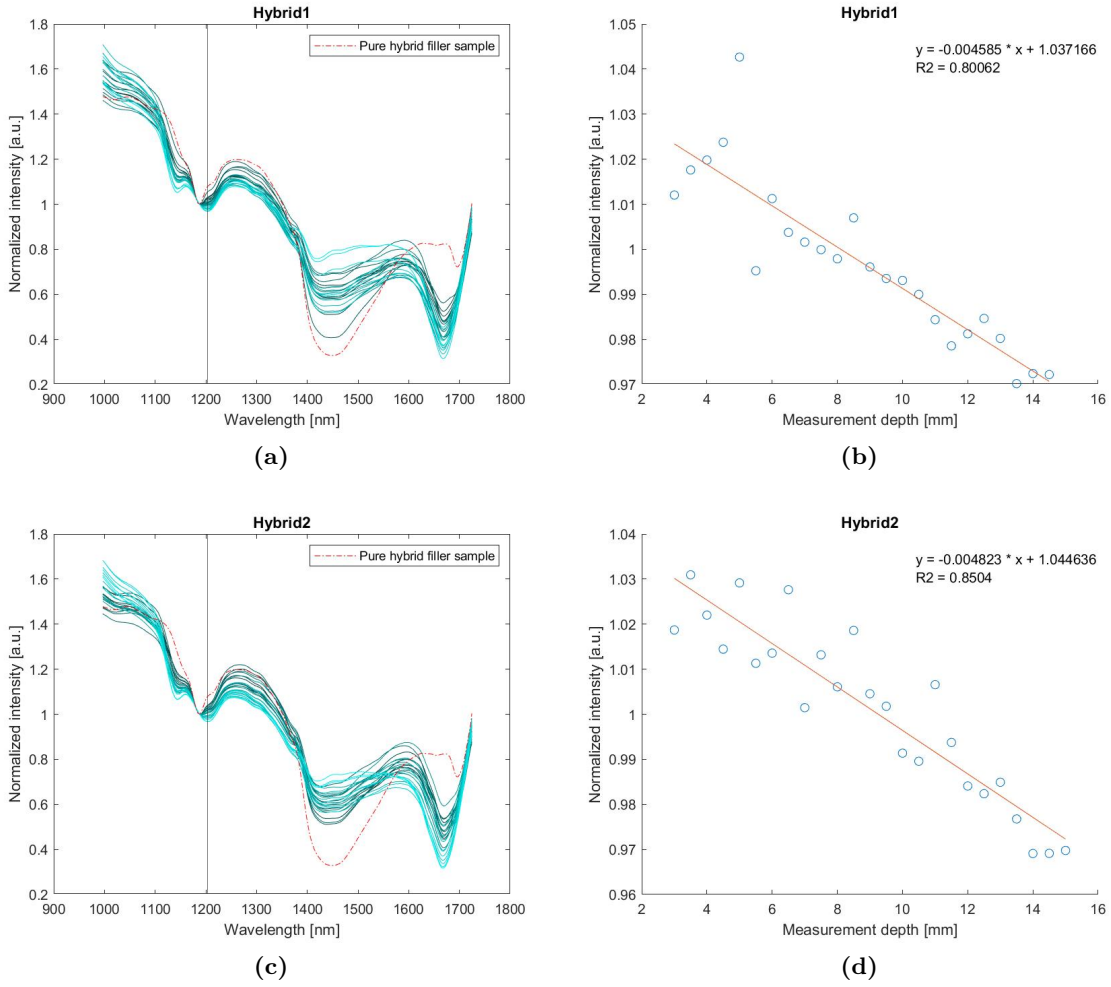

Figure 6.2: Figures a and c are raw spectra of at various measurement depths in a test sample with ABS 50% gyroid infill density in the core, a structural gradient towards the outside of the phantom, and a hybrid optical filler with 50% water+fat content, a FF of 40%, and 1 wt% Xanthan gum as a natural emulsifier. Figures b and d show the absolute reflectance intensity of the raw spectra at 1203 nm as a function of measurement depth.

was 75.7 N. When comparing these values with the values obtained during the preliminary drill test of a phantom with 50% infill density, the average force in the cancellous core is approximately the same (4.6 N vs 4.2 N), but the peak force is much higher, namely 21.2 N for the preliminary test vs 75.7 N for the integrated test.

6.3 Conclusions

In order to obtain an integrated bone phantom, the optical filler should be infused into the structural matrix by covering the structural matrix with liquid optical filler and placing it in a vacuum chamber for at least 40 minutes. The optical filler should be produced with a natural emulsifier and gelling agent that is soluble in cold water, like Xanthan gum (for which

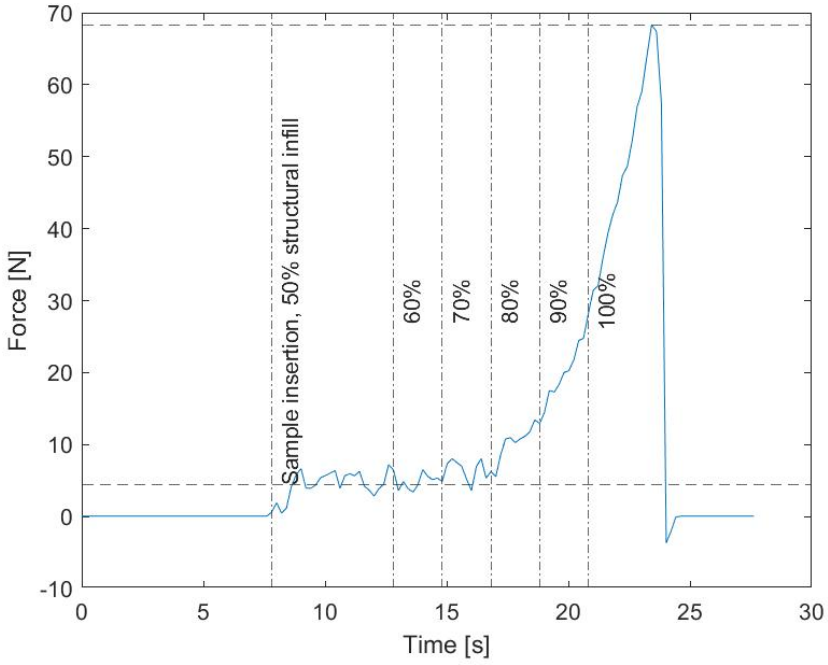

Figure 6.3: Axial drill force over time of one drilled hole in a sample with ABS 50% gyroid infill density in the core, a structural gradient towards the outside of the phantom, and a hybrid optical filler with 50% water+fat content, a FF of 40%, and 1 wt% Xanthan gum as a natural emulsifier. In the figure, the mean force in the 50% infill core of the phantom is indicated with a horizontal dotted line, as well as the peak force in the cortical part of the phantom. On top of that, vertical dotted lines indicate a step increase in infill density.

feasibility was proven with 1 wt%).

Since a structural gradient is incorporated in the printed matrix, the composition of the bone phantom changes and the measured DRS signal should change shape as well with increasing measurement depth. As mentioned before, the spectra are normalized to 1187 nm, which coincides with the location of the silicone absorption peak. The silicone content is higher at lower depths, which means that the dip at 1187 nm should be bigger, and as a result, the slope of the dip is steeper. When normalizing to this wavelength, the reflectance intensity right before and right after the normalization wavelength should thus be higher for lower depths. This is what can be seen in Figure 6.2a and c, and the statistical substantiation is depicted in Figures 6.2c and d. Because R^2 is above 0.8 for both measurements, it can be concluded that the relation between reflectance intensity at 1203 nm and the measurement depth is statistically significant. Because there is a significant relationship between the DRS measurement and the depth of measurement, one can conclude that the phantom is designed in such a way that a DRS system can theoretically be used to identity the location inside the phantom. If the fitting algorithm would be adjusted such that ABS can be fitted as well, the relationship between fitted values and measurement depth should theoretically also be visible in the results.

A force increase with increasing bone density can be seen for measurements in the phantom with 80% infill density and higher. This structural gradient has been demonstrated before when drilling from bone marrow towards the cortical bone shell [53,55]. The mean axial force in the cancellous core of the phantom is approximately the same as the the force measured in the same structure during the preliminary drill test, namely 4.2 N vs 4.6 N, which demonstrates the reproducibility of the drill test results. Compared to the target value of 6 N, the mean force in the cancellous bone of the phantom is slightly lower, which is an indication that the infill density of the core can be further optimized (increased slightly).

It should be noted that the peak force measured during the integrated test was three orders of magnitude higher than the peak force measured during the preliminary drill test. This is a logical result because the drill feed rate, the rotation speed, and the drill bit diameter stayed the same, but the amount of material that must be removed from the hole in the same amount of time increased due to the additional structural gradient. Because the total material volume to be removed increased, the total energy required to drill the hole increases, which is reflected in the axial force on the drill.

Because more material is removed during drilling, more chips are formed. On top of this, there is less space to remove the chips from the hole because the surrounding material is more dense. Because of that, the risk increases that chips accumulate in the the hole and the friction force experienced by the drill increases as well. Due to a higher friction force, the axial peak force might be increased as well.

Because the tested pre-cortical zone had a thickness of 8 mm in stead of the target thickness of 3 mm, the peak cortical bone force in a phantom with a 3 mm thick pre-cortizal zone is expected to be lower than the 75.7 N measured during the integrated test. The target peak cortical force was set to at least 30 N, so to validate this requirement, a different integrated sample with a 3 mm pre-cortical zone should be tested. It is expected that the peak cortical force will then lie between the values of the preliminary test (21.2 N, not containing any pre-cortical zone) and the integrated test (75.7 N, containing a 8 mm thick pre-cortical zone).

Chapter 7

Discussion

7.1 Highlighted results

Even though multiple publications mention the inability to mix plastics with water and fat, this study proved successful fabrication of optical samples containing silicone, water, and fat with a water+fat content of 50% and a FF of 40%. The optical samples had an increased optical stability and preservability of at least 10 weeks compared to simple water/fat hydrogel phantoms [82, 86, 90–92].

One element of this research was to design a stable optical phantom with a specified fat fraction because this parameter has proven its feasibility for tissue identification in previous research [8, 14, 28, 68, 70]. It was concluded that the fitting algorithm that was developed to determine, amongst other things, the FF of tissues from diffusely reflected light spectra for tissue identification was not compatible with the synthetic optical phantoms tested in this study.

However, the fitting algorithm succeeded in approximating the correct relative water+fat content of the optical samples from DRS measurements. The summarized data show a positive correlation between actual water+fat content and fitted water+fat content of the samples. When looking into the water+fat content of cortical and cancellous bone, the conclusion can be drawn that the two bone types can theoretically be distinguished from each other by means of their water+fat content, because the average content for cortical bone is much lower than that of cancellous bone (23.5% and 58.3% respectively) [24, 27]. Therefore, this total water+fat content parameter shows great potential for the use of the DRS-based fitting algorithm for synthetic bone applications.

On top of that, the results of the integrated test consisted of graphs that show that the measured DRS spectra can be used to identity the type of tissue by analyzing the shape of the raw spectra and the relative reflectance intensity between the graphs. As the porosity of the core material decreased, the spectral shape transformed which resulted in a statistically significant relation between the reflectance intensity at 1203 nm for normalized spectra at

1187 nm, and the measurement depth. This indicates great potential for future application in combination with (phantom-adjusted) DRS sensing systems.

The preliminary structural tests and integrated test showed that an Ultimaker 3 printer is the best available 3D printer for the fabrication of the highly detailed porous structural matrix and that the input model should be generated in the Cura slicing software. A structural sample with a gyroid infill density of 50% and a solid printed cortical shell provides a similar drilling environment as previously reported, and the results are repeatable [34]. An infill density of 50% best approximates the drill targets for healthy cancellous bone, and the infill density for osteoporotic bone should be investigated for values below 40%. The stiffness and strength of the structural sample with 50% gyroid infill were significantly higher than the set targets, although they fall within the range of measured E-Modulus and ultimate strength values reported for bone material [23, 30, 32]. A structural gradient is visible in the force measurement as a gradual force increase towards the dense bone phantom, which was reported in previous research as well [53, 55].

7.2 Functional requirement validation

Because of the chosen structural matrix manufacturing method (3D printing), the dimensional design is very flexible, such that any desired shape and outer dimensions can be chosen. This ensures that Requirements 1.1 and 1.2 are met. The cost of the phantom consists of initial costs (lab equipment, 3D printer, and vacuum chamber purchase cost), and material costs. When only considering the material costs, the expenses of, for example, a vertebral model like the one depicted in Figure 7.1 (which will be discussed in detail in the next section) can be broken down in filament cost, which is 2.60 for 52 grams of ABS filament (including supports) and €0.45 for approximately 15 g of the optical filler (including a safety margin of 3). Furthermore, the optical filler is enhanced with sodium benzoate, oil-soluble surfactant, and water-soluble surfactant, which all cost less than €0.01 in such small quantities. This results in a total phantom cost of €3.05, which is well within the target value of €1878, and even significantly below, which means that Requirement 1.3 is met. Each phantom design can be produced with simple lab equipment, a 3D printer and a vacuum chamber. Since all of these device do not require extremely high initial cost or extensive knowledge and expertise to handle, it is concluded that the phantom manufacturability is easy and thus Requirement 1.4 is met. Requirement 1.5 was also met because the integrated phantom was exposed to a temperature of 55°C for 5 minutes, and did not show any signs of change.

It was concluded that the estimated FF values from the fitting algorithm were not accurate for optical phantoms enhanced with silicone. Because of this, Requirements 2.1 and 2.2 were not met. However, it was shown that there exists a good correlation between the relative actual and estimated water+fat content of the silicone-enhanced samples. Human cortical bone contains significantly less water+fat than cancellous bone, namely 23.5% compared to 58.3% as reported by Sierpowska et al. [27] and Carter et al. [24]. This is an indication that the estimated total water+fat content, which is also an output of the fitting algorithm, can be used as a tissue identification parameter in stead of the FF. Unfortunately, the spectra of the integrated bone phantom could not be inserted into the fitting algorithm because the integrated phantom consisted partly out of ABS which is not implemented in the algorithm,

and thus resulted in strongly deviating fitted outcomes. Therefore, the potential of the water+fat content is large, but concrete optical requirements could not be assessed yet. This theory that the estimated water+fat content can be used as a tissue differentiation parameter is reinforced by the fact that the raw spectra of the integrated part gradually changed shape with increasing probe insertion depth and thus with a decrease in water+fat content. This gradual change in spectrum shape was validated by plotting the reflectance intensity at 1203 nm as a function of measurement depth, which resulted in a significant correlation. It was therefore shown that Requirement 2.3 was met. The optical stability and preservability of the integrated phantom was validated by visual inspection and DRS signal comparison in week 0 as well as week 10. The optical samples that were enhanced with silicone and mixed well, showed no signs of deterioration due to bacterial growth or dehydration. Furthermore, there was no structural trend between the DRS signals obtained in week 0 and in week 10 which is an indication that the difference in measured spectra was not due to the elapsed time, but rather due to other errors induced by for example varying measurement conditions. Therefore, Requirement 2.4 was met.

The drill force in the cancellous bone of the phantom fluctuates between 0-7.9 N which means that the target force range of 0-10.0 for healthy bone was simulated closely. Furthermore, the mean force in the cancellous bone of the phantom was 4.2 N which is lower than the mean target force of 6 N for healthy bone, but still in the same order of magnitude. Lastly, the mean peak force in the cortical bone of the phantom is 75.7 N, which is higher than the minimum target peak force of 30 N. This means that Requirements 3.1 and 3.2 are both met for healthy bone. It should be noted however, that the peak force in the cortical bone is affected by the thickness of the pre-cortical zone, which was thicker (8 mm) than the goal pre-cortical zone thickness (3 mm). For osteoporotic bone, an infill density that resulted in well approximated targets was not found because all in all samples the measured force was too large.

The stiffness and strength of the cancellous bone phantom material were higher than the target values, namely 94.5 MPa target vs 237.4 MPa measured and 2.0 MPa target vs 7.0 MPa measured respectively. This means that Requirements 3.3 and 3.4 were not met. The choice was made to prioritize the drill characteristics in stead of the compression characteristics because drilling represents the PSF procedure better, and therefore, not meeting these two requirements is insurmountable.

The core of the phantom consists of a gyroid microstructure that mimics the porous cancellous bone. The pore size of the gyroid structure falls within the target range and thus Requirement 3.5 is met. Requirement 3.6 states that there should be a structural gradient at between the cancellous bone and cortical bone material, in which the density of the bone increases, the axial drill force increases, and the pore size decreases to 0 mm. The model of the structural matrix of the integrated phantom contained an 8 mm thick pre-cortical zone with a step-wise increase in infill density from 50% to 100% (which equals an increase in BVF and apparent density, as well). Furthermore, there was a force increased measured in this pre-cortical zone of the integrated phantom, after drilling through the cancellous bone phantom material (50% infill density) and before the cortical bone phantom material (100% infill density). Because of these reasons, Requirement 3.6 was met.

7.3 Impact

This report started off with spinal disorders, pedicle screw fixation, and drawbacks of this stabilization technique. Although the stable, reliable, flexible, and reproducible bone phantom design discussed in this report is not yet fully validated, positive preliminary results open new doors to shorter medical device development and approval processes, more objective and reliable surgical device assessment, and easier surgical staff training. The increased stability of the optical part of the phantom reduces preserving complications and measurement errors. The combination of an optical filler and a bone structure is not currently on the market although optical-assisted devices are emerging in a fast pace. The integration of optics and material science reduces the complexity and required time for optical guided surgical drill device testing.

An example of a future final phantom design and its functions is depicted in Figure 7.1. This example shows the bone phantom application for testing the guided steerable surgical drill for PSF. The phantom has the shape of an L5 vertebra, obtained from a CT scan, but could be adjusted to any shape (thoracic vertebra, half a vertebra ect). The core is a gyroid structure with the desired infill density. For example, the infill density would be 50% in the aim is to mimic healthy bone. The cavities of the structural matrix are filled using a vacuum chamber with a silicone/water/fat mixture containing for example 50% silicone, and 50% water+fat with a FF of 40%. The cortical shell surrounds the porous core and the thickness can be varied along per location, for to assign a different thickness to the cortical thickness of the pedicle in the ML direction and in the AP direction. Lastly, the phantom contains a pre-cortical zone with a specified thickness and a gradient, in which the infill density changes from the core towards the cortical shell.

The results obtained in this study are not only applicable to PSF, but can be implemented in other orthopedic fields as well. They provide a basis for custom phantom design, tailored to the needs of a broad range of orthopedic applications. Based on the requirements of the bone phantom in question and the different types of samples investigated, the desired optical characteristics and structural characteristics can be selected. These design choices can then be implemented in an integrated design with custom shape and outer dimensions. In this manner, the current project not only provides a phantom design for PSF applications, but the results can be used as a phantom design tool and manufacturing guide.

Next to orthopedic applications, the optical filler described in this report could be adapted for soft tissue phantom design as well. Currently, the most commonly used optical phantoms consist of hydrogels that are very susceptible to deterioration due to bacterial growth and dehydration. A very promising alternative to these unstable optical phantoms could be a phantom containing not only water, fat, and an emulsifier, but also silicone, like the optical filler samples described in this research.

7.4 Limitations and recommendations

Generally, the fitting results that were generated by the fitting algorithm depend heavily on the assumptions made about scattering parameters based on the analytical Farrell model [79], namely the reduced scattering amplitude at the reference wavelength (S800), the Mie scattering slope (b), and the Mie-to-total reduced scattering fraction (Fmie) [8]. In previous studies,

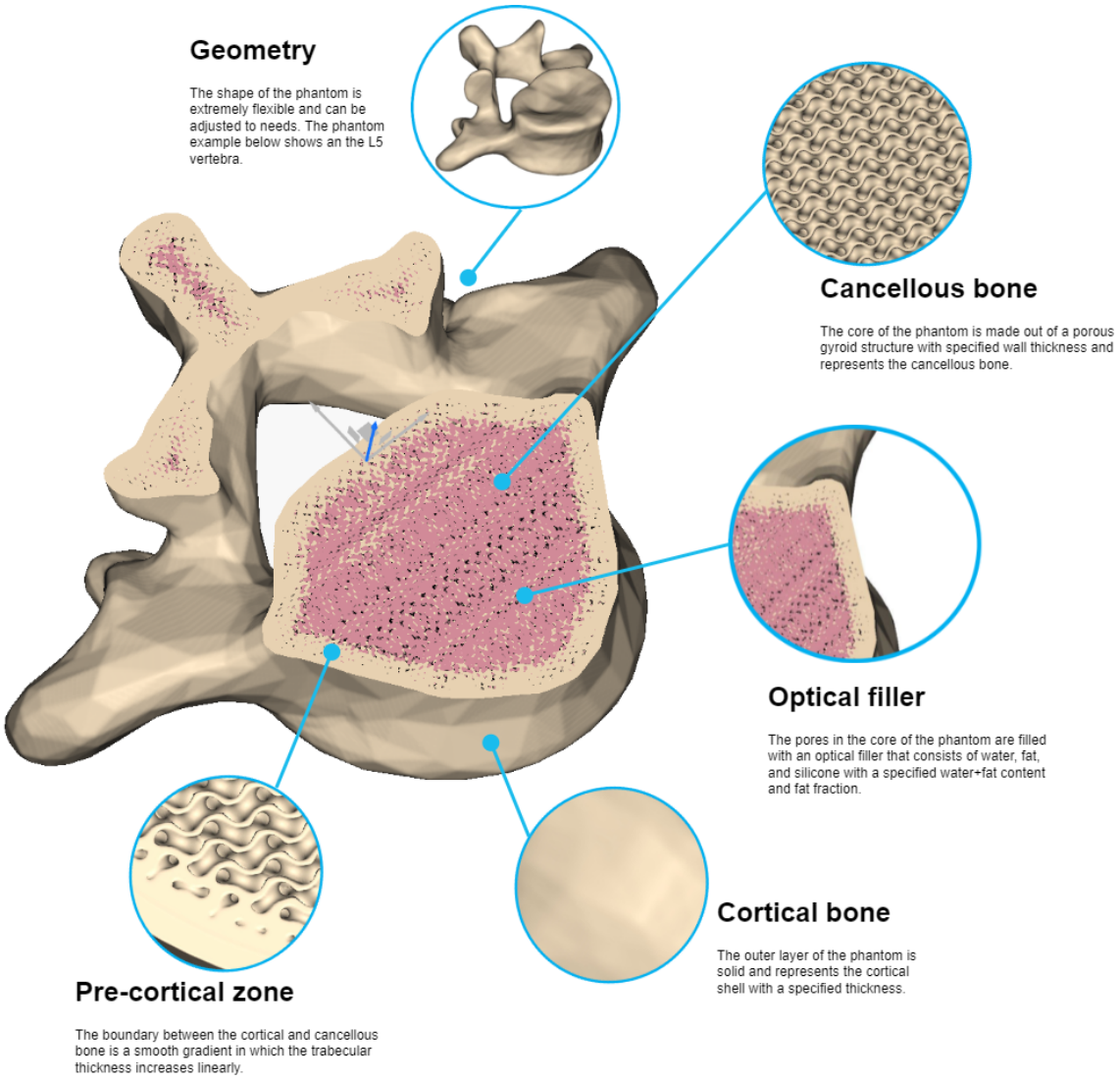

Figure 7.1: Figure of an example phantom for combined DRS and structural testing. The model represents an L5 vertebra with a hybrid optical filler and a cancellous bone core.

it was concluded that the scattering values that were known to be correct, were only correct for specific real soft human tissue, and that synthetic phantoms have completely different scattering values. The values of these scattering parameters for the optical filler samples were determined by trial and error, by matching the fitting output of DRS measurements on pure water and fat phantoms with the actual content of the phantom. Because the scattering parameter estimations were based on only a limited number of measurements, it is unknown if these parameters are correct and thus are at the global minimum of the optimization, or if they result from a local minimum.

As the fitting algorithm is based on the Farrell model equations [79], one of the conditions for using this model is that the scattering distance (the distance between the emitting and collecting optical fiber) is big enough in order for the assumptions of the model equations to hold. During previous tests, is was concluded that errors were induced in the results with a fiber distance of around 1 mm. Since the fiber distance used in these tests was 1.22 mm, it could be that the fitting results contained such errors.

The initial idea was to use the difference in FF between cortical and cancellous bone to identify the tissue boundary because this parameter has proven its feasibility in previous research [8, 14,22,28,68,70]. Although papers were found that report a significant difference in water+fat content between cortical and cancellous bone, a feasibility study on the implementation of this parameter in a DRS-based boundary detection system was never performed. Therefore, if the water+fat parameter resulting from the fitting algorithm is going to be used to detect the boundary between cortical and cancellous bone, such a feasibility study should be carried out on beforehand. In this manner the effect of unknown factors such as large inter-patient differences in water+fat content can be investigated.

Although the fitted water+fat content showed a positive correlation with the actual water+fat content, the variability of the results of some samples was large. It should be investigated if this variability originates from measurement errors, phantom inhomogeneity or another factor. Because the phantom is designed, amongst other things, for comparing novel medical devices with each other, the results should be consistent and reproducible with a small variability. One of the possible explanations for a large variability in the results is the uncontrolled tip pressure on the DRS probe during testing. Although research by Swamy et al. [70] showed no significant error in the fitted FF due to probe handling conditions, it is known that the pressure on the DRS probe tip influences the collected DRS signal. A revised measurement setup with controllable probe tip pressure could remove this unknown parameter from the obtained data, such that the influence of the pressure on the DRS measurements can be investigated.

As discussed in Chapter 6, the fitting algorithm cannot be used on the integrated phantom at this point. The reason for this is that the fitting algorithm is developed for fitting real tissue constituents and therefore, ABS is not yet implemented in the algorithm. If an ABS structural matrix and silicone/water/fat optical filler is going to be used in combination with the fitting algorithm, ABS should be added to the material library of the fitting algorithm. Only after implementation, the accuracy of the water+fat content approximation of the integrated phantom can be estimated again. In this research, the fat in the optical filler part of the phantom was peanut oil. The fat that is being fitting by the algorithm is based on real human fat with a slightly different absorption spectrum. This difference in spectrum

might induce fitting errors. To eliminate these errors, the absorption spectrum of peanut oil should be implemented as well. The same holds for silicone, as the silicone that is being fitted is based on a standard silicone absorption spectrum, without known material characteristics and origin.

On top of that, the working principle of the fitting algorithm relies on a priori knowledge about the approximated sample composition. It was concluded that the fitting outcomes for the pure water/fat phantoms only closely resembled the actual values if the additional silicone chromophore was turned off in the fitting algorithm. This means that the fitting algorithm can only be used once the main components in the tissue or phantom are known already, and that it should be adjusted manually if different tissues and phantoms are compared.

Due to infusion problems, a different emulsifier (Xanthan gum) was used for the integrated test, than for the preliminary tests. The assumption was made that, as long as the water fraction, FF, and silicone fraction stayed the same, and the hybrid filler well mixed, the absorption, optical stability, and preservability characteristics of the filler were not significantly different compared to the previously evaluated optical filler with agar agar. This should however be confirmed.

The material characteristics of a phantom that mimics osteoporotic bone should be investigated in more detail. Unfortunately, with the test samples for healthy bone, no good match with osteoporotic targets was found because all infill densities were too high. What can be concluded is that samples with an infill density lower than 40% should be evaluated for osteoporotic bone phantoms.

The target structural gradient in the pre-cortical zone of 3 mm thickness was not validated because in the integrated test, for visualization purposes, the pre-cortical zone thickness was set to 8 mm. This means that Requirement 3.6 is not met for this test phantom. However, since 3D printing allows for extremely flexible design, the structural gradient can be adjust very easily and the goal structural gradient can be accomplished. In the future, a phantom design with the correct structural pre-cortical zone thickness of 3 mm should be validated.

The bone phantom design discussed in this report consists of a 3D printed ABS structural matrix with an infused optical filler made out of mainly water, fat, and silicone. The phantom is unique because it combines both the optical and structural characteristics of bone, which has not been reported before. Furthermore, this report contains all the relevant information for anyone to compose a custom bone phantom with desired optical and structural characteristics, and thus serves as a design tool. Lastly, it was proven that the production a soft optical phantom containing water, fat, and silicone is feasible and that such a phantom has an increased stability and preservability compared to classic hydrogel soft tissue phantoms, which opens new doors for soft tissue phantom design.

References

[1] The spinal cord | Human Anatomy and Physiology Lab (BSB 141). Lumen Learning. Retrieved from: https://courses.lumenlearning.com/ap1x94x1/chapter/the-spinal-cord/ on 09/07/21.

[2] Ullrich, P. F. Spinal Anatomy and Back Pain. (2011) Retrieved from: https://centerforspineandortho.com/news/spinal-anatomy-and-back-pain/ on 02/11/2021.

[3] Klenerman, L. (2015) Human Anatomy.

[4] Panjabi, M. M., Shin, E. K., Chen, N. C., and Wang, J. L. (2000) Internal morphology of human cervical pedicles. *Spine,* **25**(10), 1197–1205.

[5] Cancellous bone. (September, 2021) Laboratoires Sevier. Retrieved from: https://commons.wikimedia.org/wiki/File:Spongy_bone_-_Trabecular_bone_2_--_Smart-Servier.png on 08/07/2021.

[6] McAlpin, C. Preparing for spinal fusion surgery is a team effort. (2020) Retrieved from: https://mayfieldclinicblog.com/?p=5610 on 06/07/21.

[7] Mirza, S. K., Wiggins, G. C., Kuntz IV, C., York, J. E., Bellabarba, C., Knonodi, M. A., Chapman, J. R., and Shaffrey, C. I. (2003) Accuracy of thoracic vertebral body screw placement using standard fluoroscopy, fluoroscopic image guidance, and computed tomographic image guidance: A cadaver study. *Spine,* **28**(4), 402–413.

[8] Burström, G., Swamy, A., Spliethoff, J. W., Reich, C., Babic, D., Hendriks, B. H. W., Skulason, H., Persson, O., Elmi Terander, A., and Edström, E. (2019) Diffuse reflectance spectroscopy accurately identifies the pre-cortical zone to avoid impending pedicle screw breach in spinal fixation surgery. *Biomedical Optics Express,* **10**(11), 5905.

[9] De Kater, E. NWO – Spine Stabilization. (2020) Retrieved from: https://www.bitegroup.nl/research-projects/steerable-bone-drill/ on 10/11/21.

[10] Sawbones. Retrieved from: https://www.sawbones.com on 04/12/2021.

[11] Synbone. Retrieved from: https://www.synbone.com on 03/12/2021.

[12] Barak, M. M. and Black, M. A. (feb, 2018) A novel use of 3D printing model demonstrates the effects of deteriorated trabecular bone structure on bone stiffness and strength. *Journal of the Mechanical Behavior of Biomedical Materials,* **78**, 455–464.

[13] Weisstein, E. W. Gyroid. Retrieved from: MathWorld–A Wolfram Web Resource. https://mathworld.wolfram.com/Gyroid.html on 23/12/21.

[14] Swamy, A., Burström, G., Spliethoff, J. W., Babic, D., Reich, C., Groen, J., Edström, E., Elmi Terander, A., Racadio, J. M., Dankelman, J., and Hendriks, B. H. W. (2019) Diffuse reflectance spectroscopy, a potential optical sensing technology for the detection of cortical breaches during spinal screw placement. *Journal of Biomedical Optics,* **24**(01), 1.

[15] Epolin. Retrieved from: https://www.epolin.com/epolin_product/nir-and-visible-absorbing-dyes-thermoplastics/ on 26/08/2021.

[16] Vertebrae of the spine. (2021) The StayWell Company. Retrieved from: https://www.cedars-sinai.org/health-library/diseases-and-conditions/v/vertebrae-of-the-spine.html on 09/07/21.

[17] Maclaughlin, S. M. and Oldal, K. N. M. (1992) Vertebral body diameters and sex prediction. *Annuals of Human Biology,* **19**(3), 285–292.

[18] Urrutia Vega, E., Elizondo Omaña, R. E., de la Garza Castro, O., and Guzmán López, S. (2009) Morfometría del cuerpo vertebral y pedículo en una población mexicana mediante TC y fluoroscopía. *International Journal of Morphology,* **27**(4), 1299–1303.

[19] Ritzel, H., Amling, M., Pösl, M., Hahn, M., and Delling, G. (jan, 1997) The Thickness of Human Vertebral Cortical Bone and its Changes in Aging and Osteoporosis: A Histomorphometric Analysis of the Complete Spinal Column from Thirty-Seven Autopsy Specimens. *Journal of Bone and Mineral Research,* **12**(1), 89–95.

[20] Eswaran, S. K., Gupta, A., Adams, M. F., and Keaveny, T. M. (2006) Cortical and Trabecular Load Sharing in the Human Vertebral Body. *Journal of Bone and Mineral Research,* **21**(2), 193–206.

[21] Mosekilde, L. (1993) Vertebral Structure and Strength In Vivo and In Vitro. *Calcified Tissue International,* **53**(Supplement 1), 121–126.

[22] Losch, M. S., Swamy, A., Elmi-Terander, A., Edström, E., Hendriks, B. H., and Dankelman, J. (2021) Proton density fat fraction of the spinal column: an MRI cadaver study. *BioMedical Engineering Online,* **20**(1), 1–11.

[23] Gibson, L. J. (1985) The mechanical behaviour of cancellous bone. *Journal of Biomechanics,* **18**(5), 317–328.

[24] Carter, D. R. and Spengler, D. M. (1978) Mechanical properties and composition of cortical bone. *Clinical Orthopaedics and Related Research,* (135), 192–217.

[25] Roy, M. E., Rho, J.-Y., Tsui, T. Y., Evans, N. D., and Pharr, G. M. (1999) Mechanical and morphological variation of the human lumbar vertebral cortical and trabecular bone. **44**, 191–197.

[26] Nouh, M. R. and Eid, A. F. (2015) Magnetic resonance imaging of the spinal marrow: Basic understanding of the normal marrow pattern and its variant. *World Journal of Radiology,* **7**(12), 448.

[27] Sierpowska, J., Lammi, M. J., Hakulinen, M. A., Jurvelin, J. S., Lappalainen, R., and Töyräs, J. (2007) Effect of human trabecular bone composition on its electrical properties. *Medical Engineering & Physics,* **29**, 845–852.

[28] Swamy, A., Burström, G., Spliethoff, J. W., Babic, D., Ruschke, S., Racadio, J. M., Edström, E., Elmi-Terander, A., Dankelman, J., and Hendriks, B. H. W. (2019) Validation of diffuse reflectance spectroscopy with magnetic resonance imaging for accurate vertebral bone fat fraction quantification. *Biomedical Optics Express,* **10**(8), 4316.

[29] Nicholson, P. H., Cheng, X. G., Lowet, G., Boonen, S., Davie, M. W., Dequeker, J., and Van Der Perre, G. (1997) Structural and material mechanical properties of human vertebral cancellous bone. *Medical Engineering and Physics,* **19**(8), 729–737.

[30] Teo, J. C., Si-Hoe, K. M., Keh, J. E., and Teoh, S. H. (2007) Correlation of cancellous bone microarchitectural parameters from microCT to CT number and bone mechanical properties. *Materials Science and Engineering C,* **27**(2), 333–339.

[31] Mosekilde, L., Mosekilde, L., and Danielsen, C. C. (1987) Biomechanical Competence of Vertebral Trabecular Bone in Relation to Ash Density and Age in Normal Individuals. *Pergamon Journals Ltd. - Bone,* **8**, 79–85.

[32] Morgan, E. F. and Keaveny, T. M. (2001) Dependence of yield strain of human trabecular bone on anatomic site. *Journal of Biomechanics,* **34**, 569–577.

[33] Schileo, E., Dall'Ara, E., Taddei, F., Malandrino, A., Schotkamp, T., Baleani, M., and Viceconti, M. (2008) An accurate estimation of bone density improves the accuracy of subject-specific finite element models. *Journal of biomechanics,* **41**(11), 2483–2491.

[34] Kan, M. P. (2020) Optical performance and drilling forces of an orthopaedic DRS drill with a stagnant optical probe. *Unpublished,*.

[35] Wei, Y., Zheng, X., Yu, D., Dong, D., and Chen, M. (2012) Experimental Study on Drilling Force during Mandible Drilling Process. **723**, 460–465.

[36] Van Drunen, F. (2020) Powered hammering a diffuse reflectance spectroscopy equipped K-wire: Examining insertion control and optical capabilities Powered hammering a diffuse reflectance spectroscopy equipped. *Unpublished,*.

[37] Vaccaro, A. R. and Garfin, S. R. (1995) Pedicle-Screw Fixation in the Lumbar Spine. *Journal of the American Academy of Orthopaedic Surgeons,* **3**(5), 263–274.

[38] Makino, T., Tsukazaki, H., Ukon, Y., Tateiwa, D., Yoshikawa, H., and Kaito, T. (2018) The biological enhancement of spinal fusion for spinal degenerative disease. *International Journal of Molecular Sciences,* **19**(8).

[39] Rajaee, S. S., Bae, H. W., Kanim, L. E., and Delamarter, R. B. (2012) Spinal fusion in the United States: Analysis of trends from 1998 to 2008. *Spine,* **37**(1), 67–76.

[40] Shepard, N., Pham, H., Natarajan, V., Errico, T., and Rieger, M. (2019) Use of a Novel Computerized Drill for Pedicle Screw Insertion in the Thoracic and Lumbar Spine: A Cadaveric Study. *International Journal of Spine Surgery,* **13**(4), 329–335.

[41] Faraj, A. A. and Webb, J. K. (1997) Early complications of spinal pedicle screw. *Eur Spine J,* **6**, 324–326.

[42] Solomiichuk, V., Fleischhammer, J., Molliqaj, G., Warda, J., Alaid, A., von Eckardstein, K., Schaller, K., Tessitore, E., Rohde, V., and Schatlo, B. (2017) Robotic versus fluoroscopy-guided pedicle screw insertion for metastatic spinal disease: A matched-cohort comparison. *Neurosurgical Focus,* **42**(5), 1–7.

[43] Allaoui, M., Zairi, F., Té Tard, M.-C., Gaughan, J., Chopin, D., and Assaker, R. (2018) Contribution of Dynamic Surgical Guidance to the Accurate Placement of Pedicle Screws in Deformity Surgery: A Retrospective Case Series. *World Neurosurg.,* **120**, E466–E471.

[44] Kothe, R., O'Holleran, J., Liu, W., and Panjabi, M. (1996) Internal Architecture of the Thoracic Pedicle: An Anatomic Study. *Spine,* **21**(3), 264–270.

[45] Weinstein, J. N., Rydevik, B. L., and Rauschning, W. (1992) Anatomic and technical considerations of pedicle screw fixation. *Clinical Orthopaedics and Related Research,* (284), 34–46.

[46] Davne, S. H. and Myers, D. L. (1992) Complications of Lumbar Spinal Fusion with Transpedicular Instrumentation.

[47] Upendra, B. N., Meena, D., Chowdhury, B., Ahmad, A., and Jayaswal, A. (2008) Outcome-based classification for assessment of thoracic pedicular screw placement. *Spine,* **33**(4), 384–390.

[48] Matsukawa, K., Taguchi, E., Yato, Y., Imabayashi, H., Hosogane, N., Asazuma, T., and Nemoto, K. (2015) Evaluation of the fixation strength of pedicle screws using cortical bone trajectory: What is the ideal trajectory for optimal fixation?. *Spine,* **40**(15), E873–E878.

[49] Holly, L. T. and Anderson, P. A. (2017) Essentials of spinal stabilization. *Essentials of Spinal Stabilization,* pp. 1–566.

[50] Defino, H. L. A. and Vendrame, J. R. B. (2007) Morphometric study of lumbar vertebrae's pedicle. *Acta Ortopédica Brasileira,* **15**(4), 183–186.

[51] Bourgeois, A. C., Faulkner, A. R., Pasciak, A. S., and Bradley, Y. C. (2015) The evolution of image-guided lumbosacral spine surgery. *Annals of Translational Medicine,* **3**(5), 1–13.

[52] McEwen, D. R. (1996) Intraoperative Positioning of Surgical Patients. *AORN Journal,* **6**(63), 1059–1079.

[53] Bouazza-Marouf, K., Browbank, I., and Hewit, J. R. (1996) Robot-assisted invasive orthopaedic surgery. *Mechatronics,* **6**(4), 381–397.

[54] Duperron, M., Grygoryev, K., Nunan, G., Eason, C., Burke, R., Manley, K., Gunther, J., and O'brien, P. (2019) Diffuse reflectance spectroscopy-enhanced drill for bone boundary detection. *Biomedical Optics Express,* **10**(2).

[55] Hu, Y., Jin, H., Zhang, L., Zhang, P., and Zhang, J. (2014) State recognition of pedicle drilling with force sensing in a robotic spinal surgical system. *IEEE/ASME Transactions on Mechatronics,* **19**(1), 357–365.

[56] Ong, F. R. Analysis of bone drilling characteristics for the enhancement of safety and the evaluation of bone strength. PhD thesis (1998).

[57] Cook, C., Santos, G. C. M., Lima, R., Pietrobon, R., Jacobs, D. O., and Richardson, W. (2007) Geographic variation in lumbar fusion for degenerative disorders: 1990 to 2000. *Spine Journal,* **7**(5), 552–557.

[58] Pan, Z., Zhong, J., Xie, S., Yu, L., Chunyang, W., Ha, Y., Kim, K. N., Zhang, Y., and Cao, K. (2018) Accuracy and Safety of Lateral Vertebral Notch-Referred Technique Used in Subaxial Cervical Pedicle Screw Placement. *Operative Neurosurgery,* **0**(0).

[59] Woo, E. J. and Dicuccio, M. N. (2017) Clinical Study Clinically significant pedicle screw malposition is an underestimated cause of radiculopathy. *The Spine Journal,* **18**, 1166–1171.

[60] Kosmopoulos, V. and Schizas, C. (2007) Pedicle Screw Placement Accuracy: A Meta Analysis. *Spine,* **32**(3), E111–E120.

[61] Schwarzenback, O., Berlemann, U., Jost, B., Visarius, H., Arm, E., Langlotz, F., Nolte, L.-P., and Ozdoba, C. (1997) Accuracy of Computer-Assisted Pedicle Screw Placement: An In Vivo Computed Tomography Analysis. *Spine,* **22**(4), 452–458.

[62] Halvorson, T., Kelley, L., Thomas, K., Whitecloud, T., and Cook, S. (1994) Effects of Bone Mineral Density on Pedicle Screw Fixation. *Spine,* **19**(21), 183–186.

[63] Seebeck, J., Goldhahn, J., Städele, H., Messmer, P., Morlock, M. M., and Schneider, E. (nov, 2004) Effect of cortical thickness and cancellous bone density on the holding strength of internal fixator screws. *Journal of Orthopaedic Research,* **22**(6), 1237–1242.

[64] Van Dijk, J. D., Van Den Ende, R. P., Stramigioli, S., Köchling, M., and Höss, N. (sep, 2015) Clinical pedicle screw accuracy and deviation from planning in robot-guided spine surgery: Robot-guided pedicle screw accuracy. *Spine,* **40**(17), E986–E991.

[65] Liu, K., Zhang, Q., Li, X., Zhao, C., Quan, X., Zhao, R., Chen, Z., and Li, Y. (dec, 2016) Preliminary application of a multi-level 3D printing drill guide template for pedicle screw placement in severe and rigid scoliosis. *European Spine Journal,* **26**(6), 1684–1689.

[66] Van Pelt, T. (2021) Structured overview of spectroscopy sensory techniques for real time tissue distinction. *Unpublished,*.

[67] Bydlon, T. M., Nachabé, R., Ramanujam, N., Sterenborg, H. J., and Hendriks, B. H. (2015) Chromophore based analyses of steady-state diffuse reflectance spectroscopy: Current status and perspectives for clinical adoption. **8**(1-2), 9–24.

[68] Hendriks, B. H. W., Balthasar, A. J. R., Lucassen, G. W., Van Der Voort, M., Mueller, M., Pully, V. V., Bydlon, T. M., Reich, C., Van Keersop, A. T. M. H., Kortsmit, J., Langhout, G. C., and Van Geffen, G.-J. (2015) Nerve detection with optical spectroscopy for regional anesthesia procedures. *Journal of Translational Medicine,* **13**, 380.

[69] Nachabé, R., W Hendriks, B. H., van der Voort, M., Desjardins, A. E., and C M Sterenborg, H. J. (2010) Estimation of biological chromophores using diffuse optical spectroscopy: benefit of extending the UV-VIS wavelength range to include 1000 to 1600 nm. *Optics Express,* **18**(24), 3.

[70] Swamy, A., Spliethoff, J. W., Burström, G., Babic, D., Reich, C., Groen, J., Edström, E., Elmi-Terander, A., Racadio, J. M., Dankelman, J., and Hendriks, B. H. W. (June, 2020) Diffuse reflectance spectroscopy for breach detection during pedicle screw placement: a first in vivo investigation in a porcine model. *BioMedical Engineering OnLine,* **19**(1), 1–12.

[71] Shea, T. M., Laun, J., Gonzalez-Blohm, S. A., Doulgeris, J. J., Lee, W. E., Aghayev, K., and Vrionis, F. D. (2014) Designs and techniques that improve the pullout strength of pedicle screws in osteoporotic vertebrae: Current status. *BioMedical Research International,* **2014**.

[72] Ali, A., Sakes, A., Arkenbout, E. A., Henselmans, P., van Starkenburg, R., Szili-Torok, T., and Breedveld, P. (oct, 2019) Catheter steering in interventional cardiology: Mechanical analysis and novel solution. *Engineering in Medicine,* **233**(12), 1207–1218.

[73] Sakes, A., Ali, A., Janjic, J., and Breedveld, P. (sep, 2018) Novel Miniature Tip Design for Enhancing Dexterity in Minimally Invasive Surgery. *Journal of Medical Devices,* **12**(3).

[74] Scali, M., Kreeft, D., Breedveld, P., and Dodou, D. (apr, 2017) Design and evaluation of a wasp-inspired steerable needle. *Bioinspiration, Biomimetics, and Bioreplication,* **10162**, 1016207.

[75] Scali, M., Pusch, T. P., Breedveld, P., and Dodou, D. (dec, 2017) Ovipositor-inspired steerable needle: design and preliminary experimental evaluation. *Bioinspiration & Biomimetics,* **13**(1), 016006.

[76] Nachabé, R., Hendriks, B. H. W., Desjardins, A. E., van der Voort, M., van der Mark, M. B., and Sterenborg, H. J. C. M. (2010) Estimation of lipid and water concentrations in scattering media with diffuse optical spectroscopy from 900 to 1600 nm. *Journal of Biomedical Optics,* **15**(3), 037015.

[77] Van Veen, R., Sterenborg, H., Pifferi, A., Torricelli, A., and Cubeddu, R. (2004) Determination of VIS- NIR absorption coefficients of mammalian fat, with time- and spatially resolved diffuse reflectance and transmission spectroscopy. *Optical Society of America,*.

[78] Nickell, S., Hermann, M., Essenpreis, M., al, P Doornbos, R. M., Lang, R., Aalders, M. C., Cross, F. W., and C M Sterenborg, H. J. (1999) The determination of in vivo human tissue optical properties and absolute chromophore concentrations using spatially resolved steadystate diffuse reflectance spectroscopy. *Physics in Medicine and Biology,* **44**, 967–981.

[79] Farrell, T. J., Patterson, M. S., and Wilson, B. (1992) A diffuse theory model of spatially resolved, steady-state diffuse reflectance for the noninvasive determination of tissue optical properties in vivo. *Medical Physics,* **19**(4).

[80] Van Norman, G. A. (jun, 2016) Drugs, Devices, and the FDA: Part 2: An Overview of Approval Processes: FDA Approval of Medical Devices. *JACC: Basic to Translational Science,* **1**(4), 277–287.

[81] Burkhard, M., Fürnstahl, P., and Farshad, M. (dec, 2018) Three-dimensionally printed vertebrae with different bone densities for surgical training. *European Spine Journal 2018 28:4,* **28**(4), 798–806.

[82] Pogue, B. W. and Patterson, M. S. (2006) Review of tissue simulating phantoms for optical spectroscopy, imaging and dosimetry. *Journal of Biomedical Optics,* **11**(4), 041102.

[83] Royston, D., Poston, R. S., and Prahl, S. A. (1995) Optical Properties of Scattering and Absorbing Materials Used in the Development of Optical Phantoms at 1064 nm. *Journal of Biomedical Optics,*.

[84] Vernon, M. L., Fréchette, J., Painchaud, Y., Caron, S., and Beaudry, P. (1999) Fabrication and characterization of a solid polyurethane phantom for optical imaging through scattering media. *Applied Optics,* **38**(19), 4247.

[85] Ayers, F., Grant, A., Kuo, D., Cuccia, D. J., and Durkin, A. J. (2008) Fabrication and characterization of silicone-based tissue phantoms with tunable optical properties in the visible and near infrared domain. *Progress in Biomedical Optics and Imaging-Proceedings of SPIE,* **6870**.

[86] Li, P., Yang, Z., and Jiang, S. (2018) Tissue mimicking materials in image-guided needle-based interventions: A review. *Materials Science and Engineering C,* **93**(August), 1116–1131.

[87] Natural Spices. Retrieved from: http://www.naturalspices.com on 11/08/2021.

[88] Sigma Aldrich. Retrieved from: https://www.sigmaaldrich.com/NL/en/product/aldrich/341584?cm_sp=Insite-_-caContent_prodMerch_gruCrossEntropy-_-prodMerch10-3 on 11/08/2021.

[89] Avigo, C., Di Lascio, N., Armanetti, P., Kusmic, C., Cavigli, L., Ratto, F., Meucci, S., Masciullo, C., Cecchini, M., Pini, R., Faita, F., and Menichetti, L. (apr, 2015) Organosilicon phantom for photoacoustic imaging. *Journal of Biomedical Optics,* **20**(4), 046008.

[90] Kennedy, G., Lentsch, G., Trieu, B., Ponticorvo, A., Saager, R. B., and Durkin, A. J. (2017) Design and fabrication of solid phantoms for NIR water fraction studies. **10056**.

[91] Kennedy, G., Lentsch, G., Trieu, B., Ponticorvo, A., Saager, R. B., and Durkin (jul, 2017) Solid tissue simulating phantoms having absorption at 970 nm for diffuse optics. *Journal of Biomedical Optics,* **22**(7), 076013.

[92] Qian, Z., Victor, S. S., Gu, Y., Giller, C. A., and Liu, H. (2003) "Look-Ahead Distance" of a fiber probe used to assist neurosurgery: Phantom and Monte Carlo study. *Optics Express,* **11**(16), 1256–1267.

[93] Bush, E. C., Gifford, A., Coolbaugh, C. L., Towse, T. F., Damon, B. M., and Welch, E. B. (sep, 2018) Fat-water phantoms for magnetic resonance imaging validation: A flexible and scalable protocol. *Journal of Visualized Experiments,* **2018**(139).

[94] Shokoufi, M. and Golnaraghi, F. (mar, 2019) Handheld diffuse optical breast scanner probe for cross-sectional imaging of breast tissue. *Journal of Innovative Optical Health Sciences,* **12**(2).

[95] Avtzi, S., Zacharopoulos, A., Psycharakis, S., and Zacharakis, G. (nov, 2013) Fabrication and characterization of a 3-D non-homogeneous tissue-like mouse phantom for optical imaging. *Biophotonics,* **9032**.

[96] Berg, R., Andersson-Engels, S., Jarlman, O., and Svanberg, S. (1996) Time-gated viewing studies on tissuelike phantoms. *Applied Optics,* **35**(19), 3432.

[97] INO biomimic optical phantoms - FAQ about our phantoms. Retrieved from https://www.ino.ca/en/solutions/biomimic/ on 01/09/2021.

[98] Sternheim, A., Daly, M., Qiu, J., Weersink, R., Chan, H., Jaffray, D., Irish, J. C., Ferguson, P. C., and Wunder, J. S. (2015) Navigated Pelvic Osteotomy and Tumor Resection. *Journal of Bone and Joint Surgery,* **97**(1), 40–46.

[99] Tasinkevych, Y., Falińska, K., Lewin, P. A., and Litniewski, J. (apr, 2019) Improving broadband ultrasound attenuation assessment in cancellous bone by mitigating the influence of cortical bone: Phantom and in-vitro study. **94**, 382–390.

[100] Bohl, M. A., Morgan, C. D., Mooney, M. A., Repp, G. J., Lehrman, J. N., Kelly, B. P., Chang, S. W., Turner, J. D., and Kakarla, U. K. (jan, 2019) Biomechanical Testing of a 3D-printed L5 Vertebral Body Model. *Cureus,* **11**(1).

[101] Ong, F. R. and Bouazza-Marouf, K. (2000) Evaluation of bone strength: correlation between measurements of bone mineral density and drilling force. *Proceeding of the Institution of Mechanical Engineers,* **214**.

[102] Honkala, S., Hämäläinen, M., and Salonen, M. (2007) Comparison of four existing concept selection methods. *Proceedings of ICED 2007, the 16th International Conference on Engineering Design,* **DS 42**(August), 1–11.

[103] Hines, C. D., Yu, H., Shimakawa, A., McKenzie, C. A., Brittain, J. H., and Reeder, S. B. (nov, 2009) T1 independent, T2* corrected MRI with accurate spectral modeling for quantification of fat: Validation in a fat-water-SPIO phantom. *Journal of Magnetic Resonance Imaging,* **30**(5), 1215–1222.

[104] De Boer, L. L., Bydlon, T. M., Van Duijnhoven, F., Vranken Peeters, M.-J. T. F. D., Loo, C. E., Winter-Warnars, G. A. O., Sanders, J., Sterenborg, H. J. C. M., Hendriks, B. H. W., and Ruers, T. J. M. (2018) Towards the use of diffuse reflectance spectroscopy for real-time in vivo detection of breast cancer during surgery. *Journal of Translational Medicine,* **16**, 367.

[105] PLA EP. Technical Data Sheet. Smartfil Smart Materials 3D. Retrieved from: https://www.smartmaterials3d.com/ep-filamento on 15/11/21.

[106] Lee, J. E., Gozen, B. A., and Ozdoganlar, O. B. (2012) Modeling and experimentation of bone drilling forces. *Journal of Biomechanics,* **45**(6), 1076–1083.

[107] Lee, W. Y., Shih, C. L., and Lee, S. T. (2004) Force control and breakthrough detection of a bone-drilling system. *IEEE/ASME Transactions on Mechatronics,* **9**(1), 20–29.

Appendix A

Homogeneity plots

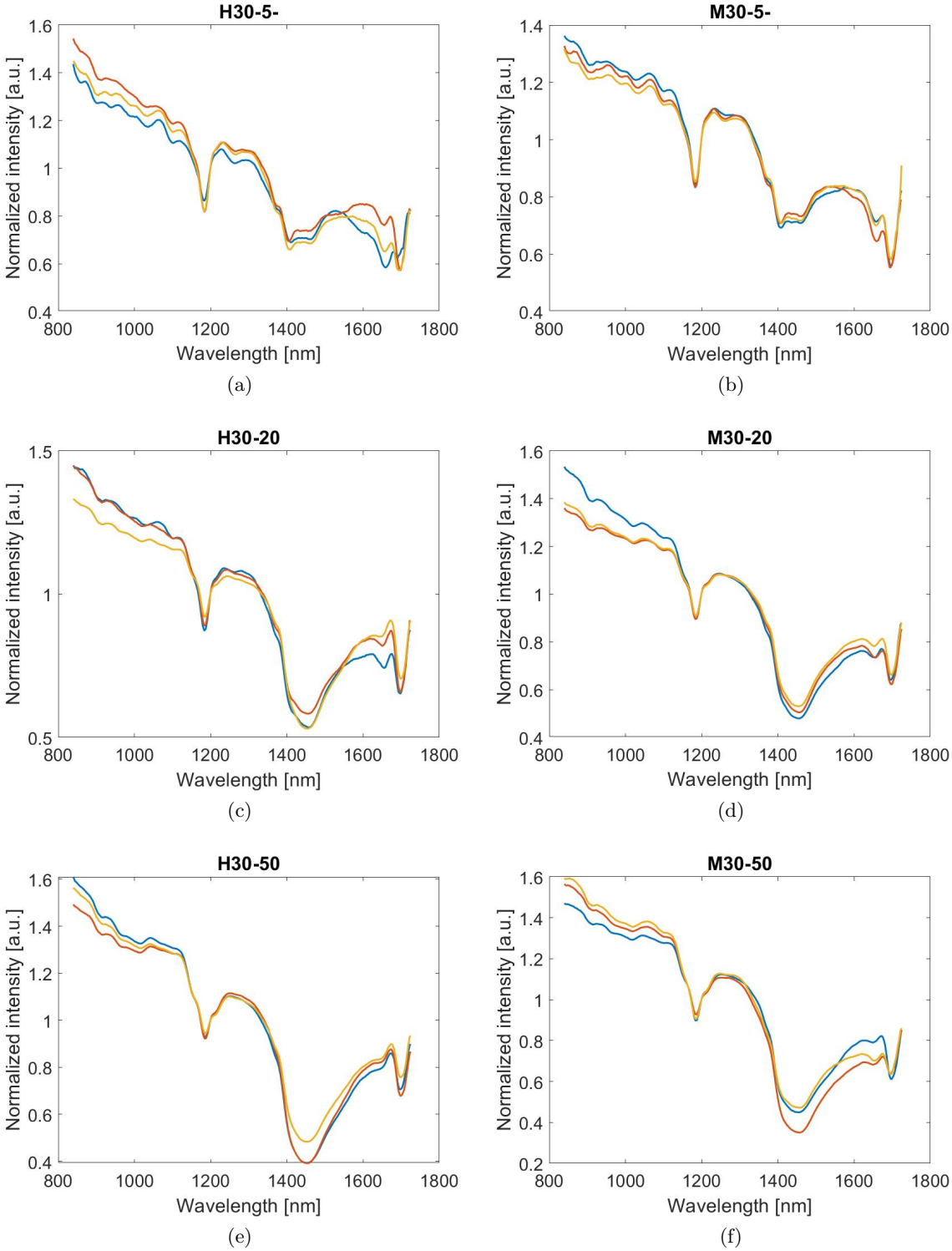

Figure A.1: Averaged raw spectra of three measurement locations per sample

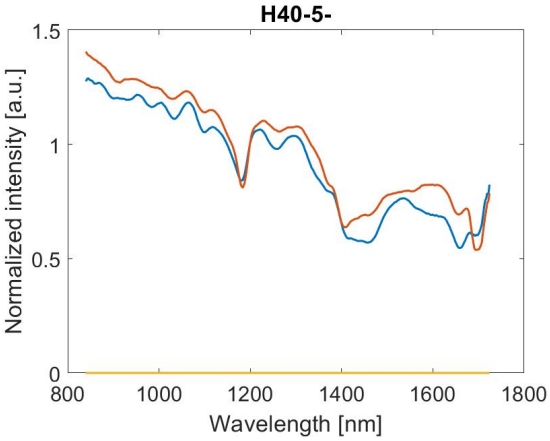

(g)

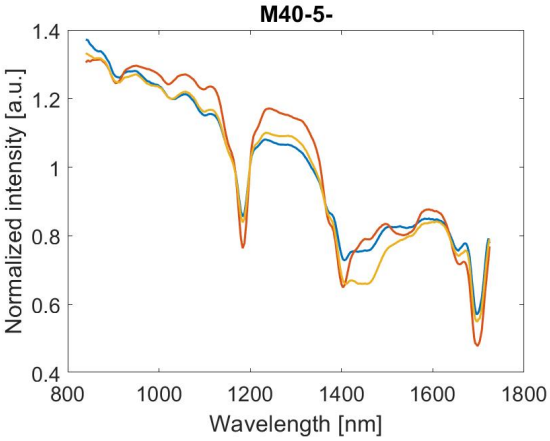

(h)

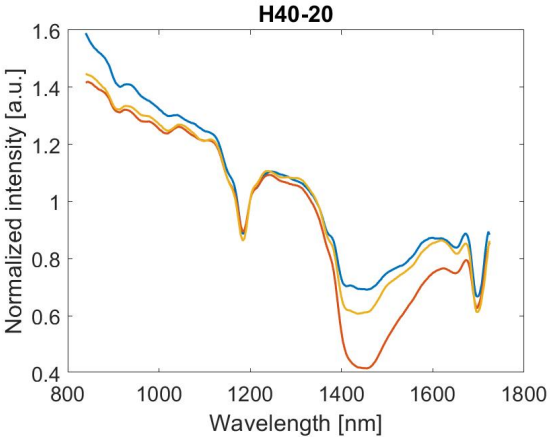

(i)

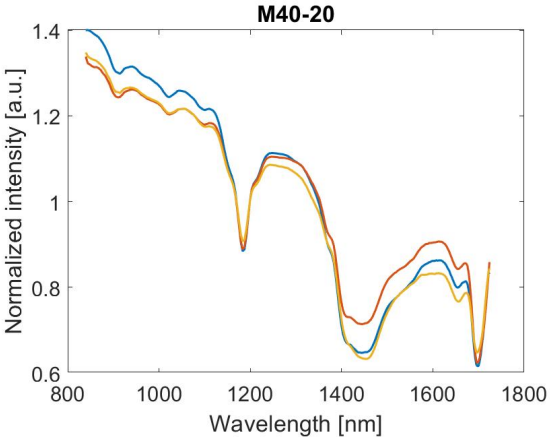

(j)

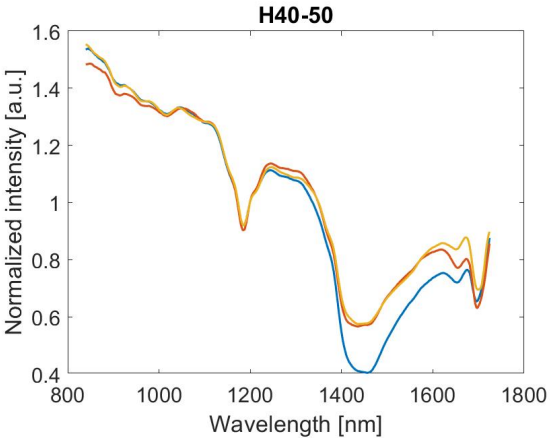

(k)

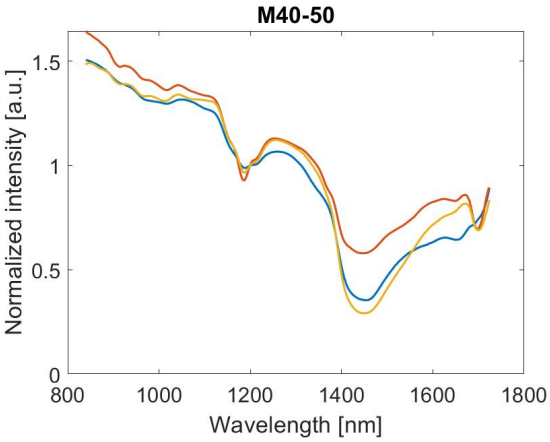

(l)

Figure A.1 continued

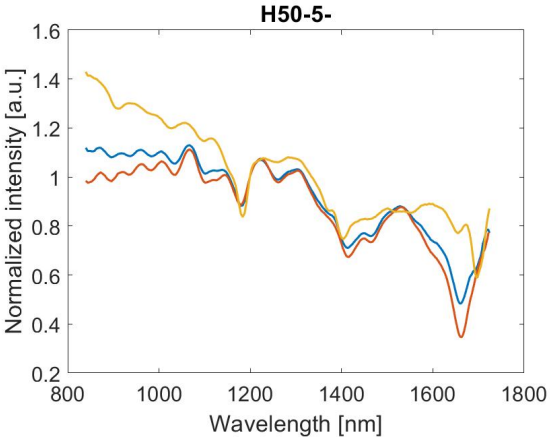

(m)

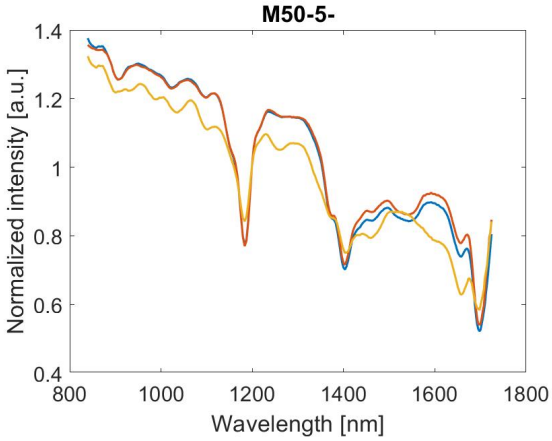

(n)

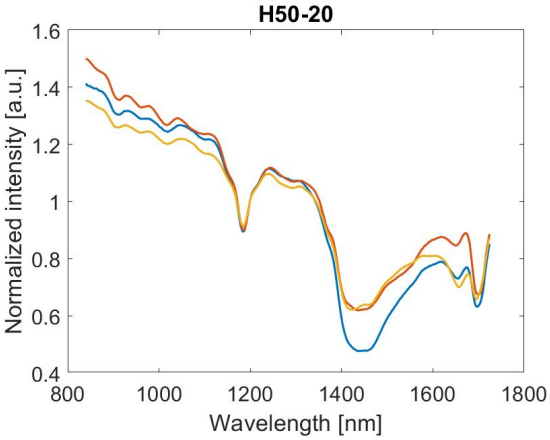

(o)

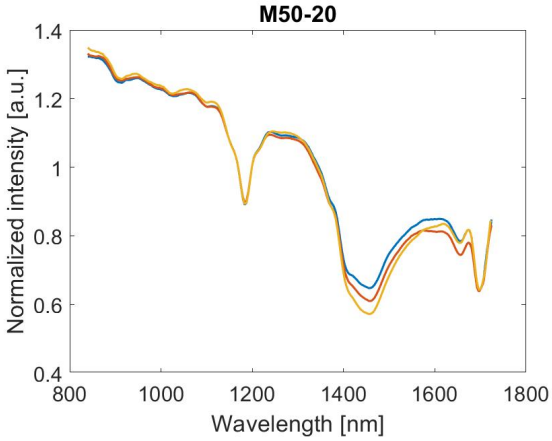

(p)

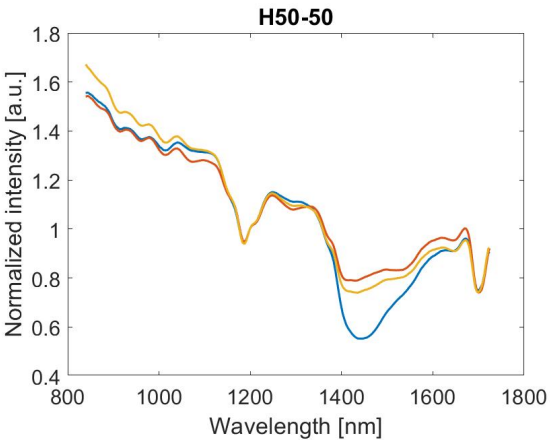

(q)

Figure A.1 continued

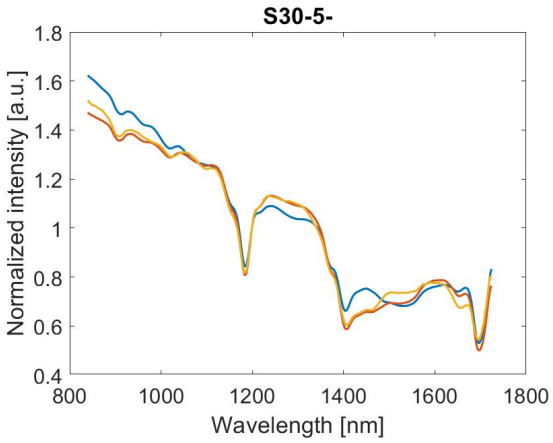

(r)

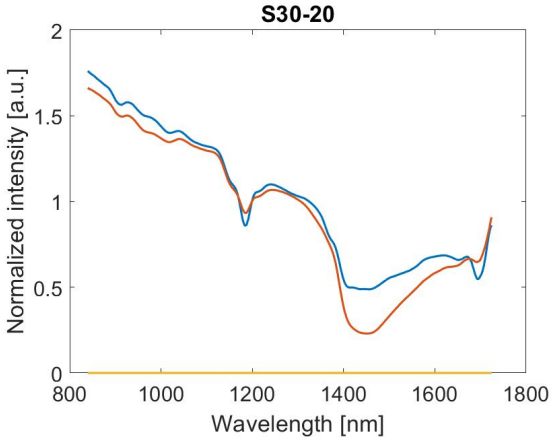

(s)

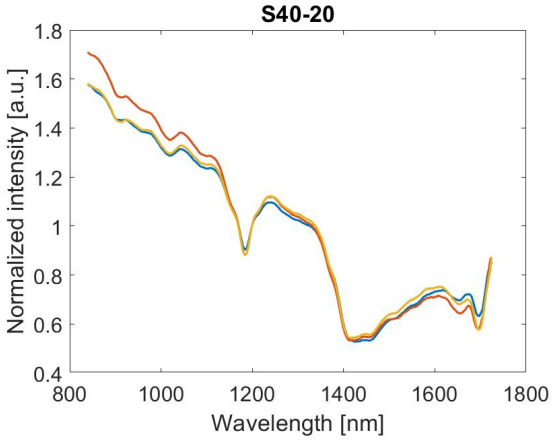

(t)

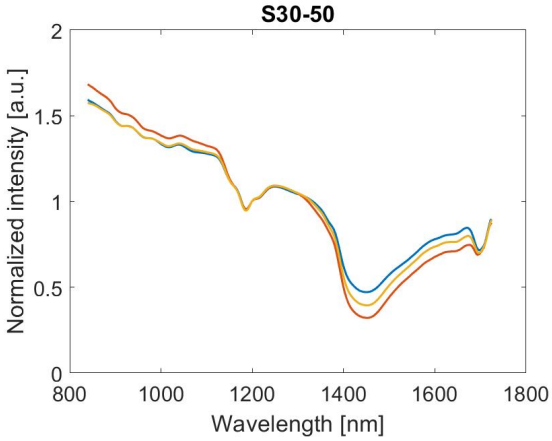

(u)

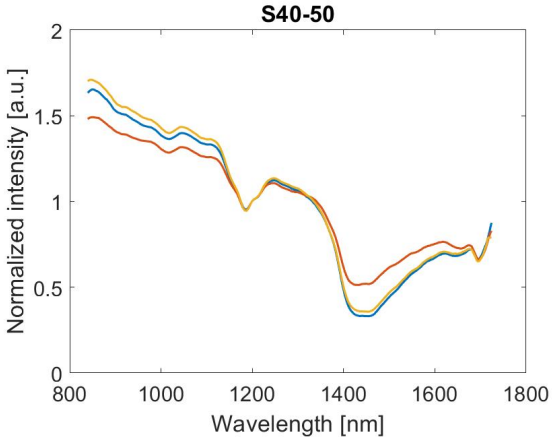

(v)

Figure A.1 continued

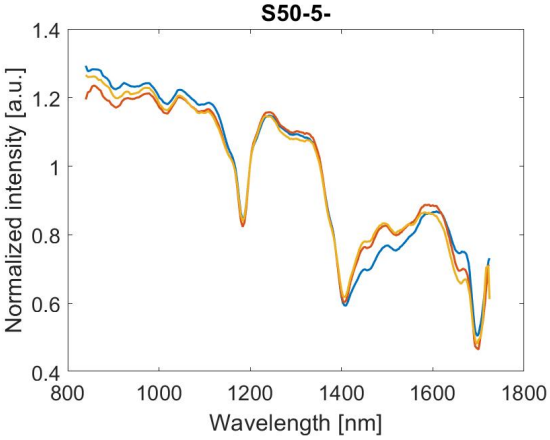

(w)

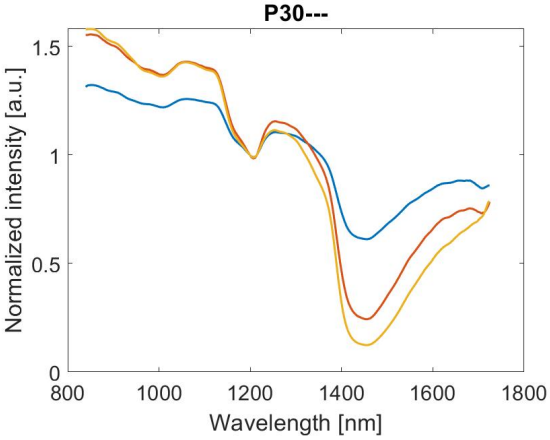

(x)

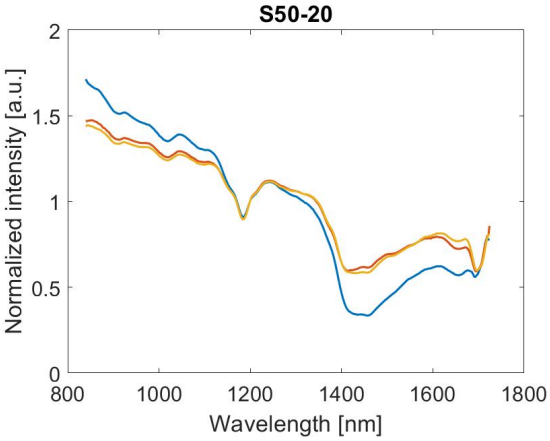

(y)

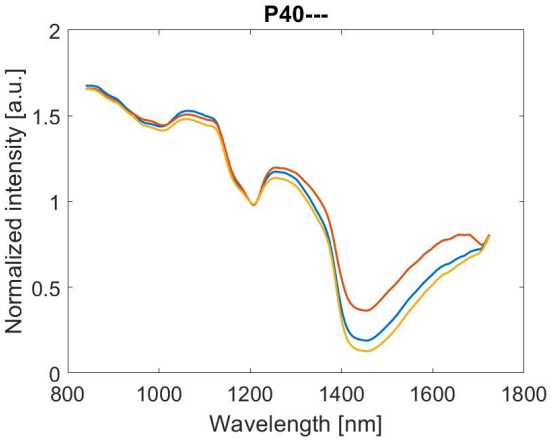

(z)

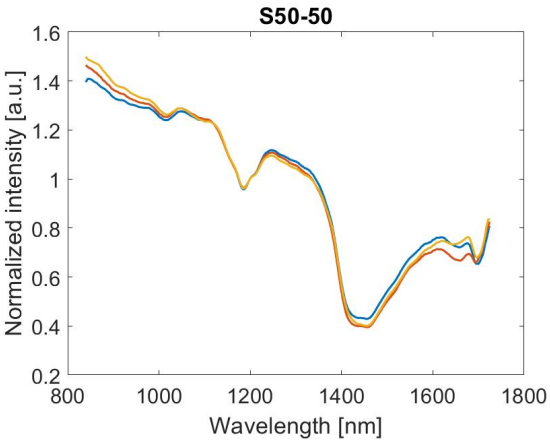

(aa)

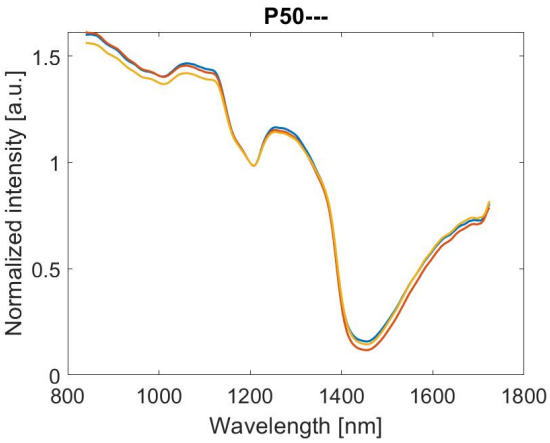

(ab)

Figure A.1 continued

Appendix B

Drill test results

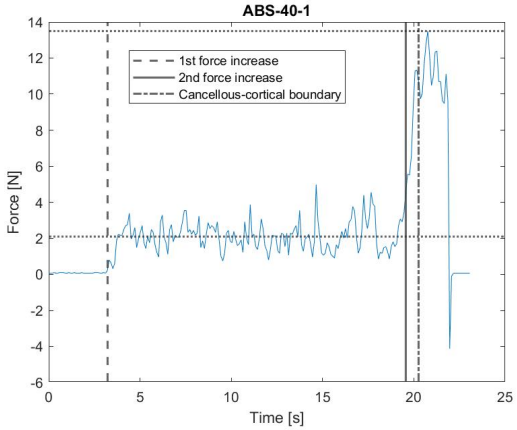

(a) 40% infill density, hole 1

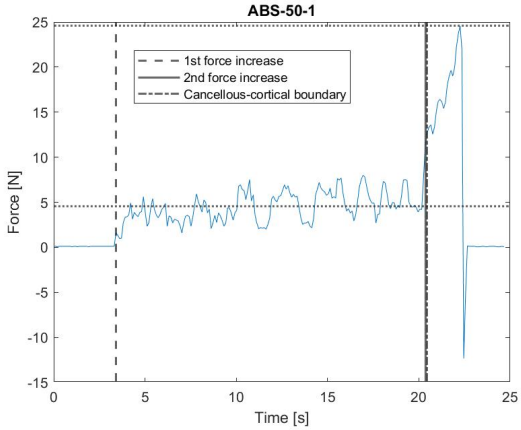

(b) 50% infill density, hole 1

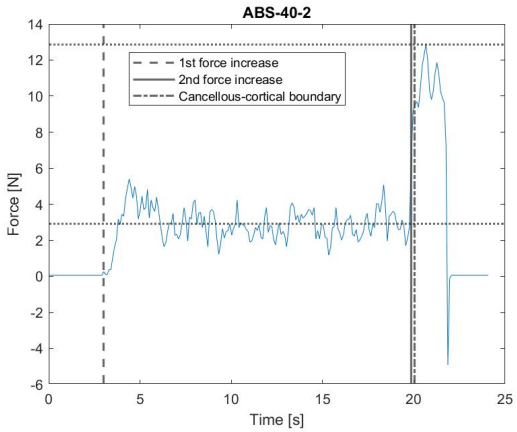

(c) 40% infill density, hole 2

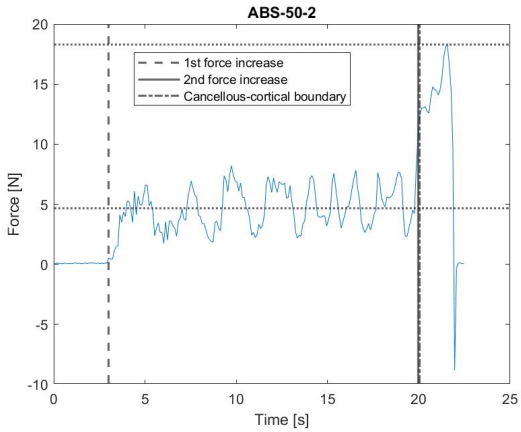

(d) 50% infill density, hole 2

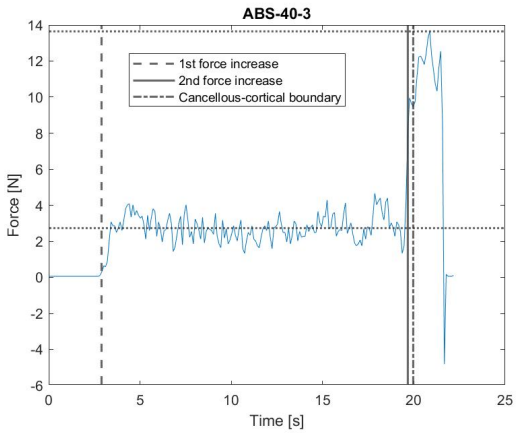

(e) 40% infill density, hole 3

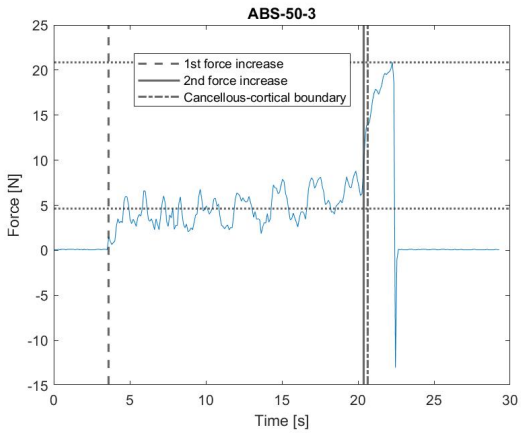

(f) 50% infill density, hole 3

Figure B.1: Axial force on the drill while drilling in ABS samples with various infill densities, without optical filler, as a function of time. In the plots, the mean force in the 50% infill core of the phantom is indicated with a horizontal dotted line, just like the peak force in the cortical part of the phantom. On top of that, vertical dotted lines indicate a step increase in infill density.

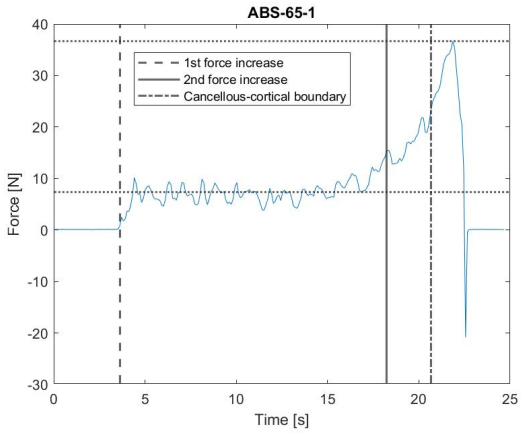

(g) 50% infill density, hole 1

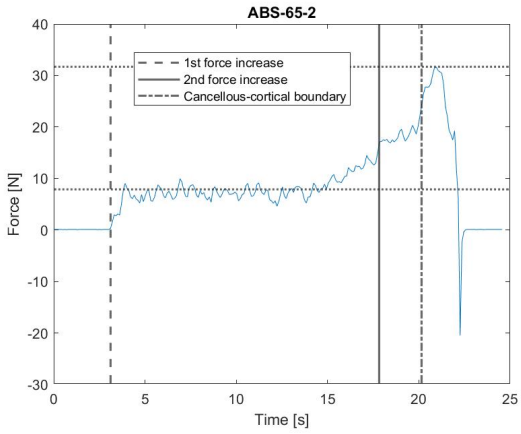

(h) 50% infill density, hole 2

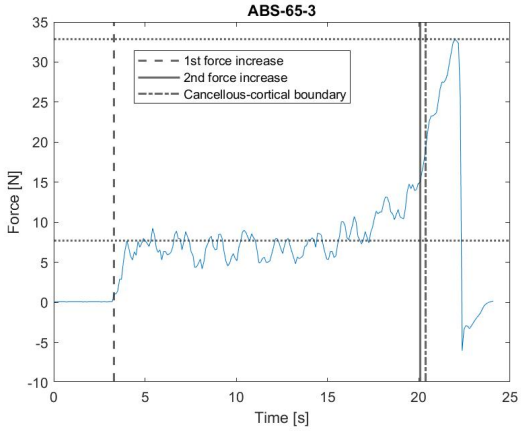

(i) 50% infill density, hole 3

Figure D.1 continued

Appendix C

Compression test results

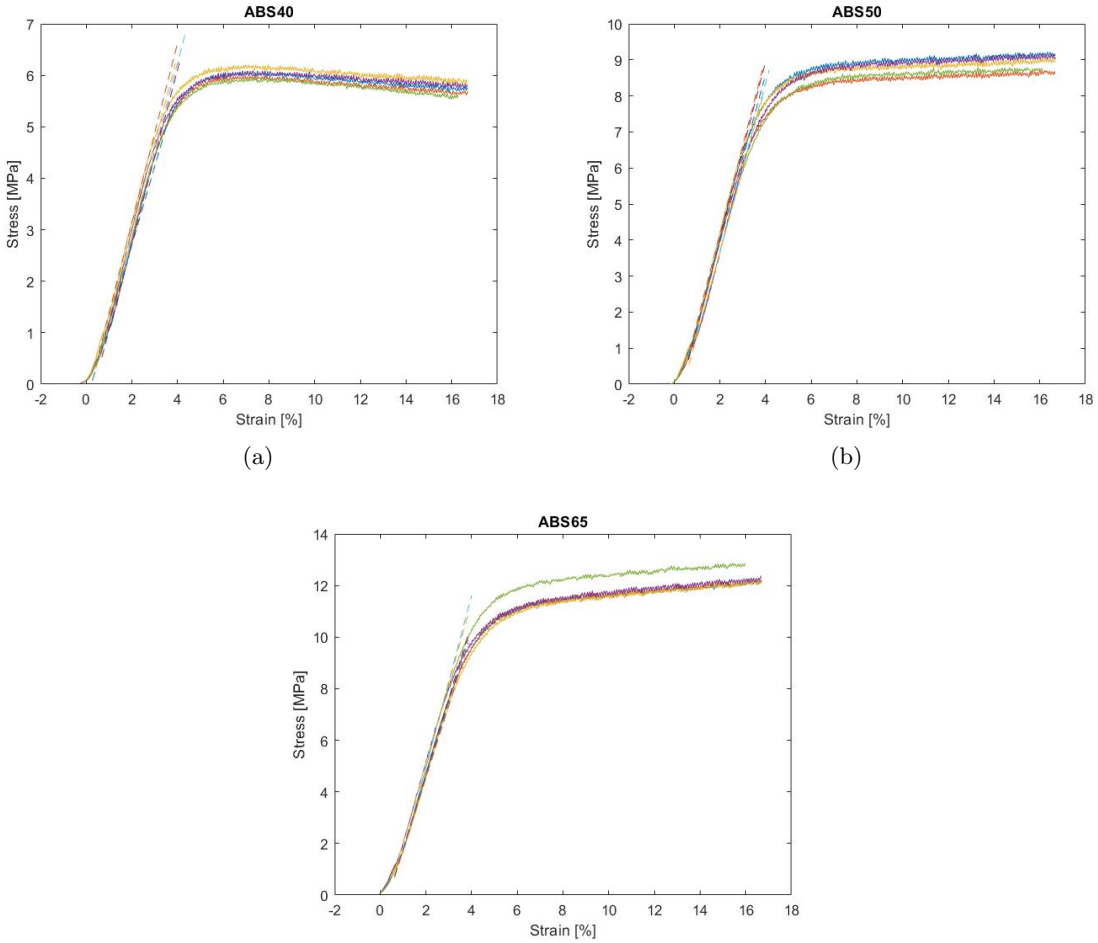

Figure C.1: Stress-strain plots of ABS samples with various infill densities without optical filler. In the plots, a linear fit of the linear-elastic part of the curve is indicated with a dotted line. The slope of this linear fit is an approximation of the E-Modulus of the samples.

Appendix D

Integrated drill test

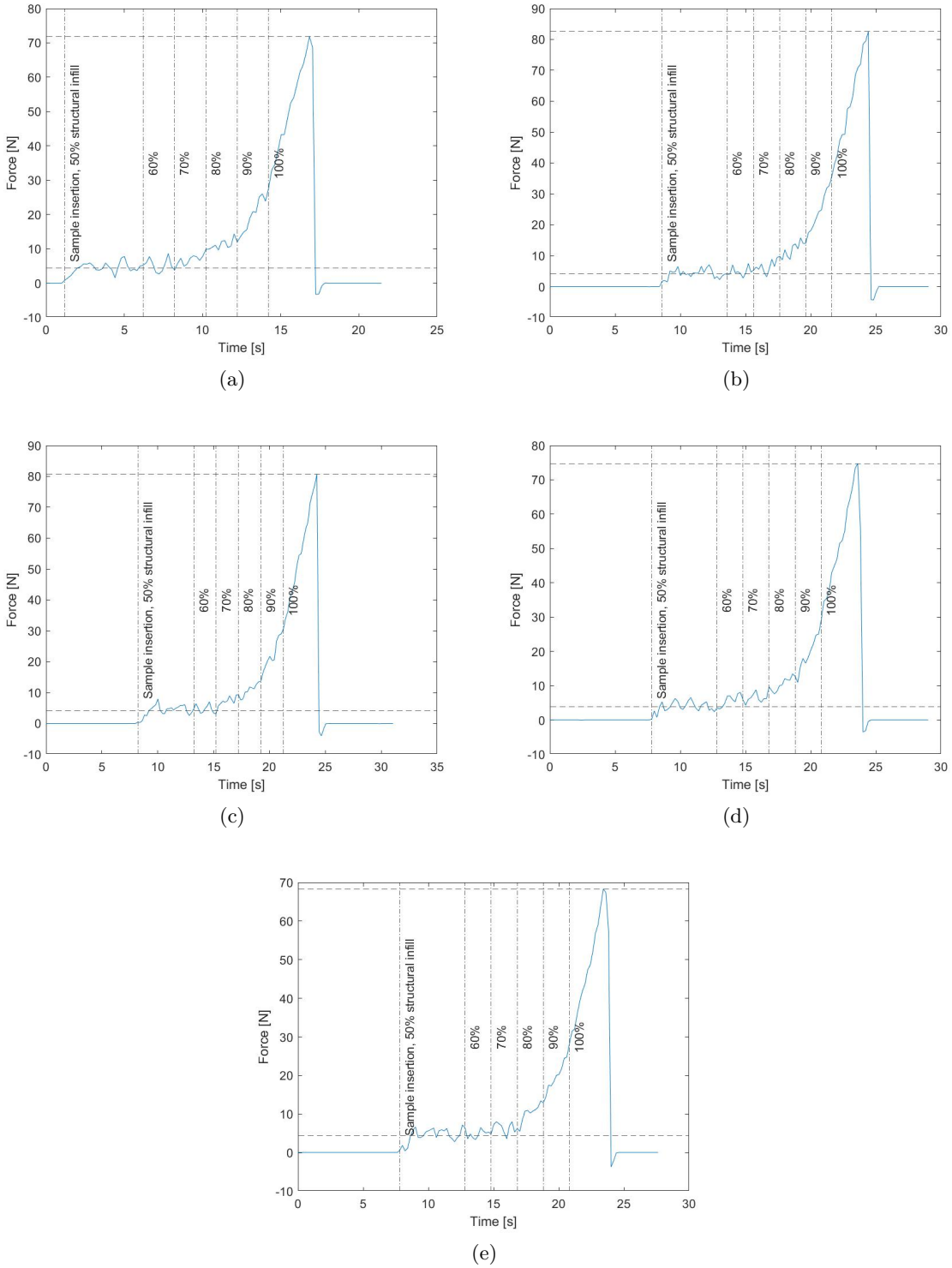

Figure D.1: Axial drill force over time of five drilled holes in samples with ABS 50% gyroid infill density in the core, a structural gradient towards the outside of the phantom, and a hybrid optical filler with 50% water+fat content, a FF of 40%, and 1 wt% Xanthan gum as a natural emulsifier. In the figure, the mean force in the 50% infill core of the phantom is indicated with a horizontal dotted line, just like the peak force in the cortical part of the phantom. On top of that, vertical dotted lines indicate a step increase in infill density.